Light as a Probe: Harnessing Optical Resonances for Sensing Chemical Diffusion and Mechanical Strain

by

Swapnil Daxini
B.Sc., University of Victoria, 2020

A Dissertation Submitted in Partial Fulfillment of the
Requirements for the Degree of

DOCTOR OF PHILOSOPHY

in the Department of Physics and Astronomy

We acknowledge and respect the Lək̓ʷəŋən (Songhees and Esquimalt) Peoples on whose territory the university stands, and the Lək̓ʷəŋən and W̱SÁNEĆ Peoples whose historical relationships with the land continue to this day.

Light as a Probe: Harnessing Optical Resonances for Sensing Chemical Diffusion and Mechanical Strain

by

Swapnil Daxini
B.Sc., University of Victoria, 2020

Supervisory Committee

Dr. Hans-Peter Loock, Supervisor
(Department of Chemistry)

Dr. Andrew MacRae, Departmental Member
(Department of Physics)

Dr. Geoffrey Steeves, Departmental Member
(Department of Physics)

Dr. Peter Wild, Outside Member
(Department of Mechanical Engineering)

Abstract

Sensors are fundamental to modern technology, supporting applications from environmental monitoring and industrial safety to structural health assessment and healthcare. However, conventional electrical and mechanical sensors often face limitations in sensitivity, robustness, and scalability. Rapid advances in optics and photonics are overcoming these challenges by harnessing light-matter interactions to detect physical, chemical, and mechanical changes with exceptional precision. These optical approaches enable remote, real-time, and multiplexed measurements while offering enhanced sensitivity and immunity to electromagnetic interference. This thesis uses optical resonance-based sensors to study VOC diffusion in polymers and to perform long-range strain sensing.

In the first part of this work, extraordinary optical transmission (EOT) through metallic nanohole arrays (NHAs) is employed as a refractive index sensing platform to study the diffusion kinetics of volatile organic compounds (VOCs), specifically o-xylene, into thin polydimethylsiloxane (PDMS) films. Rigorous analytical models based on integrated solutions to Fick's laws of diffusion are derived for both permeable and impermeable polymer films, extending classical approaches and enabling more accurate extraction of diffusion coefficients from experimental data. The resulting NHA-based sensor platform is simple to fabricate, operates in real time, and enables continuous, cost-effective monitoring of VOC sorption and desorption, providing new insights into diffusion dynamics in polymer analyte systems.

The second part of the thesis presents a long-range, high-resolution fiber-optic strain sensor based on a π-shifted fiber Bragg grating (π-shifted FBG) interrogated using the Pound-Drever-Hall (PDH) frequency locking technique. Enhanced field localization in the π-shifted FBG cavity, combined with sub-picometer wavelength resolution afforded by PDH interrogation, enables nanostrain-level response over fiber tethers up to 75 km, eliminating the need for in-line amplification. A coherent PDH scheme further improves the signal-to-noise ratio, extending the theoretical sensing range beyond 150 km.

Together, these studies demonstrate how optical resonance phenomena - from plasmonic nanostructures to resonant fiber gratings - can be harnessed to probe chemical and mechanical processes with high sensitivity and range, paving the way for advanced sensing platforms in environmental and structural applications.

Table of Contents

List of Tables

List of Figures

Co-Authorship

Unless explicitly stated, all work presented in this thesis was performed by the author under the supervision of Dr. Hans-Peter Loock. The author made the main contribution of all of the work detailed in this thesis, including instrument design and development, programming, data analysis and manuscript preparation.

The derived diffusion equations in Chapter 2 were derived with the help of Dr. Jack Barnes and Dr. Hans-Peter Loock, and built upon the work by Dr. John Saunders. This chapter is currently under review for publication in *Soft Matter*.

The nanohole array gas sensing setup described in Chapter 3 was work with Dr. Chris Prüfert, Mr. Paul Reid, Mr. Pedro Barros, Dr. Juan Gomez-Cruz, Dr. Carlos Escobedo, Dr. Jack Barnes, and Dr. Hans-Peter Loock and is currently under review for publication in *Analyst*. The inital setup at Queen's University was designed and developed with Dr. Juan Gomez-Cruz. The nebulizer gas flow system was designed and constructed with Dr. Chris Prüfert. The FDTD modeling was performed with the help of Mr. Paul Reid. All the programming, data collection, and data analysis were performed by myself.

The long-range strain sensing described in Chapter 4 was work with Mr. Arthur Giron Santos, Dr. Jack Barnes, Dr. Xijia Gu, and Dr. Hans-Peter Loock and has previsouly been published [1]. This work built upon initial work done by Dr. Deniz Aydin. Dr. Xijia Gu provided the grating used for the setup. The construction of the setup described in this chapter was done by myself and Dr. Deniz Aydin. All programming, data collection and data analysis was done by myself.

The coherent Pound-Drever-Hall system described in Section 4.4 is currently under review for publication with Dr. Arthur Giron Santos, Dr. Jack Barnes, Dr. Xijia Gu and Dr. Hans-Peter Loock. I am the second author. The setup described here was designed and constructed between myself and Arthur Giron Santos. The data presented in this section was collected by Arthur Giron Santos. I had designed and constructed the circuitry for the setup.

Acknowledgements

First and foremost, I would like to thank my supervisor, Dr. Hans-Peter Loock, for your support, patience and guidance throughout my PhD journey. You have made the PhD an enjoyable journey despite all of its challenges. Your patience and encouragement carried me through moments of doubt, and you believed in me even when I struggled to believe in myself. It has been a privilege to learn from you, and I will carry the lessons from your mentorship far beyond this thesis.

Secondly, I would like to thank all the members of our research group, who have truly made the lab not only a wonderful place to learn but also an enjoyable place to spend so much of my time. I would like to thank Dr. Jack Barnes for his constant support and willingness to help with any question I had throughout my research. I also want to thank Monique, Arthur, Paul, and Pedro - it has been a pleasure to see you grow as researchers and bring such enthusiasm to the lab. A special thank you goes to Emma and Oren, who have been there from the very beginning. It's been such a pleasure to grow alongside you - from figuring out how to set up the new lab to countless conversations that helped me think through my research. I am also grateful to Chris, whose mentorship taught me many of the valuable skills and work habits that have carried me through this degree.

I would like to thank Dr. Carlos Escobedo, Juan, and all the members at Queen's University for their warm hospitality and invaluable help during my time conducting research there. I am also deeply grateful to Dr. Andrew MacRae, whose curiosity has always inspired me and who helped instill that same spirit in me from my second year of undergrad, continuing to offer support throughout my journey. I also appreciate the help of Nick Braam, who taught me everything I know about building circuits and whose guidance was invaluable throughout my work. I would like to thank the Wuitchik Family and Dr. Arne H. Lane for their generous support through fellowships, which enabled me to pursue and complete this research.

I would also like to thank all my friends who made this journey so much more bearable - and far more enjoyable. Your support and laughter, provided the balance I needed outside of research, and I'm deeply grateful for the many memories we've shared along the way.

I would like to thank my parents, Naresh and Reema Daxini and my brother, Jay Daxini, for always believing in me and supporting me throughout my entire academic journey.

Special thanks to my cats, Shadow and Hazel, whose constant purring and need for attention kept me sane through writing process.

Finally, I would like to thank my partner, Hannah, who has always believed in me and

stood by my side through the roughest times and countless breakdowns. Your unwavering support, patience, and love kept me going when things felt overwhelming, and you were always my biggest cheerleader, celebrating every small victory along the way. I am forever grateful to have you in my life.

Dedication

To my parents, whose sacrifices and love made this journey possible.

Chapter 1

Introduction

In an increasingly interconnected and technologically advanced world, the demand for reliable, accurate, and sensitive sensors is greater than ever. Sensors are used in range of applications, from ensuring the structural integrity of critical infrastructure such as bridges, aircraft, and pipelines, to enabling real-time monitoring of environmental conditions, industrial processes, and human health.

The rapid progress in optical science and photonic engineering over the past few decades has opened new avenues for sensor development, offering pathways to improve sensitivity, selectivity, and robustness beyond what is achievable with conventional electrical or mechanical sensing approaches. Optical sensors leverage the interaction of light with matter to detect physical, chemical, or biological changes with high precision. Their immunity to electromagnetic interference, potential for remote sensing, and compatibility with miniaturized and multiplexed platforms make them attractive for next-generation sensing applications [2]. Examples of such sensors include optical fiber sensors for strain and temperature measurements, interferometric biosensors, and plasmonic sensors for detecting changes in refractive index or molecular binding events.

The sensitivity of optical sensors is ultimately determined by how changes in the environment are transduced into measurable changes of the light field. A wide range of optical parameters can serve as these sensing observables, including phase, intensity, wavelength, polarization, and spectral line shape. Environmental perturbations - such as changes in refractive index, strain, temperature, or pressure - can induce changes in one or more of these properties, which are then monitored to quantify the underlying physical or chemical change. The design of optical sensors often focuses on maximizing the device's sensitivity to these changes. This is typically achieved by enhancing the light–matter interaction through strategies such as increasing the effective interaction time or distance between light and the medium, or by amplifying the local electromagnetic field strength in the sensing region.

Interferometric sensors such as Mach–Zehnder and Michelson interferometers achieve enhanced sensitivity by splitting and recombining light beams with different optical paths. Small changes in optical path length due to external environmental parameters along one arm lead to detectable phase shifts, enabling precise detection of environmental changes [3, 4]. Similarly, ring resonators and whispering-gallery mode (WGM) cavities further extend this principle by circulating light many times around a closed-loop path, amplifying the effective interaction length within a compact footprint [5].

Optical cavities (or resonators) confine light between highly reflective mirrors, causing it to undergo multiple passes through the sensing region, thereby storing the light at high powers for long times over which it interacts with the analyte. These cavities can be used for gas detection and spectroscopy through time domain measurements such as the ring-down time [6], but also serve as narrow band-pass filters for certain resonant wavelengths of light due to constructive interference in the cavity. These resonances can be used for strain, temperature and refractive index measurements [7].

Sensors can also contain photonic structures that increase the local electromagnetic field intensity to strengthen the light–matter interaction at the sensing interface. Plasmonic nanostructures, such as nanohole arrays, gratings, or nanoparticle assemblies, support collective electron oscillations known as surface plasmon polaritons (SPPs) at metal–dielectric interfaces [8]. These resonances enhance the local electromagnetic field, making them extremely sensitive to refractive index changes near the surface [9, 10].

Building on these fundamental strategies, this thesis explores two resonance-based optical sensing platforms. Plasmonic nanohole arrays are employed as refractive index sensors to monitor the diffusion kinetics of volatile organic compounds into a polymer, leveraging strong near-field enhancement at the metal-dielectric interface to detect refractive index changes. In parallel, π-shifted fiber Bragg gratings are developed as point-based optical strain sensors capable of remote interrogation over tens of kilometers, where resonant field buildup within a Fabry-Perot-like cavity enhances the detection of small mechanical perturbations through precise tracking of wavelength shifts of the cavity resonance.

In the following sections, I briefly introduce the two main topics of this thesis - monitoring the diffusion kinetics of volatile organic compounds through the surface plasmon enhancement of an optical resonance, and monitoring strain and sound through locking a laser wavelength to an optical resonance of a fiber grating. Both techniques take advantage of optical resonance enhancement and derive the desired signal from a wavelength shift of this resonance. Arguably wavelength shifts are a superior measurand compared to light intensity measurements, since the latter is easily distorted by transmission losses, detection

responses and other processes that are difficult to quantify.

1.1 Extraordinary optical transmission-based sensors

This thesis presents a real-time, continuous, and cost-effective VOC sensing platform based on extraordinary optical transmission (EOT) through metallic nanohole arrays. By tracking resonance shifts induced by refractive index changes, the platform enables direct measurement of the diffusion kinetics of volatile organic compounds (VOCs), such as o-xylene, into polydimethylsiloxane (PDMS).

The phenomenon of extraordinary optical transmission (EOT) refers to the anomalously high transmission of light through periodic arrays of sub-wavelength holes in metallic films. Classical aperture theory, developed by Bethe in 1944, predicts that transmission through a single hole smaller than the wavelength should be extremely weak, scaling as $(d/\lambda)^4$, where d is the hole diameter and λ is the wavelength of normally incident light [11]. However, Ebbesen *et al.* [9] demonstrated in 1998 that periodic nanohole arrays in noble metal films can transmit orders of magnitude more light than predicted (Fig. 1.1a). This unexpected effect was largely attributed to the resonant excitation of surface plasmon polaritons (SPPs) [12], making EOT a central topic in modern plasmonics and an enabling mechanism for optical sensing applications.

The resonance condition depends on the local refractive index near the interface, and as a result, any change in the surrounding medium alters the plasmonic resonance and the transmission spectrum. Fig 1.1b shows typical EOT transmission spectra for different refractive indices near the metal-dielectric surface.

Monitoring the resonance wavelength shift, rather than the absolute transmitted intensity, offers a significant advantage for chemical sensing. Because the resonance condition depends on the optical phase matching at the metal–dielectric interface, the spectral position of the EOT peak remains largely insensitive to fluctuations in the intensity. As a result, resonance shift measurements enable more robust, quantitative determination of refractive index changes, and thus VOC concentration. This principle has been used to measure the refractive index of liquids [13] and polymers [14] with high precision. Contrary to other optical techniques that are used for VOC detection, the nanohole array-based is operated in transmission mode, allowing for easier alignment, miniaturization and multiplexing [15, 16]. A conventional absorption spectrometer suffices for the measurement of the EOT signal. The fabrication of the device that we developed below is facile, rapid, and does not require a cleanroom.

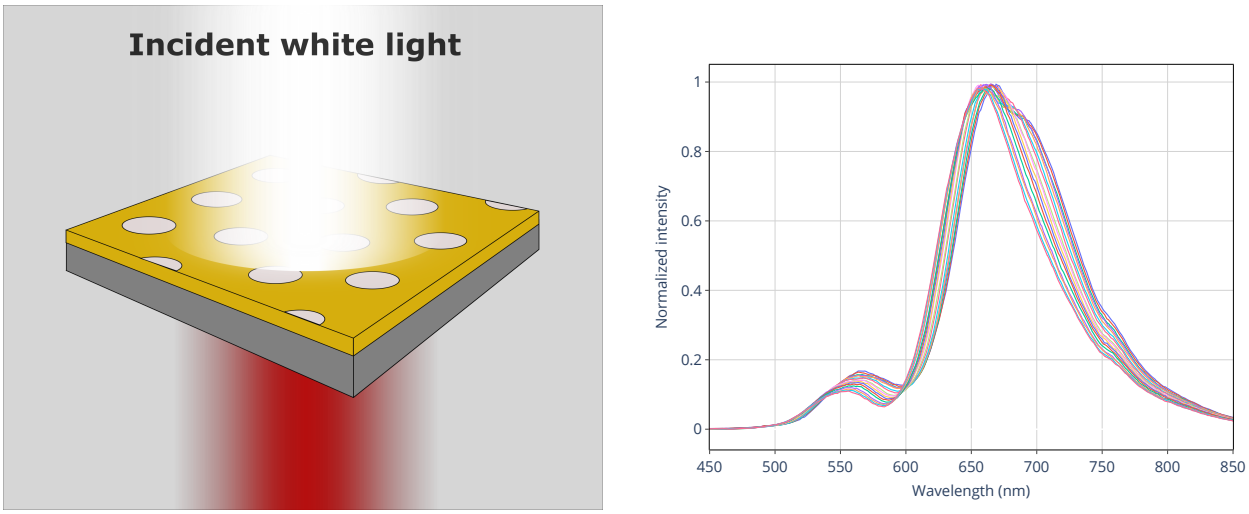

(a) Example of EOT transmission

(b) EOT resonance spectra

Figure 1.1: EOT transmission through nanohole arrays

Following the publication of the seminal work on EOT by Ebbesen et al. in 1998, there have been numerous sensing systems based on nanohole arrays for refractometry [17, 13], biosensing [12, 18, 19], as well as in multiplexed systems [20, 18]. Recent work has demonstrated the use of nanohole arrays for gas detection [21, 22], though the systems were based on monitoring intensity changes, rather than the plasmonic shift induced by refractive index changes, and may therefore be more prone to noise from the light source and detector.

Polydimethylsiloxane (PDMS) is widely used in chemical sensing because of its high permeability to volatile organic compounds (VOCs), chemical stability, optical transparency, and ease of fabrication. Its hydrophobic nature and affinity for non-polar molecules make it particularly suitable for detecting hazardous VOCs such as benzene, toluene, ethylbenzene, and xylenes (BTEX). As VOCs diffuse into PDMS, they alter its local refractive index and cause swelling of the polymer matrix, effects that can be transduced into optical signals.

In this thesis, we leverage these properties to develop a real-time, on-line VOC sensing platform based on extraordinary optical transmission (EOT) through metallic nanohole arrays. By coating the arrays with a thin PDMS layer, we demonstrate that tracking shifts in the plasmonic resonance provides a powerful and intensity-independent method to monitor VOC uptake and release dynamics and to directly extract diffusion kinetics from optical measurements. This approach enables detailed characterization of VOC–polymer interactions and establishes a versatile platform for chemical sensing.

1.2 Fiber-optic strain sensing

Fiber Bragg gratings are the most common optical sensor heads for localized strain sensing as they provide all advantages of fiber optic sensors, while being relatively simple to fabricate and interrogate. A fiber grating consists of a periodic variation of the refractive index within the core of an optical fiber (Fig. 1.2a). They are commonly fabricated through means of photo-inscription where high-intensity UV light with an interference pattern is incident on the fiber core, which may be chemically sensitized. Upon absorption of the light, there is change in the germanium-silicon dioxide bond, resulting in an increase in the refractive index [2].

When the pitch of the grating, Λ, is less than 1 μm, the resulting structure is referred to as a Fiber Bragg Grating (FBG). Longer periods produce so-called Long Period Gratings (LPGs) which have found many applications in refractive index sensing [23].

In case of an FBG, the fundamental modes in the forward and backward propagating directions couple to each other, resulting in a narrowband reflection at the Bragg wavelength:

$$\lambda_B = 2n_{\text{eff}}\Lambda \tag{1.1}$$

where n_{eff} is the effective refractive index of the core [24]. The characteristics of the reflection envelope are dependent on the grating parameters such as the period, difference in refractive index and the length of the grating [2]. Fiber Bragg gratings are particularly useful for sensing applications as both the pitch and refractive index change due to environmental factors such as strain and temperature.

FBGs are particularly attractive for strain sensing because many physical phenomena - including pressure, displacement, vibration, and acoustic fields - manifest as mechanical deformation in a material. Structural deflection produces surface strain that can be used to infer displacement or load distribution [25], while vibrations and acoustic waves induce periodic strain fluctuations that can be monitored with high sensitivity. In geophysical and civil applications, strain measurements reveal pressure changes, seismic events, or ground motion [2], and in biomedical contexts they are used to track heartbeat, respiration, and muscle activity [26].

Specialized FBG structures can be created that exhibit unique spectral properties. A Fabry-Perot cavity can be formed with two identical matched FBGs separated by a few millimeters. Similarly as in free space, the cavity will allow for high transmittance for certain resonant frequencies, uniformly spaced apart, with a spectral width much smaller than that of the envelope [28]. Among the various FBG configurations, the π-shifted fiber Bragg grating

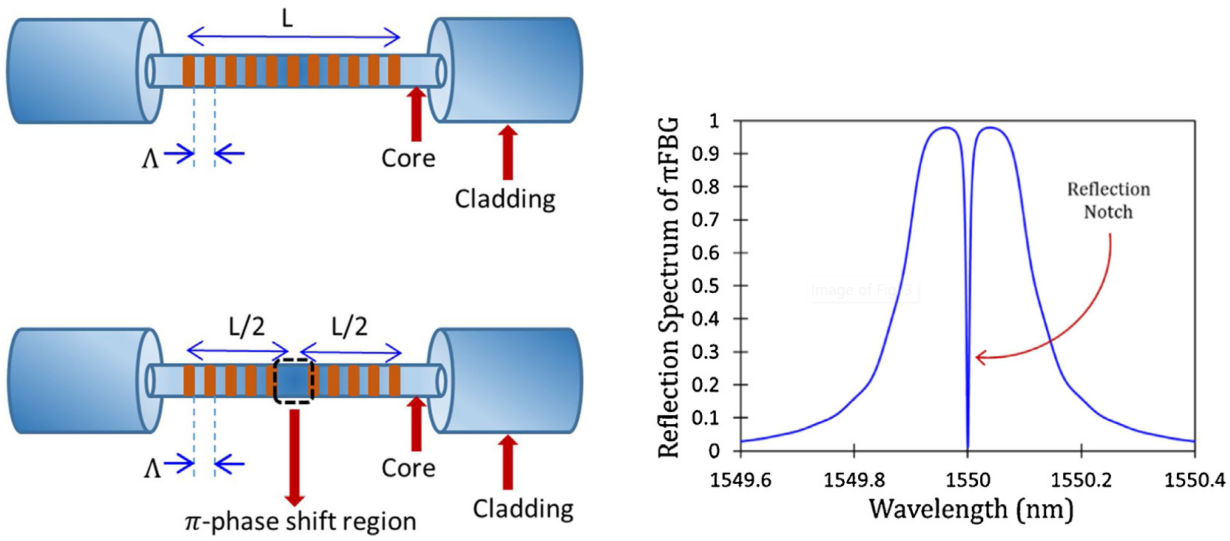

(a) FBG and π-FBG

(b) π-FBG reflection spectrum

Figure 1.2: Schematic of a conventional FBG and a π-phase shifted FBG, and the reflection spectrum for π-FBG gratings. This figure was taken from Reference [27]

(π-FBG) is particularly well suited for precision strain sensing. By introducing a π-phase discontinuity within the grating (Fig. 1.2a), a Fabry–Perot-like resonant cavity is formed at the Bragg wavelength, which leads to strong localization of the optical field within the grating [29, 30]. This field localization creates a sharp transmission resonance within the reflection envelope of FBG (Fig. 1.2b). The enhanced field–matter interaction within the π-shifted cavity allows for the detection of picostrain-level changes in the fiber [31]. Furthermore, π-FBG sensors retain the advantages of standard FBGs - such as compactness, passive operation, and multiplexing capability - while offering superior sensitivity, making them particularly attractive for long-distance remote sensing in environments where maintenance-free operation is essential.

In this work, we focus on tracking the resonance wavelength of a π-FBG, a narrow spectral feature that shifts in response to strain-induced changes. Because the resonance arises from optical phase-matching within the grating, its position shifts predictably with strain and can be monitored with high precision, independent of broadband intensity variations. Building on this principle, we developed a long-range, passive, all-fiber strain sensing system that interrogates the π-FBG using the Pound–Drever–Hall (PDH) technique. PDH interrogation is particularly well suited for this approach, as it converts minute resonance shifts into high signal-to-noise error signals that remain detectable even at very low return powers. By locking a diode laser to the π-FBG resonance, the system achieves nanostrain-level sensitivity

over fiber tethers up to 75 km without requiring in-line amplification, demonstrating the feasibility of long-range strain sensing in harsh or inaccessible environments.

1.3 Thesis outline

This thesis investigates how optical resonances - both plasmonic and grating-based - can be used to enhance light–matter interaction and enable high-sensitivity sensing of chemical and mechanical phenomena. The thesis is structured as follows:

Chapter 2 develops the theoretical foundation for describing diffusion kinetics in thin polymer films. By revisiting and extending Crank's classical solutions to Fick's laws of diffusion, exact integrated equations are derived for both impermeable and permeable boundary conditions. These models form the mathematical basis for interpreting experimental data in Chapter 3.

Chapter 3 applies these diffusion models to the detection of volatile organic compounds (VOCs) using metallic flow-through nanohole arrays (NHAs). The chapter details the design, fabrication, and optical characterization of the plasmonic sensor platform, and demonstrates its ability to monitor VOC sorption and desorption in real time. The extracted diffusion coefficients are compared with literature values, and the influence of surface functionalization, film thickness, and delivery methods on sensing performance is analyzed.

Chapter 4 explores a long-range fiber-optic strain sensor based on a π-shifted fiber Bragg grating (π-FBG) interrogated using the Pound-Drever-Hall (PDH) locking technique. The chapter presents the experimental setup, noise analysis, and sensor characterization, demonstrating nanostrain-level sensitivity over fiber tethers up to 75 km. Furthermore, we demonstrate a coherent PDH scheme that enhances the error signal's signal-to-noise ratio, enabling laser locking with return powers as low as -58 dBm (< 2 nW). This removes the need for optical amplification and theoretically extends the sensing range to 155 km.

Chapter 5 summarizes the key findings of the thesis, highlights their broader implications for optical sensing technologies, and outlines directions for future research, including potential improvements to the VOC detection platform and the application of the long-range strain sensing setup for a fiber optic hydrophone and free-space configurations.

Chapter 2

Exact integrated equations to describe diffusion kinetics

This chapter first derives and introduces the modelling of diffusion constants through permeable membranes by revisiting Crank's solution to Fick's diffusion from 1950. This part of the chapter is from a submitted publication that builds upon work done by Dr. John Saunders and Dr. Jack Barnes, a previous PhD student and Senior Research Associate in the Loock group. The diffusion equations were derived to develop a model that would allow us to fit to the experimental data described in the following chapter (Chapter 3).

2.1 Introduction

In his seminal 1956 book "The Mathematics of Diffusion", John Crank derived the differential equations describing Fick's Law of Diffusion for two limiting but common cases: (1) the diffusion of an analyte into a film that is supported by an impermeable substrate, and (2) the diffusion of an analyte into a free-standing film that has no analyte entering from the opposing side [32] (Fig. 2.1).

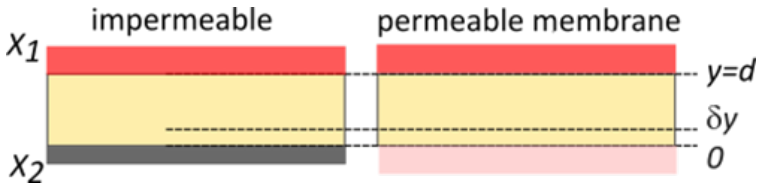

Figure 2.1: Boundary conditions and integration bounds for a film (yellow) on an impermeable (left, grey) and permeable substrate (right) as described in the text. The concentration above the polymer film (red) is held at a constant concentration of X_1 for both cases. For the impermeable substrate, the concentration below the polymer is always 0 (grey region), while the concentration below the permeable membrane (pink) is given by X_2.

Both are one-dimensional diffusion problems, and a straightforward and exact analytical solution can be obtained by integration that describes the kinetics of diffusion. Indeed, the measurement of the relative analyte concentrations in a film as a function of time is one of the most common methods to determine the diffusion rate.

Experimental concentration measurements, obtained either as an average of the concentration of the analyte in the entire film or taken at a particular distance from its surface, can be used to obtain the diffusion constant for the particular film:analyte system by fitting to the equations describing the diffusion kinetics. The concentration is obtained from some measured property, $X(y,t)$, that has to scale linearly with the concentration of the analyte and could be the mass of the film [33], or its polarizability volume [34, 35], its fluorescence intensity [36], or its absorbance [37], among others. Since the measurement site and the film thickness, d, are usually known, these fits only require two variables, i.e. the diffusion constant, D, and a property that describes the equilibrium concentration of the analyte in the film, X_∞. These properties can be determined from primary measurements such as optical transmission [37], refractive index measurements [35], optical [38] or mechanical [39] resonance frequency shifts, etc.

While the exact diffusion equations are readily derived, most chemists use much simpler equations to fit the diffusion kinetics, and to obtain the diffusion constants. These are based on the exponential asymptotic growth function for analyte entering the film and on the exponential decay function for analyte diffusing out of a film

$$\begin{aligned} \overline{X}(t) &= X_\infty \left[1 - \exp\left(-D\frac{\pi^2 t}{4d^2}\right)\right] \\ \overline{X}(t) &= X_\infty \exp\left(-D\frac{\pi^2 t}{4d^2}\right) \end{aligned} \tag{2.1}$$

With these equations one can obtain an expression for the diffusion constants based on the saturated concentration by observing the half-concentration, the initial or the limiting slope [33, 40]. As was mentioned previously, these functions are first-order approximations to the exact analytical functions [34, 41], and provide a comparably poor fit in some cases, particularly when there is uncertainty in the value of the saturated concentration. A 10% deviation in the saturated concentration can lead to an error of up to 50% in the estimation of the diffusion constant [42].

In this chapter, we derive "ready-to-use" integrated equations that allow a practitioner to obtain accurate diffusion constants by fitting. Despite their slightly more complex form they are readily incorporated into any fitting algorithm and use the same number of parameters as their first-order approximations.

2.2 Theoretical Model

In his book "The Mathematics of diffusion" in 1956 [32] John Crank derived equations to describe the diffusion kinetics of analytes into a free-standing membrane and into a film supported by an impermeable substrate. He solved Fick's second law of diffusion

$$\frac{\partial X}{\partial t} = D\frac{\partial^2 X}{\partial y^2} \tag{2.2}$$

for several different cases. In the following we assume that the diffusion constant, D, is, in fact, a constant and that the film does not swell or shrink during the diffusion processes.

The Fickian diffusion model is appropriate for polymer networks for tracer diffusion, i.e. when the analyte concentration is very low – an assumption that we consider valid throughout this chapter. Fickian diffusion is also adequate at higher analyte concentrations, when the temperature is well above the glass transition temperature of the film.

Crank solved the partial differential Eq. 2.2 by separation of variables:

$$X(y,t) = C(y)T(t) \tag{2.3}$$

and obtained a general solution of the form:

$$X(y,t) = \sum_{m=1}^{\infty} \left(A_m \sin \lambda_m y + B_m \cos \lambda_m y\right) \exp\left(-\lambda_m^2 Dt\right) \tag{2.4}$$

The constants A_m, B_m, and λ_m, are determined using the respective boundary and initial conditions of the problem. In the present cases we determine the boundary conditions to represent a permeable membrane and an impermeable membrane, with the analyte concentration being represented by the experimental observable, X.

2.3 Film on an impermeable substrate

Assume first that the film is accessible to the analyte at one face and impermeable at the opposite face. We can then treat the problem as one-dimensional diffusion through a plane of finite thickness within an infinite reservoir of analyte.

In this case, we assume that the surface of the membrane ($y = d$) is maintained at constant concentration of X_1, and we do not have any diffusion across the substrate support of the membrane ($y = 0$). Thus, the boundary conditions are given by

$$\begin{aligned} X(y,0) &= X_0 \\ X\left(d,t\right) &= X_1 \\ \frac{\partial X\left(0,t\right)}{\partial y} &= 0 \end{aligned} \tag{2.5}$$

With these boundary conditions, Crank analytically solved the problem of diffusion into a film of finite thickness that is mounted on one impermeable wall [32] and obtained an equation containing an infinite sum of exponentials

$$\frac{X(y,t)-X_0}{X_1-X_0} = 1 - \left[\frac{4}{\pi}\sum_{m=0}^{\infty}\frac{(-1)^m}{2m+1}\exp\left(-D(2m+1)^2\frac{\pi^2 t}{4d^2}\right)\cos\left((2m+1)\frac{\pi y}{2d}\right)\right] \tag{2.6}$$

At short times, a large number of terms in the sum are required, and the following approximate solution is more practical.

$$\frac{X(y,t)-X_0}{X_1-X_0} = \sum_{m=0}^{\infty}(-1)^m \operatorname{erfc}\left(\frac{(2m+1)d-y}{2\sqrt{Dt}}\right) + \sum_{m-0}^{\infty}(-1)^m \operatorname{erfc}\left(\frac{(2m+1)d+y}{2\sqrt{Dt}}\right) \tag{2.7}$$

Balik described a blended model that uses one-term approximations of Eq. 2.6 and Eq. 2.7, and a switching function to shift the weight between the two equations as a function of time [33]

$$\frac{X(y,t)-X_0}{X_1-X_0} = \phi\left(t\right)F\left(y,t\right) + \left[1-\phi\left(t\right)\right]G\left(y,t\right) \tag{2.8}$$

where, $F(y,t)$ and $G(y,t)$ are the right-hand-sides of (1.6) and (1.7) truncated to a single term ($m=0$), and $\phi(t)$ is the Fermi function

$$\phi\left(t\right) = \left[1-\exp\left(\frac{t'-a}{b}\right)\right]^{-1} \tag{2.9}$$

that shifts the weight between the two functions with time. The reduced time is $t' = Dt/d^2$, and $a = 0.05326$ and $b = 0.004$ were determined to give an optimal fit.

With today's computing abilities there is no longer a need for these complications and calculating 20-50 terms for very short time scales and at 3-5 terms at longer timescales is readily possible, and probably simpler.

2.3.1 Concentration gradients for the impermeable substrate

In Eq. 2.6 and Eq. 2.7, X_0 is the initial concentration in the film and X_1 is the equilibrium concentration of the analyte in the film. If the film is initially free of analyte, $X_0 = 0$, as is the case for many absorption experiments, we can write Eq. 2.6 as:

$$X(y,t) = X_1 \left[1 - \frac{4}{\pi} \sum_{m=0}^{\infty} \frac{(-1)^m}{2m+1} \exp\left(-D(2m+1)^2 \frac{\pi^2 t}{4d^2} \right) \cos\left((2m+1) \frac{\pi y}{2d} \right) \right] \tag{2.10}$$

The limiting case at $t \to \infty$ gives the uniform equilibrium concentration $X_\infty = X_1$. The other limiting case at $t = 0$ reduces Eq. 2.10 to $X_0 = 0$, as the second term in the brackets becomes unity when applying the Leibniz expression:

$$\frac{\pi}{4} = \sum_{m=0}^{\infty} \frac{(-1)^m}{2m+1} \tag{2.11}$$

For the desorption case, we can take the initial concentration within the membrane to be X_∞, i.e. the equilibrium concentration for absorption, and since $X_1 = 0$, we obtain

$$X(y,t) = X_\infty \frac{4}{\pi} \sum_{m=0}^{\infty} \frac{(-1)^m}{2m+1} \exp\left(-D(2m+1)^2 \frac{\pi^2 t}{4d^2} \right) \cos\left((2m+1) \frac{\pi y}{2d} \right) \tag{2.12}$$

Fig. 2.2 shows the concentration gradients, $X(y,t)$, across the film for the absorption process described by Eq. 2.10 (Fig. 2.2A) and the desorption process described by Eq. 2.12 (Fig. 2.2C). The diffusion coefficient was set to $D = 1 \times 10^{-6}\text{cm}^2\text{s}^{-1}$ and the thickness of the film to $d = 0.01cm$. The red traces show the concentration profile in the film at $t = 0.1s$ then from 1 s to 19 s in 2 second increments (blue) and finally from 30-150 s in 15 second increments (black) using (1.10). The curves are separated by a time interval of $\Delta t' = 0.15$ (black curves) and $\Delta t' = 0.02$ (blue) where the reduced time is $t' = Dt/d^2$.

We now evaluate $X(t)$ for two limiting, but common cases. We derive two equations that permit the determination of the diffusion constant from either the average concentration of the analyte in the polymer film or from the concentration near the film-substrate interface. When measuring the temporal evolution of measurement $X(t)$, we can then distinguish between these two cases.

Case (A): the measurement samples only a small sliver of the film (thickness: δy) near the bottom ($y = 0$) or top ($y = d$) surface,

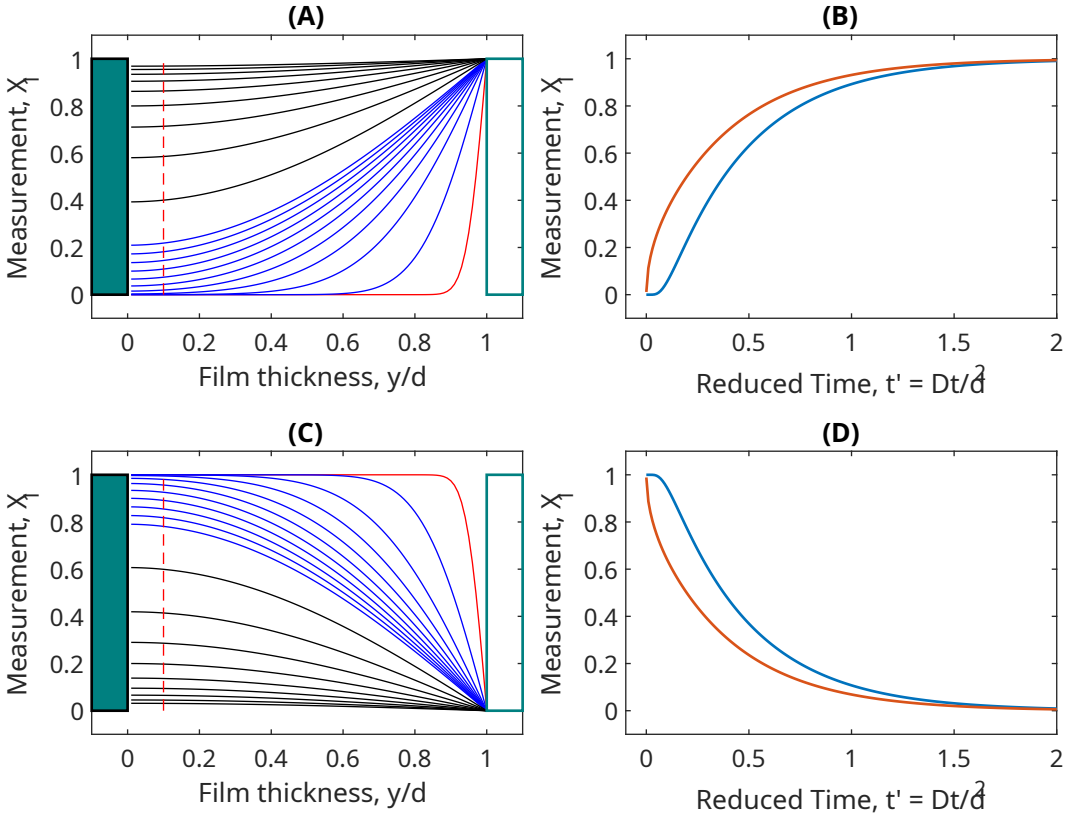

Figure 2.2: (A) Concentration gradient of an analyte in a film mounted on an impermeable substrate as a function of time from $t' = 0.001$ to 1.5. The red curve represents the profile at $t' = 0.001$. Each curve is separated by $\Delta t' = 0.02$ for the lower 10 curves (blue) and by $\Delta t' = 0.15$ for the top 9 curves (black). (B) Uptake curve of an analyte diffusion into a film mounted on an impermeable substrate. The red curve shows the total concentration throughout the film; the blue curve shows its average concentration in the bottom 10% layer of the film. (C) and (D) as in (A) and (B) but for a desorption case.

$$\overline{X}(\delta y, t) = \frac{1}{d} \int_{\substack{y=0 \\ or \\ y=d}}^{\delta y} X(y,t)dy \tag{2.13}$$

Case (B): the measurement samples the concentration of the analyte over the entire film thickness:

$$\overline{X}(t) = \frac{1}{d} \int_{y=0}^{d} X(y,t)dy \tag{2.14}$$

Examples for the first case are measurements of the evanescent wave absorption or fluorescence, or when plasmonic interactions or critical angles are used to determine the film's refractive index near the substrate interface. Case (B) applies when gravimetric or optical density measurements are used to follow the analyte concentration.

2.3.2 Interface concentration (impermeable substrate)

For Case (A) measurements, one integrates Eq. 2.10 between $y = 0$ and δy.

$$\overline{X}(t) = \frac{1}{\delta y}\int_{y=0}^{\delta y} X_\infty \left[1 - \frac{4}{\pi}\sum_{m=0}^{\infty}\frac{(-1)^m}{2m+1}\exp\left(-D(2m+1)^2\frac{\pi^2 t}{4d^2}\right)\cos\left((2m+1)\frac{\pi y}{2d}\right)\right] dy \tag{2.15}$$

which yields

$$\overline{X}(t) = X_\infty \left[1 - \frac{8d}{\pi^2\delta y}\sum_{m=0}^{\infty}\frac{(-1)^m}{(2m+1)^2}\exp\left(-\frac{D\pi^2(2m+1)^2 t}{4d^2}\right)\sin\left((2m+1)\frac{\pi\delta y}{2d}\right)\right] \tag{2.16}$$

For the desorption case, we can perform a similar integration with Eq. 2.12 and the average concentration near the interface is thus given by:

$$\overline{X}(t) = X_\infty \left[\frac{8d}{\pi^2\delta y}\sum_{m=0}^{\infty}\frac{(-1)^m}{(2m+1)^2}\exp\left(-\frac{D\pi^2(2m+1)^2 t}{4d^2}\right)\sin\left((2m+1)\frac{\pi\delta y}{2d}\right)\right] \tag{2.17}$$

Although Eq. 2.16 and 2.17 contain infinite sums of exponential functions, fitting is straightforward, since the arguments of the exponential functions are easily evaluated and the amplitude factors $(-1)^m/(2m+1)^2$ converge quickly to zero. For most scenarios a fit with $m = 3$ to 5 should be sufficient.

2.3.3 Integrated concentration (impermeable substrate)

In Case B the average concentration of the film for absorption can be calculated by integration of Eq. 2.10 across the film's thickness, d, to obtain:

$$\overline{X}(t) = \frac{1}{d}\int_{y=0}^{d} X_{=\infty}\left[1 - \frac{4}{\pi}\sum_{m=0}^{\infty}\frac{(-1)^m}{2m+1}\exp\left(-D(2m+1)^2\frac{\pi^2 t}{4d^2}\right)\cos\left((2m+1)\frac{\pi y}{2d}\right)\right]dy \tag{2.18}$$

which simplifies to

$$\overline{X}\,(t) = X_{\infty}\left[1 - \frac{8}{\pi^2}\sum_{m=0}^{\infty}\frac{1}{(2m+1)^2}\exp\left(-D(2m+1)^2\frac{\pi^2 t}{4d^2}\right)\right] \tag{2.19}$$

Similarly, the average concentration during desorption is given by:

$$\overline{X}\,(t) = X_{\infty}\left[\frac{8}{\pi^2}\sum_{m=0}^{\infty}\frac{1}{(2m+1)^2}\exp\left(-D(2m+1)^2\frac{\pi^2 t}{4d^2}\right)\right] \tag{2.20}$$

Again, the diffusion coefficient, D, may be obtained by fitting as long as the thickness, d, is known.

Fig. 2.2B shows the concentration $X(y,t)$ near the substrate interface, from Eq. 2.16 and the average concentration through the entire film, from Eq. 2.19, whereas Fig. 2.2D shows the respective desorption curves calculated using Eq. 2.17 and 2.20. Fifty exponential terms were included in the calculation of concentration profiles and of $\overline{X}(t)$.

2.4 Film on a permeable support

Absorption and desorption processes involving diffusion into a free-standing film, i.e. having either a fully permeable support or no support, can be described in analogy to the case of the supported film (see Fig. 2.1). The boundary conditions are now given by:

$$\begin{aligned} X\,(0 < y < d, 0) &= f(y) \\ X\,(d,t) &= X_1 \\ X\,(0,t) &= X_2 \end{aligned} \tag{2.21}$$

2.4.1 Concentration gradients for the free-standing film

The general solution of 2.4 with the boundary conditions in Eq. 2.21 is given by

$$X(y,t) = X_2 + (X_1 - X_2)\,\frac{y}{d} + \frac{2}{\pi}\sum_{n=1}^{\infty}\frac{X_1\cos n\pi - X_2}{n}\sin\frac{n\pi y}{d}\exp\left(-\frac{Dn^2\pi^2 t}{d^2}\right) + \frac{2}{d}\sum_{n=1}^{\infty}\sin\frac{n\pi y}{d}\exp\left(-\frac{Dn^2\pi^2 t}{d^2}\right)\int_0^d f\left(y'\right)\sin\frac{n\pi y'}{d}\,\mathrm{d}y' \tag{2.22}$$

Here $f(y)$ describes the initial distribution of analyte within the film. In most absorption experiments $f(y)$ is either equal to zero or a constant. For the two-sided *desorption* process, we consider an initial constant concentration throughout the film, as well as a linear concentration gradient as it might be obtained following one-sided absorption process.

Setting $y = 0$ reduces Eq. 2.22 to $X(0,t) = X_2$ for all times. Similarly, at $t = 0$ equation Eq. 2.22 yields $f(y)$, i.e. the boundary conditions are met.

During absorption, we typically assume that the film is initially free of analyte, $f(y) = 0$ and that the analyte emerging from the low concentration face is carried promptly away, $X_2 = 0$. We can then simplify Eq. 2.22 to obtain

$$X(y,t) = X_1\left[\frac{y}{d} + \frac{2}{\pi}\sum_{n=1}^{\infty}\frac{(-1)^n}{n}\sin\frac{n\pi y}{d}\exp\left(-\frac{Dn^2\pi^2 t}{d^2}\right)\right] \tag{2.23}$$

Fig. 2.3A shows the concentration gradients described by Eq. 2.23 following one-sided absorption into a permeable film, where we assume that the analyte can be completely removed from the opposite surface. Note that the red, blue and black lines correspond to lower time intervals than in Fig. 2.2A,C. The steady-state analyte distribution following one-sided absorption into a permeable membrane (Fig. 2.3A) is simply given by

$$f(y) = \frac{X_1}{d}y \tag{2.24}$$

For the desorption case for the permeable membrane, we may consider two different cases.

We first consider the situation where at the start of the process the linear concentration gradient of Eq. 2.24 is present. The concentration gradients are in this case evaluated using Eq. 2.22 with 2.24, and for $X_1 = X_2 = 0$:

$$X(y,t) = \frac{2X_1}{\pi}\sum_{n=1}^{\infty}\frac{(-1)^n}{n}\sin\frac{n\pi y}{d}\exp\left(-\frac{Dn^2\pi^2 t}{d^2}\right) \tag{2.25}$$

The concentration gradients of the desorption process from Eq. 2.25 are given in Fig. 2.3C. Alternatively, we can consider the case when the analyte within the film is at a constant

uniform concentration X_0, and, as before, the initial conditions are given by $X_1 = X_2 = 0$. Applying these boundary conditions to Eq. 2.22 gives

$$X(y,t) = \frac{4X_0}{\pi}\left[\sum_{m=0}^{\infty}\frac{1}{2m+1}\exp\left(-\frac{D(2m+1)^2\pi^2 t}{d^2}\right)\sin\frac{(2m+1)\pi y}{d}\right] \tag{2.26}$$

These gradients are presented in Fig. 2.3E.

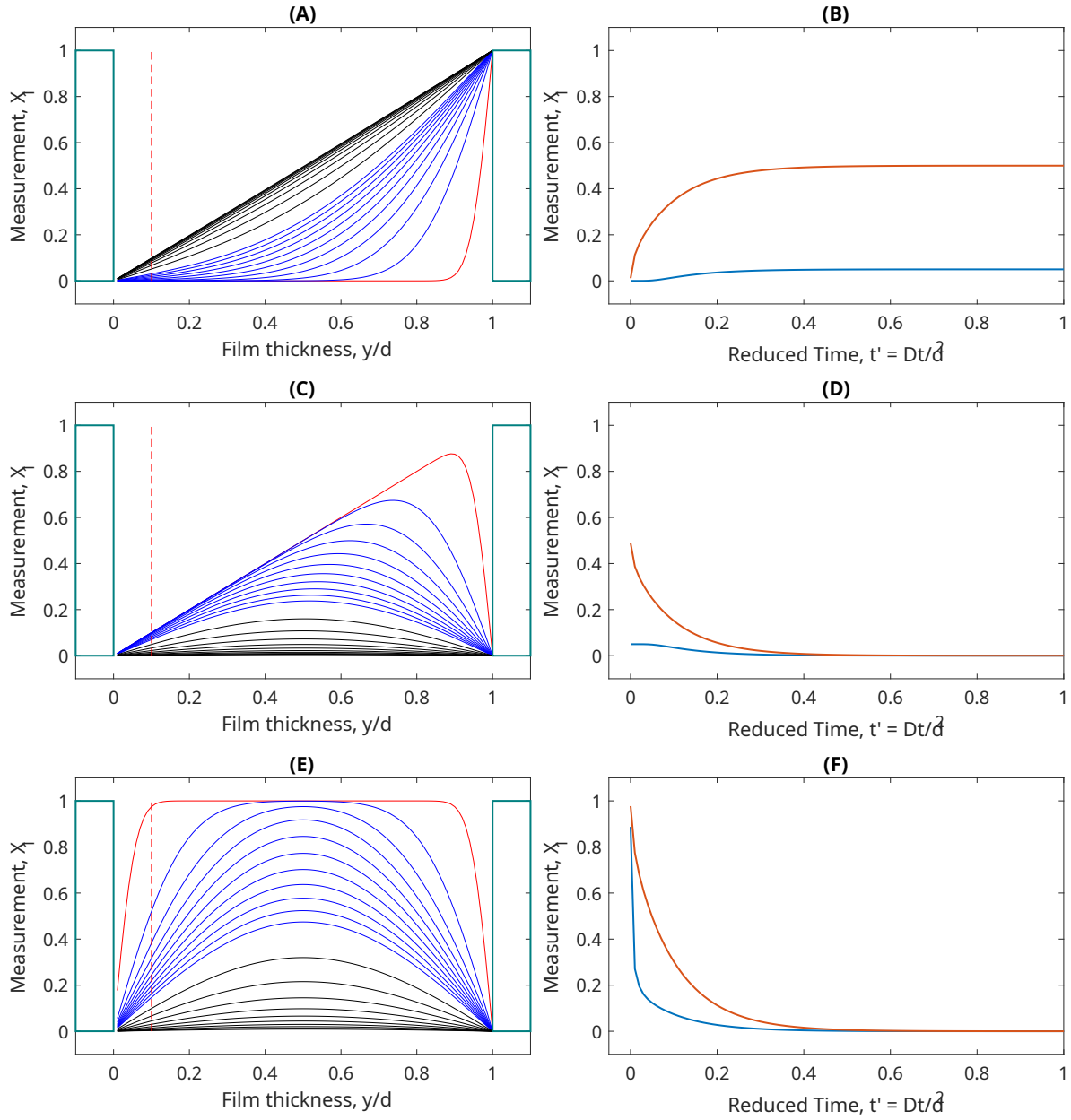

Figure 2.3: (A) Concentration gradient of an analyte in a film mounted on a permeable substrate as a function of time from $t' = 0.001$ to 0.5. The red curve represents the profile at $t' = 0.001$. Each curve is separated by $\Delta t' = 0.01$ for the lower 10 curves (blue) and by $\Delta t' = 0.04$ for the top 10 curves (black). (B) Uptake curve of an analyte diffusion into a film mounted on a permeable substrate. The red curve shows the total concentration throughout the film; the blue curve shows its average concentration in the bottom 10% layer of the film. (C) and (D) show the desorption curves with a permeable membrane for a case of linear initial concentration. (E) and (F) show the desorption curves for a uniform initial concentration.

2.4.2 Analyte flow through the permeable film

Many researchers determine the diffusion constant, and the solubility of the analyte in the film using the rate, dQ/dt, at which the analyte emerges from the low-concentration side of the film. The total analyte emerging from the film is given by [1]

$$\frac{dQ}{dt} = D\left(\frac{\partial X}{\partial y}\right)_{y=0} \tag{2.27}$$

and can then be determined from Eq. 2.22 with $f(y) = X_0$ as

$$\begin{aligned} Q = D\left(X_1 - X_2\right)\frac{t}{d} + \frac{2d}{\pi^2}\sum_{n=1}^{\infty}\frac{X_1\cos n\pi - X_2}{n^2}\left(1 - \exp\left(-\frac{Dn^2\pi^2 t}{d^2}\right)\right) \\ + \frac{4X_0 d}{\pi^2}\sum_{m=0}^{\infty}\frac{1}{(2m+1)^2}\left(1 - \exp\left(-\frac{D(2m+1)^2\pi^2 t}{d^2}\right)\right) \end{aligned} \tag{2.28}$$

In most experiments the analyte concentration can initially be set to zero, $X_0 = 0$, and the concentration at the low concentration side of the film can also assumed to remain zero, $X_2 = 0$ so that Eq. 2.28 is simplified to

$$\frac{Q}{X_1 d} = \frac{Dt}{d^2} - \frac{1}{6} - \frac{2}{\pi^2}\sum_{n=1}^{\infty}\frac{(-1)^n}{n^2}\exp\left(-\frac{Dn^2\pi^2 t}{d^2}\right) \tag{2.29}$$

At steady state $t \to \infty$ and all exponential terms in Eq. 2.29 tend to zero. Only the first two terms remain, giving a linear concentration gradient between the top and bottom surface of the film.

$$X(y, \infty) = X_2 + \left(X_1 - X_2\right)\frac{y}{d} \tag{2.30}$$

With an average concentration of

$$\overline{X}_{\infty} = \frac{X_1 + X_2}{2} \tag{2.31}$$

This forms a steady-state concentration gradient that is maintained even though analyte continues to flow through the film. From Eq. 2.29 the production at steady state is given as

[1] This equation differs from Crank's equation by a negative sign due to our coordinate system that places the high-concentration, X_1, side of the film at the position $y = d$.

$$Q = \frac{DX_1}{d}\left(t - \frac{d^2}{6D}\right) \tag{2.32}$$

The flow rate at steady state is constant at

$$\frac{dQ}{dt} = \frac{DX_1}{d} \tag{2.33}$$

and depends on the analyte concentration, X_1, at the top ($y = d$) of the film. The diffusion constant can also be determined from the time lag, i.e. the intercept of Eq. 2.32:

$$L = \frac{d^2}{6D} \tag{2.34}$$

which no longer depends on the concentration.

2.4.3 Interface Concentration (free-standing film)

Although the concentrations at the top and bottom surface of the film are bounded by equation Eq. 2.21 to give X_1 and X_2, respectively, it is for some experiments important to consider the concentration in a small sliver of the film as it might be interrogated by e.g. surface-specific optical techniques.

Similar to the impermeable membrane, we can find the average analyte concentration for absorption within a region defined by y_1 and y_2 through integration of Eq. 2.22 with $f(y) = X_0$ to obtain:

$$\overline{X}(t) = X_2 + \frac{1}{y_2 - y_1}\left[\begin{array}{l} \dfrac{(X_1 - X_2)}{2d}\left(y_2^2 - y_1^2\right) \\ -\dfrac{2d}{\pi^2}\displaystyle\sum_{n=1}^{\infty}\frac{X_1\cos n\pi - X_2}{n^2}\left(\cos\frac{n\pi y_2}{d} - \cos\frac{n\pi y_1}{d}\right)\exp\left(-\frac{Dn^2\pi^2 t}{d^2}\right) \\ -\dfrac{4dX_1}{\pi^2}\displaystyle\sum_{m=0}^{\infty}\frac{1}{(2m+1)^2}\left(\cos\frac{(2m+1)\pi y_2}{d} - \cos\frac{(2m+1)\pi y_1}{d}\right) \\ \times\exp\left(-\dfrac{D(2m+1)^2\pi^2 t}{d^2}\right) \end{array}\right] \tag{2.35}$$

Assuming that all analyte which is exiting the film is carried away ($X_2 = 0$) and that the initial concentration throughout the film is $X_0 = 0$, the equation for the absorption process becomes:

$$\frac{\overline{X}(t)}{X_1} = \frac{(y_2^2 - y_1^2)}{2d\,(y_2 - y_1)} - \frac{2d}{(y_2 - y_1)\,\pi^2} \sum_{n=1}^{\infty} \frac{(-1)^n}{n^2} \left(\cos \frac{n\pi y_2}{d} - \cos \frac{n\pi y_1}{d} \right) \exp\left(-\frac{Dn^2\pi^2 t}{d^2} \right) \tag{2.36}$$

Within the range of the evanescent interactions ($y_1 = 0; y_2 = \delta y$), we obtain the simple expression for an analyte uptake process

$$\overline{X}(\delta y, t) = X_1 \left[\frac{\delta y}{2d} + \frac{2d}{\delta y \pi^2} \sum_{n=1}^{\infty} \frac{(-1)^n}{n^2} \left(1 - \cos \frac{n\pi\delta y}{d} \right) \exp\left(-\frac{Dn^2\pi^2 t}{d^2} \right) \right] \tag{2.37}$$

which approaches asymptotically the constant concentration

$$\overline{X}(\delta y, \infty) = \frac{\delta y}{2d} X_1 \tag{2.38}$$

The blue line in Fig. 2.3B describes the time evolution of the measured concentration according to Eq. 2.37.

For the two desorption cases ($X_1 = X_2 = 0; f(y) \neq 0$) mentioned above, we can, again, consider a constant initial concentration, $X_0 = \overline{X}(\delta y, \infty)$. Within the range of evanescent interaction, we obtain the integrated expression:

$$\overline{X}(t) = \overline{X}(\delta y, \infty) \frac{4d}{\delta y \pi^2} \left[\sum_{m=0}^{\infty} \frac{1}{(2m+1)^2} \left(1 - \cos \frac{(2m+1)\pi\delta y}{d} \right) \exp\left(-\frac{D(2m+1)^2\pi^2 t}{d^2} \right) \right] \tag{2.39}$$

The blue line in Fig. 2.3D describes the time evolution of the measured concentration according to Eq. 2.39.

Alternatively, we can consider the case with a linear concentration gradient described by Eq. 2.24, and perform a similar integration of Eq. 2.25 within the range of the evanescent field to obtain

$$\overline{X}(t) = X_1 \left[\frac{2d}{\delta y \pi^2} \sum_{n=1}^{\infty} \frac{(-1)^n}{n^2} \left(\cos \frac{n\pi\delta y}{d} - 1 \right) \exp\left(-\frac{Dn^2\pi^2 t}{d^2} \right) \right] \tag{2.40}$$

This time evolution is given by the blue line in Fig. 2.3F.

2.4.4 Integrated concentration (free-standing film)

When calculating the concentration of analyte upon one-sided absorption into a freestanding film, the average concentration of the analyte across the entire film can be calculated as a function of time by integration of Eq. 2.22 across the film's thickness, d. The average analyte concentration upon absorption is then given by

$$\overline{X}(t) = X_1 \left[\frac{1}{2} - \frac{2}{\pi^2} \sum_{n=1}^{\infty} \frac{1}{n^2} \left(1 - (-1)^n\right) \exp\left(-\frac{Dn^2\pi^2 t}{d^2}\right) \right] \tag{2.41}$$

which can be simplified by omitting all terms with zero value from the sum:

$$\overline{X}(t) = X_1 \left[\frac{1}{2} - \frac{4}{\pi^2} \sum_{m=0}^{\infty} \frac{1}{(2m+1)^2} \exp\left(-\frac{D(2m+1)^2\pi^2 t}{d^2}\right) \right] \tag{2.42}$$

where we, again, assumed that $X_2 = 0$ and that the initial concentration is $X_0 = 0$. The red line in Fig. 2.3B describes the time evolution of the measured concentration in Eq. 2.42.

For the desorption process we, first, consider a uniform initial concentration, $X_0 = X_\infty$. With $X_1 = X_2 = 0$, we have

$$\frac{\overline{X}(t)}{\overline{X}(d,\infty)} = \frac{8}{\pi^2} \sum_{m=0}^{\infty} \frac{1}{(2m+1)^2} \exp\left(-\frac{D(2m+1)^2\pi^2 t}{d^2}\right) \tag{2.43}$$

The red line in Fig. 2.3D describes the time evolution of the measured concentration according to Eq. 2.43. If we, instead, start out with a concentration gradient as in Eq. 2.24, the average analyte in the film during desorption is given by:

$$\frac{\bar{X}(t)}{X_1} = \frac{4}{\pi^2} \sum_{m=0}^{\infty} \frac{1}{(2m+1)^2} \exp\left(-\frac{D(2m+1)^2\pi^2 t}{d^2}\right) \tag{2.44}$$

This time evolution is given by the red line in Fig. 2.3F. In all figures shown here, we included fifty exponential terms.

2.5 Summary

It may be surprising that a discussion of one-dimensional diffusion processes is of relevance nearly 70 years after Crank laid the foundation of the mathematical models. This discussion should have been published 65 years ago. And, yet, it appears that the exact numerical models collected and provided by Crank have either been forgotten or have not been commonly applied. We hope that our work may help those who need to extract accurate diffusion constants from experimental data, and believe that future diffusion models no longer have to rely on a first-order approximation as given in Eq. 2.1.

The equations derived in this chapter are used to fit to the sorption curves obtained with the nanohole array gas sensing setup described in Chapter 3.

Appendix A.1 provides the equations presented in this chapter as Matlab functions to which experimental data may be fit. The average concentrations are calculated either by integrating over a small sliver of the film or over the entire film. The former is relevant, for example, for evanescent field or plasmonic interaction measurements (index "ev"). The latter pertains to gravimetric, optical absorption or bulk refractive index measurements of concentration (index: "film").

Chapter 3

Detection of volatile organic compounds using metallic flow-through nanohole arrays

This chapter describes a real-time, on-line, continuous, cost-effective VOC sensing system that is based on the phenomenon of extraordinary optical transmission (EOT). The results presented in this chapter are analyzed and modeled using the equations derived in Chapter 2 to investigate the diffusion of o-xylene into PDMS. Many parts of this chapter are found in an article, submitted for publication, in collaboration with researchers at Queen's University. This chapter begins with an introduction of the sensing principle of using nanoholes to detect VOCs, then provides a detailed description of the experimental setup and methods used in the chapter. Finally, the results and a discussion of the experimental methods and results are provided.

3.1 Introduction

The detection of anthropogenic and biogenic volatile organic compounds (VOCs) is an important field in gas phase analysis and is relevant to, for example, food production, environmental monitoring, health care and industrial processes [43, 44, 45, 46, 47, 48, 49]. Benzene, toluene, ethylbenzene and xylenes (BTEX) form a subcategory of VOCs, whose monitoring is of particular importance as they pose a potent risk to human health at high concentration and/or prolonged exposure. Health risks include but are not limited to respiratory diseases, reproductive adversities, and cancer [50, 51].

BTEX compounds are typically detected and quantified using separation techniques such as gas chromatography mass spectrometry (GC-MS) [52, 53, 54], high-performance liquid chromatography (HPLC) [52], and capillary electrophoresis (CE) [55]. Samples can be controllably enriched in BTEX concentrations using Solid-Phase Micro-Extraction (SPME), a rapid, solvent-free sample preparation method pioneered by the Pawliszyn group and others

[56, 57]. In solid-phase micro-extraction (SPME), the extraction efficiency and analytical reliability critically depend on the diffusion kinetics of analytes through the polymer coating, most commonly polydimethylsiloxane (PDMS) [58]. During SPME, volatile organic compounds (VOCs) partition from the sample phase into the PDMS layer, where they diffuse until equilibrium or a quasi-steady state is reached. The rate and extent of this diffusion fundamentally determine how rapidly the coating accumulates analyte, the sensitivity and linearity of the extraction process, and whether equilibrium is achieved within practical sampling times [59, 58].

Polydimethylsiloxane (PDMS) is a commonly used extraction matrix for SPME. It is an elastic, chemically inert, hydrophobic polymer with optical transparency in the ultraviolet-visible (UV-Vis) region of light [60, 61] . PDMS, like other silicon-based inorganic polymers, bears a strong affinity to non-polar molecules. This allows VOCs to be readily absorbed into the polymer causing physical and chemical changes [62, 34]. For instance, the uptake of VOCs into PDMS results in the alteration of its refractive index. The increase or decrease of RI of the polymer is strongly dependent on the VOC optical properties, solvent-polymer affinity, and sorption kinetics [34, 63]. To optimize PDMS-SPME probes for optimum extraction time and film thickness, it is important to understand the diffusion kinetics of these compounds through PDMS.

The diffusion kinetics through PDMS have previously been investigated through gravimetric sensors [40, 64, 65], time-lag permeation [66], and through the measurement of refractive index and swelling using a interferometric refractometer [35, 34]. Gravimetric sorption methods are among the most direct approaches, relying on the precise measurement of mass uptake as VOCs partition into a PDMS film over time. In such experiments, the polymer sample is exposed to a controlled vapor environment, and the time-dependent mass increase is recorded using a sensitive microbalance or quartz crystal microbalance (QCM) [40, 64]. The time-lag permeation method measures diffusion coefficients by monitoring the delay (time lag, θ) before a permeating VOC first appears on the downstream side of a polymer membrane after exposure to a constant concentration on the upstream side. The diffusion coefficient D is then calculated from this lag time using $D = l^2/6\theta$, where l is the membrane thickness [66]. More recently, interferometric refractometry has emerged as a powerful optical approach for probing VOC diffusion in real time by measuring the refractive index and thickness changes to a thin polymer film upon the absorption of different VOCs [35]. With this method, a thin polymer film is deposited on a reflective substrate that acts as an optical cavity. The refractive index and thickness measurement were obtained by capturing the interference pattern of the Fresnel reflected light near the critical angle.

Although there has been numerous studies conducted to investigate the diffusion kinetics of VOCs, there is a significant spread in the reported values for these constants. For example, the diffusion constants for xylene vary in two orders of magnitude, with reported values between $3 \times 10^{-8}\text{cm}^2\text{s}^{-1}$ to $1.2 \times 10^{-6}\text{cm}^2\text{s}^{-1}$ [40, 65, 67, 34].

In this chapter, we present a real-time, on-line, continuous, cost-effective VOC sensing method that is based on the phenomenon of extraordinary optical transmission (EOT) to investigate the diffusion kinetics of o-xylene into PDMS.

3.1.1 Extraordinary optical transmission through nanohole arrays

When light is incident on a periodic metal array of apertures, the SPPs are excited on the surface due to grating coupling of the incident light. The energy from the enhanced field at the surface tunnels through the apertures and is scattered into the far field in transmission. We can derive an expression for location of the EOT resonances by considering the momentum-matching condition to allow for their propagation.

The emergence of SPPs can be explained by applying Maxwell's equations to a simple geometry where we have light incident on a single flat interface consisting of a non-absorbing dielectric with a positive dielectric constant ε_d, and a conductive metallic layer with dielectric function ε_m, in which the $Re[\epsilon_m] < 0$. In the following, I summarize the relations as presented in reference [68] and [69].

If we are to apply Maxwell's equations and the appropriate boundary conditions for the case of transverse magnetic (TM) mode incident on the boundary, we can solve for the dispersion relation, k_{SPP}, for a SPPs propagating at the interface

$$k_{SPP} = k_0 \sqrt{\frac{\varepsilon_d \varepsilon_m}{\varepsilon_d + \varepsilon_m}} \tag{3.1}$$

where k_0 is the magnitude of the incident wave-vector. The real part of the dispersion equation is always less than the light line, implying that the SPP mode is evanescent and cannot be directly excited by propagating light as the free-space photon does not have enough in-plane momentum. To excite the SPP modes, an additional momentum component $\mathbf{G}$ along the SPP propagation plane is required and provides the phase matching conditions required for the excitation of these modes. For extraordinary optical transmission, this additional momentum is provided by the periodic structure of the apertures, and we can express the condition by:

$$\mathbf{k}_{SPP} = \mathbf{k}_{||} \pm \mathbf{G}_{mn} \tag{3.2}$$

where $\mathbf{k}_{||}$ is the in-plane momentum of the incident light, and $\mathbf{G}_{mn}$ is the reciprocal-lattice vector of the structure. In most cases, we consider normally incident light, thus $\mathbf{k}_{||} = 0$, and the above condition simplifies to a simple scalar condition given by:

$$k_{SPP} = |\mathbf{G}_{mn}| \tag{3.3}$$

If we consider a hexagonal lattice structure, the corresponding reciprocal basis vectors and reciprocal-lattice vector are given by

$$\mathbf{b}_1 = \frac{2\pi}{a}\left(1, -\frac{1}{\sqrt{3}}\right), \quad \mathbf{b}_2 = \frac{2\pi}{a}\left(0, \frac{2}{\sqrt{3}}\right), \quad \mathbf{G}_{mn} = m\mathbf{b}_1 + n\mathbf{b}_2 \tag{3.4}$$

where a is the pitch of the structure. The magnitude of the lattice vector is

$$|\mathbf{G}_{mn}| = \frac{2\pi}{a\sqrt{\frac{4}{3}\left(m^2 + mn + n^2\right)}} \tag{3.5}$$

Using Equations (3.1), (3.3) and (3.5), we can apply the momentum-matching conditions to derive an approximation for the EOT resonance peak positions at normal incidence:

$$\lambda_{\max,mn} = \frac{a}{\sqrt{\frac{4}{3}\left(m^2 + mn + n^2\right)}}\sqrt{\frac{\varepsilon_m \varepsilon_d}{\varepsilon_m + \varepsilon_d}} \tag{3.6}$$

where m and n are scattering orders of the array. It should be noted that the above equation does not consider the presence of the holes, Fabry-Perot effects and its associated losses.

This expression highlights two key dependencies: (i) the geometrical parameters of the two-dimensional array (periodicity and symmetry), and (ii) the refractive index of the adjacent medium. The latter is particularly relevant for sensing applications, as changes in the local refractive index shift the resonance condition, which can be observed as spectral shifts in the transmission spectrum.

In this chapter, we demonstrate the use of a PDMS-covered nanohole arrays as a novel VOC sensing method. With the high time-resolution and high sensitivity that this sensor affords, we obtain insights into the diffusion kinetics of o-xylene into PDMS. The kinetics of o-xylene diffusion through a thin layer of PDMS are investigated by measuring the peak-shift of the plasmonic signal. The increase of the refractive index of PDMS with o-xylene concentration is analyzed using a new one-dimensional diffusion model based on a rigorous

integration of Fick's Laws of Diffusion, presented in Chapter 2.

3.2 Methods

The overall setup for the nanohole array gas sensor system can be separated into three groups: the NHA chamber with the PDMS-coated nanohole arrays, the optical setup to interrogate the NHAs in a transmission-based geometry, and the analyte-loading gas flow system to introduce the VOCs to the NHA chamber. This experiment was carried out at both Queen's University at Dr. Carlos Escobedo's lab and then at the Loock Laser Lab at the University of Victoria (UVic). Both systems had similar optical and NHA chamber designs, but the gas flow setup at Queen's used a gas bubbler to introduce the analyte to the chamber, which was later replaced with a nebulizer system at the University of Victoria. A detailed description of the setup is provided below.

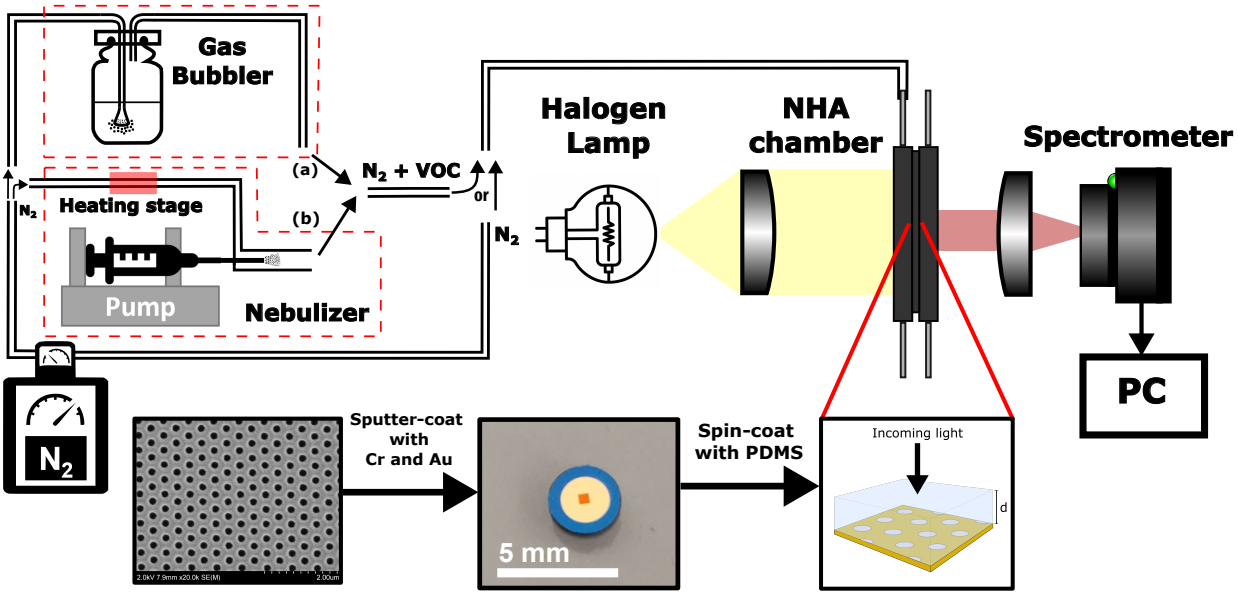

Figure 3.1: Schematic overview of the setup with the NHA preparation, nebulization stage and optical setup.

3.2.1 Optical setup

The optical transmission of the nanohole array gas sensor comprises of a simple spectrometer design as shown in Figure 3.1. It uses a halogen lamp (Ocean Optics HL-2000, USA) as a broadband light source, with a set of collimating optics to direct the collimated light on top

of the NHA structure and to focus the transmitted light onto a UV-Vis spectrometer (Ocean Optics, USB4000, USA).

A similar optical setup was used for both the Queen's and UVic system, with a different set of collimating optics. The Queen's setup used a 10x objective lens and a biconvex lens with an iris, while the UVic optical setup was mounted onto a 30 mm cage system, with the use of two plano-convex lens (f = 50.2 mm), and fiber collimation package for the fiber-coupled spectrometer for ease of alignment.

3.2.2 Nanohole array fabrication and assembly

The nanohole array chamber consisted of an array of sub-wavelength nanoholes that were spin-coated with a layer of polydimethylsiloxane (PDMS), and placed in a custom 3D printed chamber that allowed the flow of gas over or under the nanoholes.

The plasmonic NHA sensor head was prepared from a commercial sample-mounting grid designed for transmission electron microscopy that we coated with gold. The sample-mounting grid (Prod No. 21586-10, Ted Pella Inc., USA) consisted of 450 μm $\times$ 450 μm perforated area with 200 nm holes arranged in hexagonal pattern with a pitch of 400 nm on a 200 nm thick Si_3N_4 substrate. The nanohole grid was plasma-cleaned for 60 s and sputter coated, first, with 5 nm of Cr as an adhesion layer and then, with 100 nm of gold. A scanning electron micrograph (SEM) image was obtained of the coated structure, and the average radius and pitch were measured to be (99 ± 3) nm and (407 ± 6) nm respectively (Fig. 3.2). The average pitch was measured through image analysis of the x20k magnification image to determine the spacing between the holes, while the average radius was measured from the area of the holes in the x45k magnification image to account for shape irregularities.

3.2.3 PDMS layer

The depth range of the refractive index measurement is governed by the penetration depth of the surface plasmons; thus, it is essential to have a strong adhesion between the PDMS and the gold layer.

Polydimethylsiloxane (PDMS) is a silicon-based polymer consisting of a repeating siloxane backbone $-[Si(CH_3)_2-O]_n-$ with methyl side groups (Fig. 3.3). This molecular structure provides PDMS with a unique combination of flexibility, chemical inertness, and low surface energy due to the presence of nonpolar methyl groups. The chemistry of this backbone, along with the ability to modify the surface by plasma or chemical treatments, determines how PDMS interacts with substrates such as glass and gold.

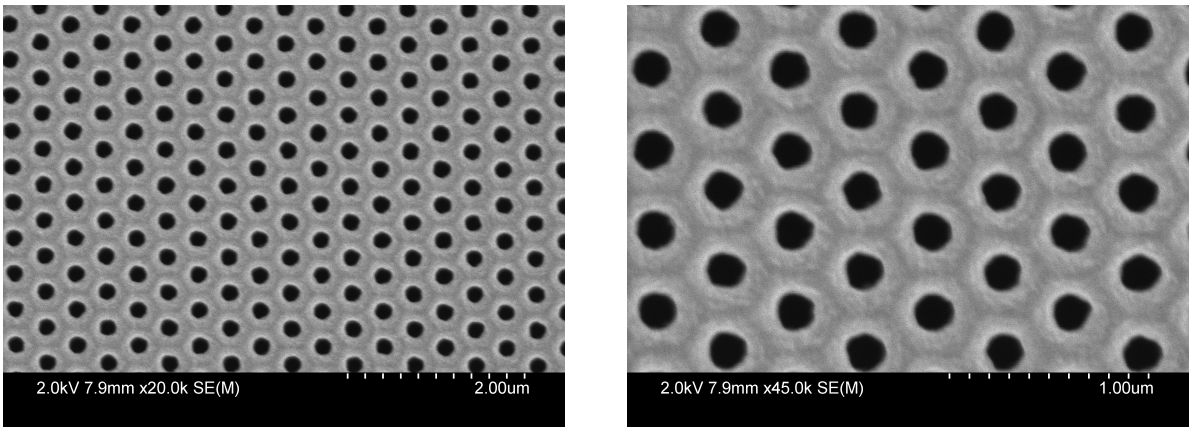

(a) x20k magnification (b) x45k magnification

Figure 3.2: Scanning electron micrograph of nanohole array

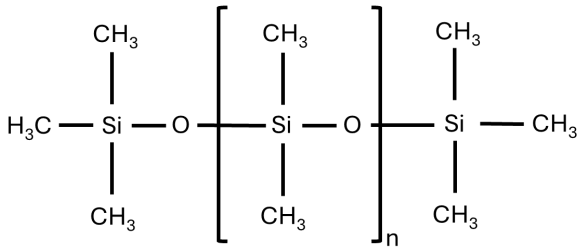

Figure 3.3: Molecular structure of PDMS

When PDMS is bonded to glass, both surfaces are activated using an oxygen plasma. The plasma oxidizes the surface of PDMS, creating a thin silica-like (SiOx) layer that contains silanol (Si–OH) groups, while also creating similar silanol groups on the glass surface. When these activated surfaces are brought into contact, condensation reactions occur between silanol groups to form covalent siloxane (Si–O–Si) linkages, resulting in a permanent bond. This mechanism explains why plasma-activated PDMS, and glass form robust, often irreversible seals widely used in microfluidics and optics applications.

In contrast, gold presents a chemically inert, nonhydroxylated surface. Plasma-activated PDMS does not have compatible functional groups to covalently react with gold, leaving only weak van der Waals interactions at the interface. As a result, PDMS bonds poorly to gold films compared to glass, with detachment being a common issue in hybrid microfluidic and plasmonic devices.

As gold surfaces have weak interactions with PDMS, two different self-assembled monolayers were tested to improve adhesion between the two surfaces:

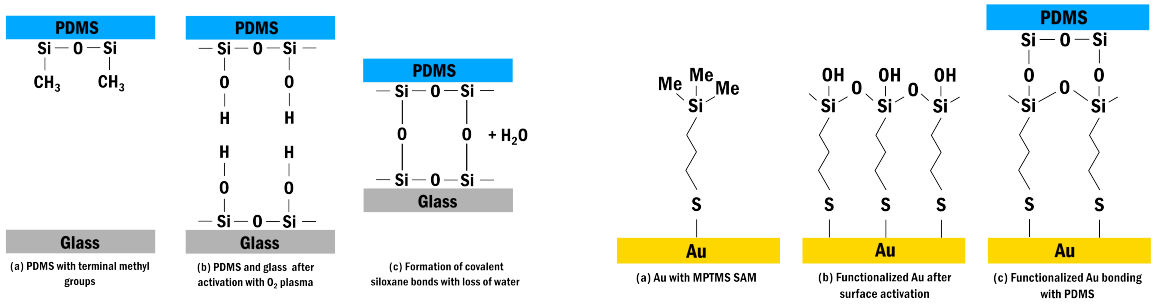

Figure 3.4: Comparison of bonding mechanism of PDMS with glass (left) and gold (right)

(3-mercaptopropyl) trimethoxysilane (MPTMS) and 11-mercaptoundecanoic acid (11-MUA). Both are thiol-based molecules that are commonly used as a molecular adhesive. With MPTMS, The three activated methoxy functional groups form siloxane bonds with PDMS, while the thiol functional group can bind to the Au surface. To test the effectiveness of the adhesion improvement, a peel and tape test were performed. The peel test used a pair of tweezers to see how easy it was to remove PDMS layer off a gold substrate with the different functionalizations. This was subjectively ranked from 1 to 5, with 1 being the weakest adhesion between the two layers. The tape test affixed an adhesive tape onto the surface, and the percentage of PDMS detached from the substrate was recorded. Table 3.1 summarizes the results from the two testing methods. The monolayer of MPTMS showed consistent improvement in the adhesion in all but one samples, while also out-performing the 11-MUA in the tape test for most samples. It was concluded that a self-assembling monolayer of MPTMS provided the better improvement to the adhesion and was used for the rest of the experiments. A further study of adhesion between different SAMs was conducted using a piezoresistive sensing setup, which confirmed that MPTMS showed the most improved bonding strength and reproducibility [70].

To apply the PDMS layer, the gold-coated NHAs were submerged in a 10 mM ethanolic solution of MPTMS for 20 hours to produce an MPTMS monolayer. The MPTMS was then activated via plasma cleaning for 60 s before a PDMS layer (Dow Corning Sylgard 184, 10:1 mixing ratio) was spin coated onto the NHA directly thereafter. Here, the NHA was mounted onto the spin-coater, the PDMS was dropped onto the NHA, and the NHA was spin coated with the desired thickness - here 10 μm. After spin coating, the PDMS film was cured for 10 min at 100°C and 20 min at 70°C on a hotplate. The thickness was set according to a calibration curve obtained using an optical profiler as described in the next section.

Table 3.1: Summary of results testing the effectiveness of MPTMS and 11-MUA in improving the adhesion between gold and PDMS

Time	**Condition**	**MPTMS**	**11-MUA**
18 hours	Plasma	Peel – 3.5 Tape – 0%	Peel – 1.5 Tape – 100%
	No plasma	Peel – 3 Tape – 20%	Peel – 3.5 Tape – 0%
24 hours	Plasma	Peel – 1 Tape – 100%	Peel – 3 Tape – 100%
	No plasma	Peel – 3 Tape – 10%	N/a
48 hours	Plasma	Peel – 2.5 Tape – 0%	Peel – 2 Tape – 50%
	No plasma	Peel – 3.5 Tape – 0-20%	Peel – 3 Tape – 0%

3.2.4 Thickness measurement

The thickness of the PDMS is determined by the spin speed and time of the spin-coater. Initially, we used a home-built spin coater at Queen's University, and later a commercial spin-coater at the University of Victoria. The PDMS coating was applied in 3 phases, with an initial acceleration phase of 5 s, followed by a constant spin speed (between 1000-8000 rpm) phase of variable time (1-10 mins), followed by a final deceleration phase of 10 s.

Due to a lack of surface profilometer instrumentation, the thickness of the PDMS layer in the samples tested at Queen's were not measured prior to the sorption runs. The PDMS layer were measured retroactively to be about 40 μm, i.e much thicker that the intended target of 10 μm.

The spin-coater at UVic was calibrated to produce reproducible PDMS film thicknesses. The film thickness was determined by different spin speeds and coating times using an optical profiler (Contour GT-X, Bruker). Fig. 3.5 shows the obtained calibration curve and 3D profile of the PDMS film of the nanohole array used for the experiment. Note that the vertical axis is on a much-expanded scale compared to the in-plane dimensions. The PDMS film in the experiments forms a smooth surface and has a thickness of 10.2 μm $\pm$ 2.8 μm. This film was spun at 5000 RPM for 1 min.

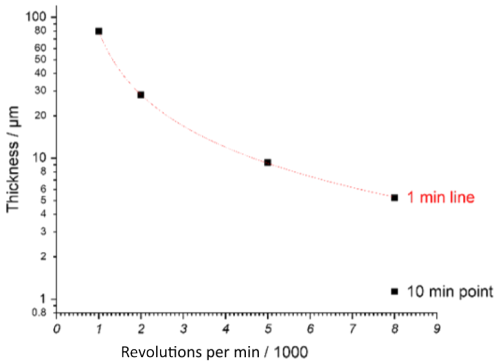

(a) Calibration curve for film thickness

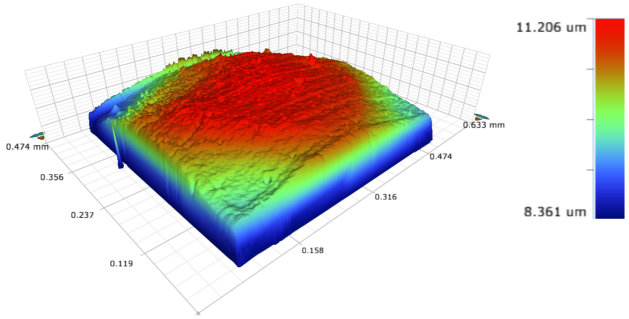

(b) Heat map plot of the surface of a PDMS spin-coated NHA

Figure 3.5: Surface profile and thickness calibration of PDMS layer

3.2.5 NHA chamber

The PDMS-NHA structure was enclosed in a 3D printed in-house built chamber that allows the transmission of light through the center of the chamber and allows for the gases to flow on top of the PDMS-NHA structure. It consists of three main parts, i.e. two outer plates and one central disc that holds the NHA (Fig. 3.6).

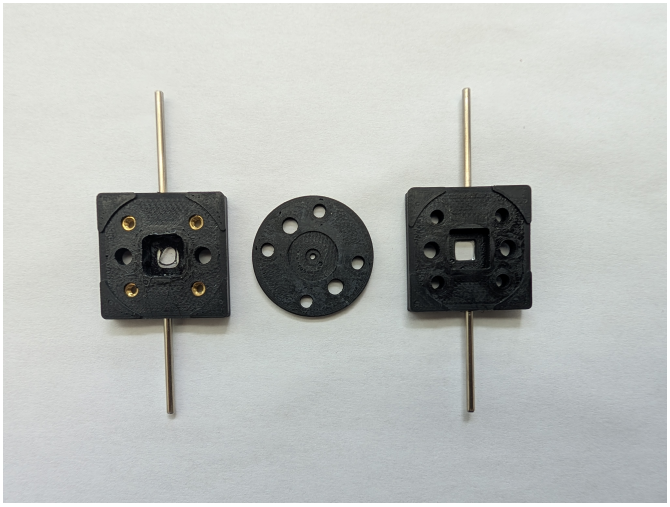

Figure 3.6: 3D printed NHA chamber

The chamber holding the PDMS-coated NHA was designed in-house and resin-printed using a 3D printer. It consists of three main parts, i.e. two outer plates and one central disc with a slot that holds the NHA. The plates have a 5 mm x 5 mm square open hole that

is turned into an optical window using coverslip squares (Fisher Scientific, USA) that are attached and sealed using epoxy resin. Facing inside, each plate has a square center recess that forms the sample chamber. The sample chamber accepts sample gas through a bore connected with 22 needle gauge tubing to the aerosol generator, while the second bore directs the sample gas to waste after it has flown across the PDMS film which faces the white light source. The right part of the chamber (Figure 3.6) has a similar design and, therefore, also permits gas flow across the silicon nitride grid that forms the support for the NHA assembly.

3.2.6 Gas bubbler flow system

With the initial setup at Queen's University, a gas bubbler was used to introduce the solvent vapor into the carrier gas. In this setup, nitrogen gas is directed into a solvent (the VOC analyte) reservoir, where it forms bubbles that rise through the liquid. As the bubbles travel, solvent molecules evaporate into the gas phase, producing an analyte-containing gas at the outlet (see Figure 3.1). The analyte concentration can be approximated from the solvent's vapor pressure and the total system pressure, assuming ideal equilibrium conditions and full saturation of the gas with the solvent vapor.

In practice, complete equilibration between the solvent and carrier gas is not always achieved, and multiple bubblers in series are often used to prevent undersaturation. The actual analyte concentration depends strongly on the residence time of the bubbles, the solvent viscosity, vapor pressure, and the gas flow rate. Due its dependence on many of these factors, it was difficult to achieve control of the analyte concentration in the gas stream with a single gas bubbler.

3.2.7 Nebulizer system

To generate a more defined VOC load of the carrier gas, a co-axial nebulizer system was developed and set up at the University of Victoria.

The nebulizer itself consists of two co-axially mounted capillaries, with the inner capillary supplying the liquid VOC through a syringe pump. Due to the steep pressure gradient, strong shear forces are exerted on the liquid at the tip of capillary. This leads to the dispersion of the ejected liquid into a fine mist, i.e. it is nebulized. The flow of heated nitrogen gas from the surrounding larger capillary carries the mist towards the sample chamber while ensuring complete evaporation of the VOC. Since the liquid and gas flow rates can be tightly controlled, the VOC partial pressure of the sample gas can be finely adjusted.

The performance of the nebulizer is dependent on several design parameters that govern

the atomization process due the presence of the shear forces at the tip of the capillary. The gas flow rate and pressure govern the velocity and shear forces where the gas interacts with the liquid stream as it exits the inner capillary. Higher gas velocities enhance droplet breakup through increased shear, resulting in finer aerosol generation, but may also lead to excessive dispersion or undesired turbulence. To investigate the performance of the nebulizer, a Computational Fluid Dynamics (CFD) simulation (Ansys Fluent, USA) was performed and coupled to a finite element analysis (Fusion360) using the experimental dimensions using the experimental dimensions, with the results shown in Fig. 3.7. The pressure is set to 15 bar which produces a N_2 gas velocity of 50,000 ft/min (or 250 m/s). The outer capillary has an inner diameter of 0.8 mm, while the inner capillary has an inner and outer diameter of 0.4 mm and 0.7 mm respectively.

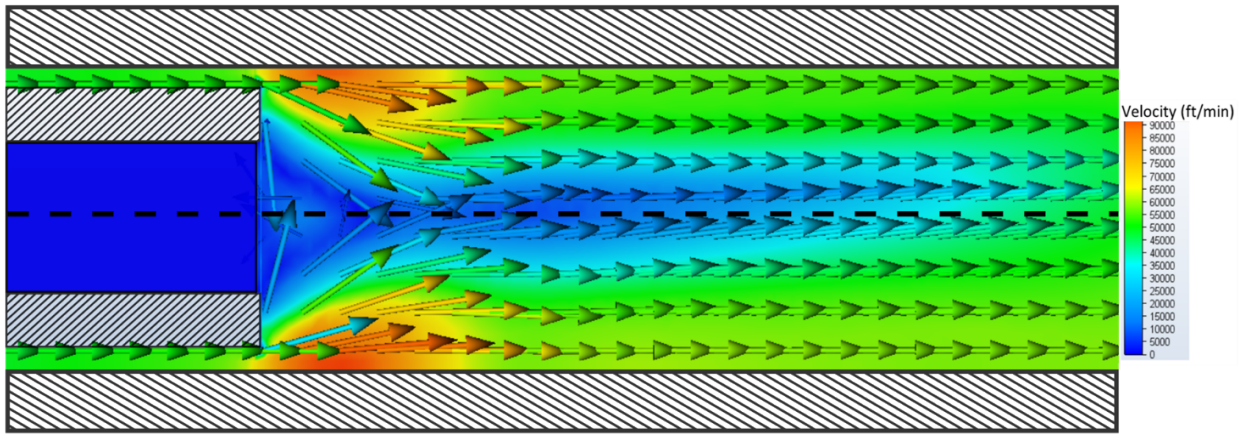

Figure 3.7: CFD simulation of the coaxial nebulizer.

We observe a strong velocity gradient at the tip of the inner capillary which indicates there exists effective shear forces for atomizing the liquid. The pressure was simulated as 15 bar which shows a narrow and symmetric flow, indicative of uniform atomization. The outer capillary through which the N_2 gas was injected was heated to 50°C to counteract the cooling due to evaporation and rapid expansion of the analyte. This increased the temperature of the gas at the nozzle and in the tubing downstream from -15°C to room temperature and prevented condensation of the analyte.

The range of operation of the nebulizer was determined as 10 ppm to 4000 ppm of o-xylene in N_2 by varying the flow rate and observing the onset of the formation of droplets at the output. The nebulizer was tested at different pump flow rates to determine the limit at which we do not observe complete nebulization of the solvent – apparent by the formation of droplets. Similarly, we varied the temperature of the nitrogen carrier gas to observe the

onset of condensation by observing the formation of droplets at the exit of the nebulizer.

Modeling of the gas flow was used to determine the effectiveness of the nebulizer performance within that operating range.

3.2.8 Data preprocessing

The sensing system measures the change in refractive index near the metal-dielectric interface by measuring the peak-shift of the extraordinary optical resonance due to the nanoholes. Fig. 3.8 shows the experimental obtained transmission spectrum with different refractive indices above the nanoholes. The resonance spectrum shows a broad resonance peak centered around 660 nm. This peak, as evident from Eq. 3.6, is due to the combination of resonances due to the gold-dielectric interface above the nanoholes, as well as the contribution of resonances between the Si_3N_4-Au interface.

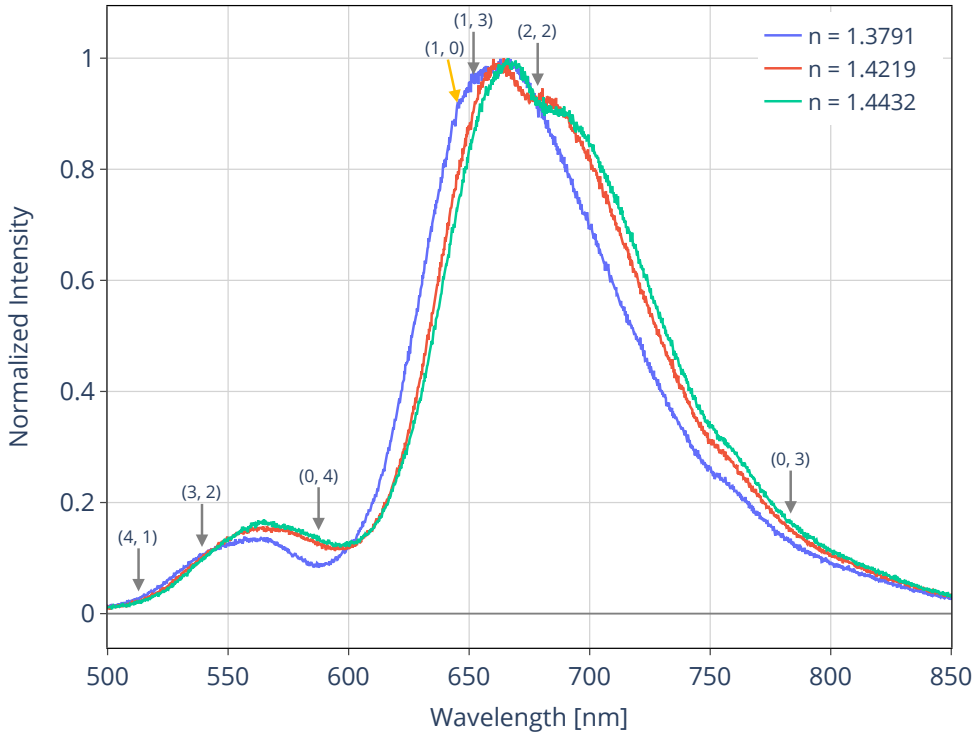

Figure 3.8: EOT resonance for different refractive indices. The location of the resonance, given by Eq. 3.6, are indicated by the gold and gray arrows with their respective orders

The peak shift due to changing refractive index can be obtained in a number of ways. The simplest approach would be to track the peak maximum of the resonance, however even in the best case, the broadness of the peak and inherent intensity noise of the spectrometer limits

the precision of peak-shift measurement of the system (Figure 3.9 (a)). More important in our particular case, the primary EOT peak originating from the gold-PDMS interface - which shifts in response to refractive index changes - appears only as a weak shoulder beneath a much stronger resonance, and thus has minimal influence on the overall peak position. Alternatively, the peak maximum can be retrieved by modeling the resonance shape and fitting the spectra with a least-squares fit. This method can increase the precision but would prove difficult to implement with his system due to complex peak shape as the transmission spectrum is combination of multiple different EOT resonance peaks and fails to handle changes to peak shape.

For our analysis, we opted to use the centroid of the resonance as it is able to effectively capture peak shift with higher precision as it measures the "center of mass" of the peak. To do this, the maximum of the spectrum was initially used to determine the full-width-at-half-maximum (FWHM) of the peak. Using this value, the centroid of the peak was calculated using all the wavelength within the FWHM of resonance using the equation:

$$x_{cen} = \frac{\sum x_i I_i}{\sum I_i} \tag{3.7}$$

where x_i are the wavelengths within the FWHM of the resonance, and I_i are their respective intensities. This method drastically improved the precision of the peak-shift measurement; however, it was found to contain multiple outliers as a result of the inconsistency in finding the peak maximum (to determine the FWMH of the resonance) due to the intensity noise of the spectrometer. To combat this, additional smoothing was performed prior to determining the maximum intensity to find the FWHM. This resulted in a more consistent and precise measurement of the peak shift. From Figure 3.9 (b), we can see evidence of this as the centroid calculation eliminated the outliers in the peak shift measurement and further increased the precision of the measurement. In this case, the uncertainty was calculated from the standard error (i.e. standard deviation in the mean) of the centroid calculation of 10 consecutively obtained spectra.

3.2.9 Data collection

The data collection for different runs was performed with a custom designed python application that plotted the observed spectrum and centroid shift in real-time to allow for the monitoring of any changes to the signal. The data was captured with an acquisition time of 10 s with gas bubbler setup, which was then reduced to 500 ms for nebulizer setup, owing to improvements in the data acquisition software. The centroid was determined from an

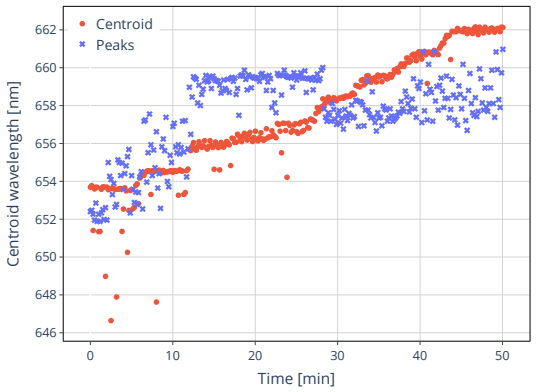

(a) Plot of the peak maximum (blue) and centroid position (red) for a calibration run.

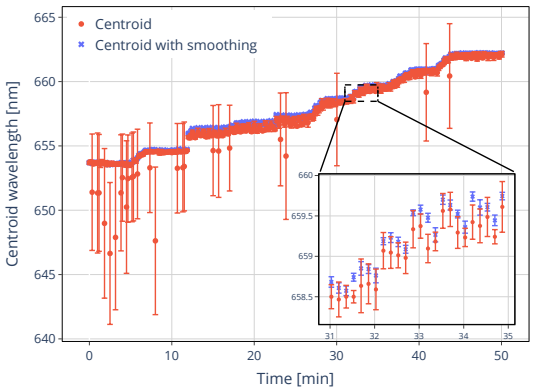

(b) Plot of the centroid postion with (blue) and without smoothing (red)

Figure 3.9: Comparison of data processing methods

average of 10 consecutively obtained spectra, unless stated otherwise.

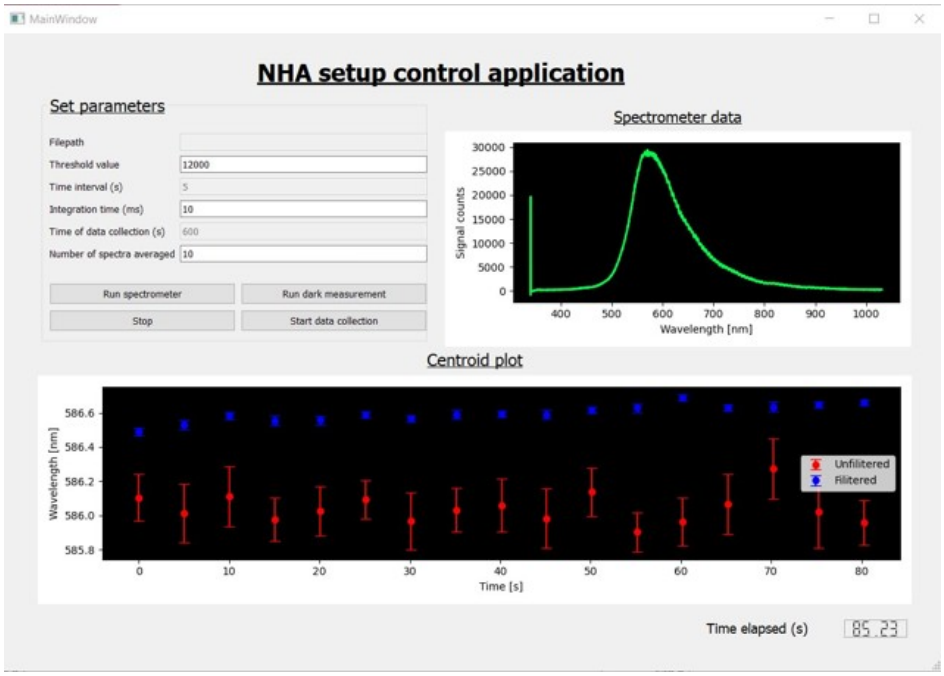

Figure 3.10: Python application for data collection

3.3 Theoretical models

3.3.1 Determining analyte concentrations in polymer films

The experimental mole fraction of o-xylene diffused in the PDMS can be determined from the refractive index change that was obtained experimentally using the centroid wavelength from the EOT spectrum and the calibration curve (Figure 3.13). The mole fraction was calculated using Eq. 3.8, an equation that had been derived previously [34],

$$\overline{X}(t) = \frac{P_{PDMS}\left[1 - \left(\frac{n_{PDMS}^2+2}{n_{PDMS}^2-1}\right)\left(\frac{n_{mix}^2(t)-1}{n_{mix}^2(t)+2}\right)\right]}{P_{PDMS}\left[1 - \left(\frac{n_{PDMS}^2+2}{n_{PDMS}^2-1}\right)\left(\frac{n_{mix}^2(t)-1}{n_{mix}^2(t)+2}\right)\left(1+\frac{\Delta d(t)}{d_0}\right)\right] - P_{Analyte}} \tag{3.8}$$

In deriving Eq. 3.8, it is assumed that the Lorentz-Lorenz equation holds, i.e. that molar polarizabilities, P_i, are linearly additive. Note that refractive indices, n_i, are not linearly additive. In this case, we also assume that swelling of the film is negligible ($\Delta d = 0$). Although it has been observed that PDMS swells by up to 50% after 72 hours of exposure to a saturated xylene atmosphere [62], the assumption holds in our experiments, since the sorption experiments were much shorter and at a lower xylene concentration. Indeed, the maximum swelling was estimated using thin-film interferometry to be between 2-5% and assumed negligible for the modeling (See Section 3.4.6).

3.3.2 Diffusion constants of the VOCs

Since the experiments are conducted at temperatures well above the PDMS glass transition temperature, T_g = -123°C [71], we can use the derived equations in the Chapter 2 to model the analyte migration of VOCs into PDMS.

The PDMS layer on the surface is thin compared to its lateral extension, and the hole diameter is orders of magnitude smaller than the film thickness. Therefore, the problem was analyzed as one-dimensional diffusion through a plane of finite thickness having an infinite reservoir of analyte gas above the polymeric sorption film. Most of this film is supported by the gold layer which is modeled to be an impermeable substrate (referred to as "supported film"), and a smaller fraction that is suspended above the nanoholes is modeled as a "free-standing film".

We mathematically described the sorption kinetics of a thin PDMS film supported by an array of nanoholes by integrating Crank's solutions for a one-dimensional diffusion problem. The derivation of these equations are presented in Chapter 2. The total analyte concentration is obtained from the linear combination of the time-dependent mathematical expressions,

describing an average mole fraction of the analyte over the range of the evanescent wave near metal-film interface through an permeable film on a impermeable supported substrate (SF), $\overline{X}_{SF}$, and a free-standing film (FSF), $\overline{X}_{FSF}$. For the case of absorption, this corresponds to Eq. 3.9 for $\overline{X}_{abs,SF}$ and Eq. 3.10 for $\overline{X}_{abs,FSF}$. The integrated equation for desorption for the film interface for the supported film and free-standing film are given by Eq. 3.11 and Eq. 3.12 respectively. For the free-standing film, we consider the case that we have a constant uniform concentration in the layer, as the supported film accounts for 80% of the total area. In these equations, the equilibrium mole fraction in the film, and the diffusion coefficient D are determined from the fit to Eq. 3.13 or 3.14.

$$\overline{X}_i(t)_{\text{abs, SF}} = a_j \left[1 - \left(\frac{8d}{\pi^2 \delta y}\right) \sum_{i=1}^{\infty} \frac{(-1)^i}{(2i+1)^2} \exp\left(-\frac{D_j\,(t-t_0)\,(2i+1)^2\pi^2}{4d^2}\right) \sin\left(\frac{(2i+1)\pi\delta y}{2d}\right)\right] ; \text{j} = 1, 2 \tag{3.9}$$

$$\overline{X}_j(t)_{\text{abs, FSF}} = a_j \left[\left(\frac{\delta y}{2d}\right) + \left(\frac{2d}{\delta y \pi^2}\right) \sum_{i=1}^{\infty} \frac{(-1)^i}{i^2} \left(1 - \cos\frac{i\pi\delta y}{d}\right) \exp\left(-\frac{D_j\,(t-t_0)\,i^2\pi^2}{d^2}\right)\right] \tag{3.10}$$

$$\overline{X}_j(t)_{\text{des, SF}} = b_j \left[\left(\frac{8d}{\pi^2 \delta y}\right) \sum_{i=1}^{\infty} \frac{(-1)^i}{(2i+1)^2} \exp\left(-\frac{D_j (2i+1)^2\pi^2\,(t-t_0)}{4d^2}\right) \sin\left(\frac{(2i+1)\pi\delta y}{2d}\right)\right] ; \text{j} = 1, 2 \tag{3.11}$$

$$\overline{X}_j(t)_{\text{des, FSF}} = b_j \left[\frac{4d}{\delta y \pi^2} \sum_{i=1}^{\infty} \frac{1}{(2i+1)^2} \left(1 - \cos\frac{(2i+1)\pi\delta y}{d}\right) \exp\left(-\frac{D_j (2i+1)^2\pi^2\,(t-t_0)}{d^2}\right)\right] \tag{3.12}$$

The film thickness, $d = 10.2\ \mu$m, was obtained using an optical profiler (see Fig. 3.5) and δy is the effective amplitude of the evanescent plasmonic wave into the PDMS and is obtained by modeling - see below and Fig. 3.12. The total sensing area is $2.0 \times 10^5 \mu\text{m}^2$, and the nanoholes, representing the FSF, account for $4.0 \times 10^4 \mu\text{m}^2$ or 20% of the total area. Therefore, the linear combination representing the total solvent mole fraction is:

$$\begin{aligned} \overline{X}_{\text{abs}} &= 0.8\overline{X}_{\text{abs, SF}} + 0.2\overline{X}_{\text{abs, FSF}} \\ \overline{X}_{\text{des}} &= 0.8\overline{X}_{\text{des, SF}} + 0.2\overline{X}_{\text{des, FSF}} \end{aligned} \tag{3.13}$$

The coefficients of this linear combination were further investigated using the FDTD simulation by considering the fraction of electric field intensity inside and outside the nanoholes.

As will be discussed below, most processes are best analyzed as concurrent sorption processes having two different diffusion rates given by D_1 and D_2, and Eq. 3.13 is therefore best written as

$$\begin{aligned}\overline{X}_{abs} &= 0.8\left[a_1\overline{X}_{abs,SF}\left(D_1\right)+a_2\overline{X}_{abs,SF}\left(D_2\right)\right]\\ &\quad+0.2\left[a_1\overline{X}_{abs,FSF}\left(D_1\right)+a_2\overline{X}_{abs,FSF}\left(D_2\right)\right]\\ \overline{X}_{des} &= 0.8\left[b_1\overline{X}_{des,SF}\left(D_1\right)+b_2\overline{X}_{des,SF}\left(D_2\right)\right]\\ &\quad+0.2\left[b_1\overline{X}_{des,FSF}\left(D_1\right)+b_2\overline{X}_{des,FSF}\left(D_2\right)\right]\end{aligned} \tag{3.14}$$

where a_1, a_2, b_1, b_2, D_1 and D_2 are the optimized parameters for the least-squares fitting algorithm.

3.3.3 FDTD simulation

To investigate the spatial extent of surface plasmon resonance (SPR) interactions within the system, δy, a three-dimensional finite-difference time-domain (FDTD) simulation was conducted using Tidy3D software package (Ver. 2.8.4, Flexcompute). Periodic boundary conditions were applied along the x and y directions (1.4 μm and 1.2 μm, respectively), corresponding to a small section of the hexagonal NHA. Along the z-axis, perfectly matched layers, PMLs, were implemented to absorb outgoing waves and prevent reflections. To ensure the highest resolution near the plane of interaction an override mesh was employed throughout the segment and with a height of 600 nm, centered about the TEM grid. The best override mesh size was found to be 7 nm in the x- and y-axes with 0.5 nm in the z-axis. The PDMS film, the Cr adhesion layer, and the silicon nitride substrate were modelled using the Sellmeier dispersion relation with parameters obtained from the Tidy3D database [72, 73, 74], while the optical response of gold was described using a Drude model, as it more accurately captures its plasmonic behaviour [75].

The FDTD simulation was used to determine the electric field spatial distribution across the gold surface and at various depths within the PDMS. This was used to estimate the sensing area ratio between the supported film over the gold surface versus the free-standing film over the holes and was found to be consistent with 4:1 ratio obtained from the fractional areas. This was achieved by applying a mask of the hexagonal pattern of the array on the spatial field distribution at different depths into the PDMS layer. From Figure 3.11, we can see that within the range of the plasmonic interaction ($\delta y = 25$ nm), the ratio of intensity outside versus inside the holes is equal to 4:1, consistent with the ratio of areas used for the modelling of diffusion coefficients in Eq. 3.13.

In addition, the integrated field intensity at the EOT resonance wavelengths was used to evaluate the decay of the SPP-induced fields into the PDMS material to estimate $\delta y = 25$ nm, the effective decay length of the evanescent plasmonic wave (Figure 3.12). This decay

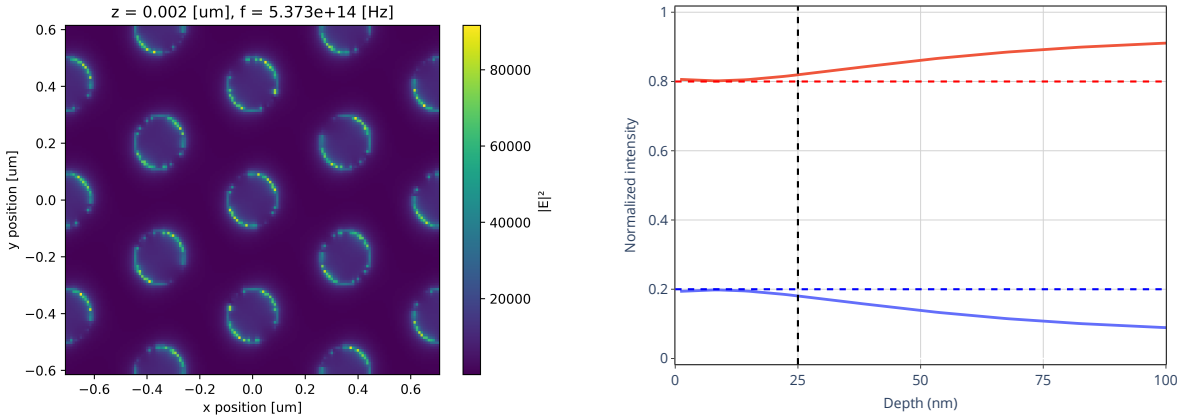

Figure 3.11: (left) Spatial electric field distribution over the nanohole at the Au-PDMS interface. (right) Plot of fraction of averaged intensities inside (solid blue) and outside (solid red) the holes of the NHA surface for different depths. The dashed red and blue lines represent the values used for modeling the diffusion kinetics as a linear combination of the two contributions. The dashed black line represents the penetration depth of the evanescent wave into the PDMS layer.

length, δy, governs the thickness of the layer in which the refractive index change can be measured, i.e. it corresponds to the bounds of the integrals that lead to Equations (3.9) to (3.12).

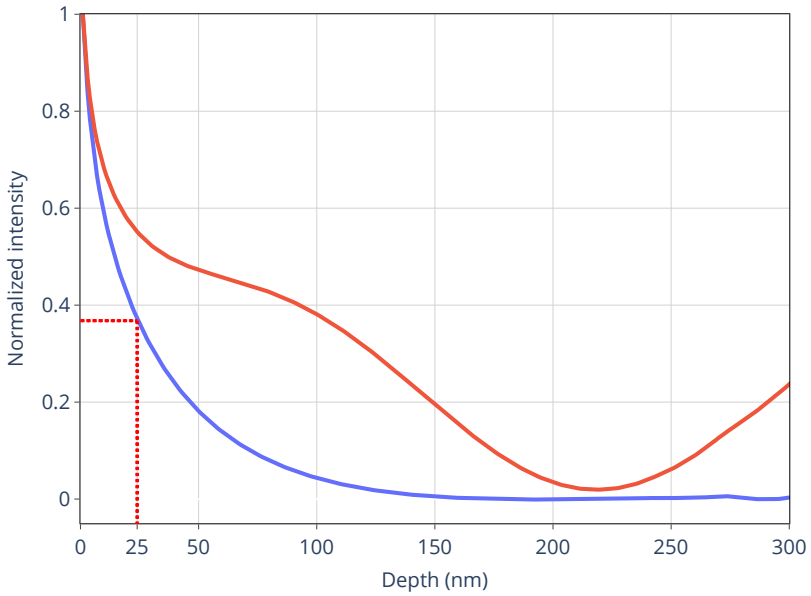

Figure 3.12: Calculation of the depth of the evanescent wave into the PDMS layer. The red curve shows the total average electric field intensity as a function of the depth, which includes the contribution from the reflected field. After subtracting the sinusoidal contribution from the reflected field, the exponential curve (blue) shows an evanescent intensity decay length of 25 nm.

3.4 Results

3.4.1 Sensor response curve

The diffusion mechanism of o-xylene through PDMS can be determined by measuring the time-dependent mole fractions of o-xylene in the PDMS layer adjacent to the gold-film. The mole fractions are obtained from the refractive indices during that process (Eq. 3.8). Over the small refractive index range that we study, the experimentally obtained wavelength shift of the EOT maximum (obtained using the centroid of the top 50% of the peak) correlates linearly with the change in the refractive index of the dielectric medium above the gold layer. A calibration series of mixtures, initially with dimethyl sulfoxide (DMSO, $n = 1.473$) and water ($n = 1.333$ at 589 nm) mixtures at Queen's University, then with glycerol ($C_3H_8O_3$, $n = 1.475$) and water mixtures at UVic, were measured to obtain the sensor's sensitivity (Fig. 3.13).

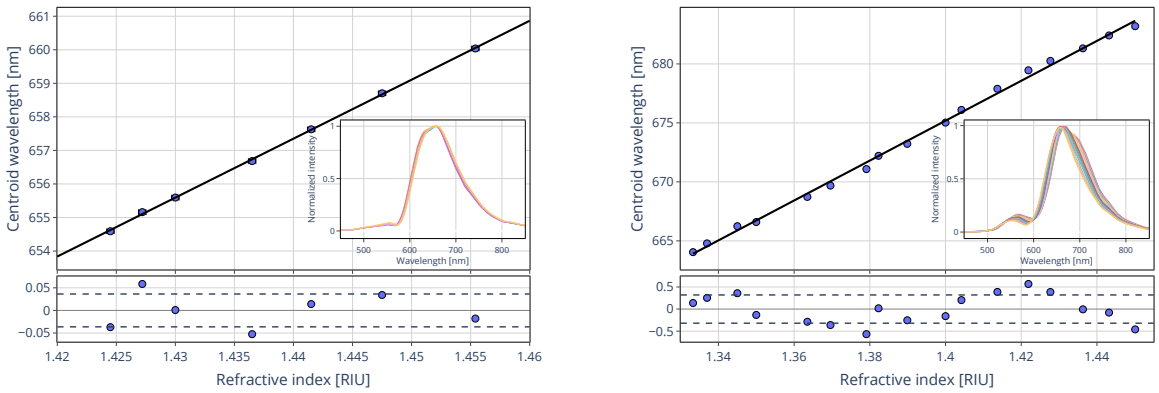

(a) DMSO and water mixtures

(b) Glycerol and water

Figure 3.13: Calibration of the sensor with two different solvents mixtures with water. The spectra of all the solutions are shown in the inset. The linear fit yields the sensitivity of the RI measurement as S = 175 ± 2 nm/RIU and S = 170 ± 3 nm/RIU. The horizontal width of the 1σ-confidence interval (0.08 nm and 0.8 nm) indicates that refractive index can be measured with an uncertainty of 0.0002 RIU and 0.002 RIU respectively.

This was achieved by placing a gold-coated nanohole array into a PDMS mould having a 50 μm open channel to allow for the flow of calibration solutions using a peristaltic pump. Each solution was directed over the NHA for a minimum of 60 s and the average centroid wavelength for each mixture was obtained.

The sensitivity obtained from both sets of calibration solutions were consistent, with a measured sensitivity of S = (175 ± 2) nm/RIU and S = (170 ± 3) nm/RIU for the DMSO

and glycerol mixtures, respectively. It should be noted that the measurement uncertainty of the refractive indices differ by a factor of 10 (0.0002 RIU for the DMSO-water mixtures, compared to 0.002 RIU for the glycerol-water mixtures). This is largely attributed to the precision and accuracy of the different devices used to experimentally measure the refractive indices, with the DMSO-water mixtures values obtained with an Abbe refractometer (ABBE-3L refractometer, Bausch & Lomb), while the glycerol-water mixtures refractive values were measured using a handheld digital refractometer (81150-56, Cole-Parmer).

3.4.2 Detection of o-xylene

Figure 3.14 (a) shows the response of the nanohole-array–based sensing system upon exposure to the volatile organic compound (VOC) o-xylene using the gas bubbler setup. The average centroid position of the extraordinary optical transmission (EOT) resonance is plotted as a function of time, with data acquired every 10 s. The analyte concentration can be determined by relating the sensor response to the refractive index change using Eq. 3.8.

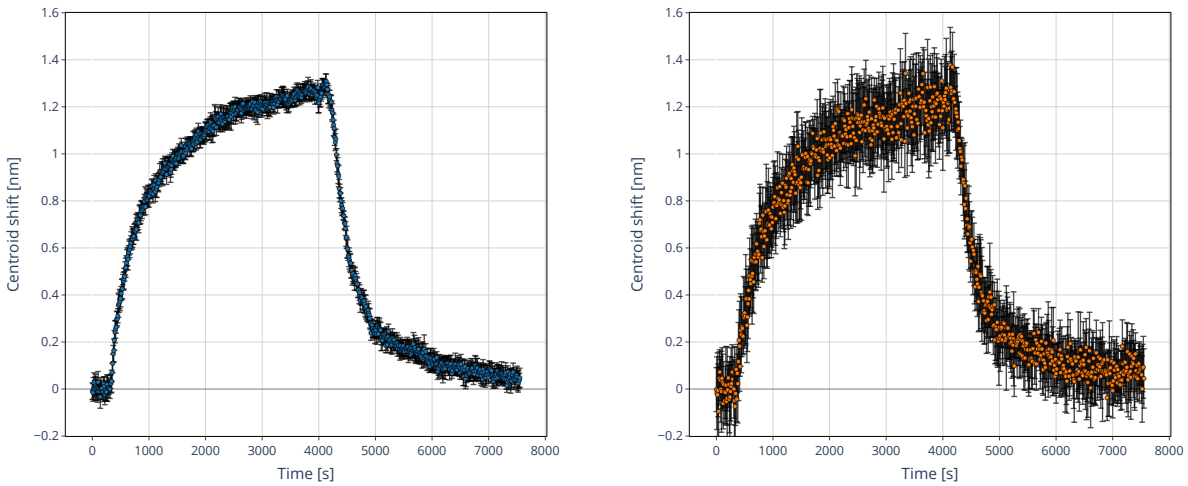

(a) With smoothing (b) Without smoothing

Figure 3.14: Centroid shift during the absorption and desorption of o-xylene. The two figures shows a comparison of the calculated centroid wavelength when we performed additional smoothing of EOT spectrum in order to determine the FWHM for Eq. 3.7

To establish a baseline, N_2 gas is initially flowed through the system prior to analyte introduction. During the absorption stage, the gas stream is directed through either the bubbler or nebulizer to load it with o-xylene, which is then delivered into the nanohole array chamber. Once equilibrium is reached, desorption is initiated by switching the chamber back to pure N_2 flow.

Following the baseline period, the centroid wavelength increases until reaching an asymptotic value, as o-xylene molecules diffuse into the thin PDMS layer and distribute uniformly throughout the film to the gold-PDMS interface, resulting in a measurable plasmonic response. The observed redshift during absorption arises from the higher refractive index of o-xylene ($n = 1.5058$) compared to PDMS ($n = 1.4425$).

The effect of data processing is highlighted in Figure 3.14, which compares centroid shifts obtained with (a) and without (b) smoothing of EOT spectrum curve in obtaining the centroid wavelength. The smoothed data processing method clearly exhibit reduced spread and significantly lower standard error, as evidenced by the error bars. This improvement yields a higher signal-to-noise ratio, thus enhancing the reliability of kinetic analysis of VOC diffusion into PDMS. The benefit of smoothing is particularly important for extracting meaningful physical parameters from the adsorption–desorption dynamics. Consequently, for the remainder of this chapter, all detection curves will be presented using smoothed centroids.

3.4.3 Effect of surface functionalization

Figure 3.15 presents multiple runs of o-xylene detection using the gas bubbler with two types of nanohole arrays (NHAs): one with bare gold (no surface functionalization) and another with gold surfaces functionalized with (3-mercaptopropyl)trimethoxysilane (MPTMS). The analyte concentration was extracted from the centroid shift and is plotted as a function of time, with data acquired every 10 s.

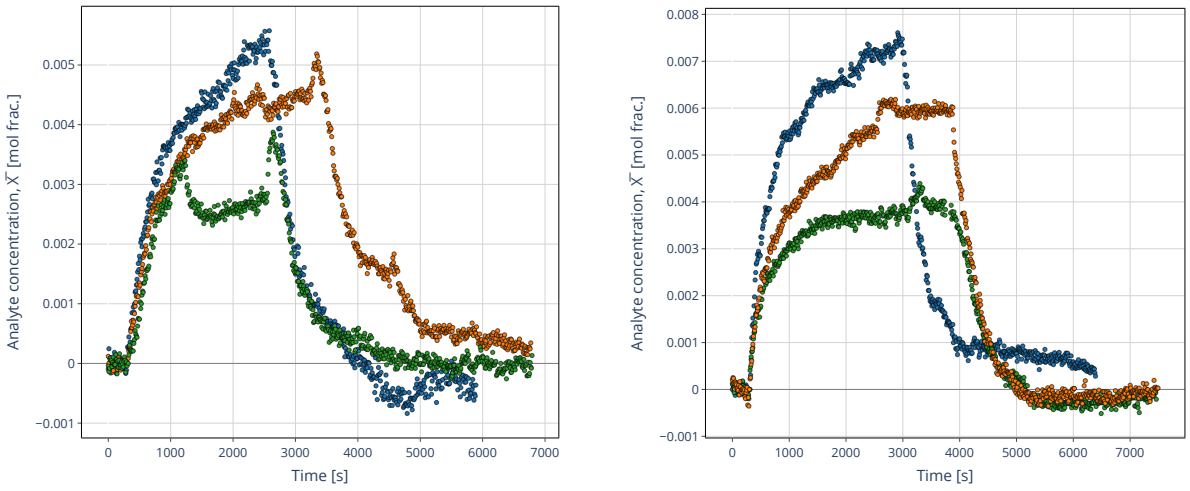

(a) Bare gold NHA

(b) MPTMS functionalized NHA

Figure 3.15: Sorption curves for o-xylene obtained with the gas bubbler system

For the control samples with bare gold, significant discontinuities are observed in the response curves, most notably during the absorption phase. These irregularities are likely caused by detachment or partial delamination of the PDMS from the gold surface, which strongly affects the local refractive index and introduces discontinuities into the measurement. This instability highlights a limitation of using unmodified gold surfaces for repeated measurements with PDMS.

By contrast, the MPTMS-functionalized samples demonstrate improved stability and reproducibility, as the chemical bonding between the thiol groups and the gold enhances adhesion at the PDMS–Au interface. This minimizes the likelihood of detachment and allows reliable reuse of a single sensing chamber across multiple runs.

Figure 3.15 also demonstrates the limitations of the gas bubbler setup. Despite maintaining similar experimental conditions for all runs, the loading of VOC into the carrier gas was not well defined, and as a result, the saturation levels of o-xylene varied between experiments, as reflected in the different asymptotic concentrations across datasets.

These results illustrate both the challenges and partial solutions in controlling analyte delivery using the bubbler system. While MPTMS functionalization improved the mechanical robustness of the sensor, the variability in analyte saturation underlines the need for more precise vapor delivery methods to achieve reproducible concentration profiles and enable accurate VOC detection for its use in kinetic modeling.

3.4.4 Nebulizer setup sorption curves

With the nebulizer setup, the VOC load in the carrier gas can be precisely controlled by adjusting the liquid flow rate through the thin capillary. From the flow rate, the corresponding concentration within the carrier gas can be determined; for example, a liquid injection of 1 μL/min corresponds to approximately 295 ppm or a partial pressure of 30 Pa.

Figure 3.16 presents representative datasets for flow rates of 3 μL/min and 8 μL/min. The use of the nebulizer clearly resulted in greater consistency between experimental runs at a given concentration. This improvement is attributed to the controlled analyte delivery and the constant nitrogen carrier gas flow of 750 mL/min. Notably, the results obtained at 8 μL/min further indicate that the diffusion of o-xylene within the polymer follows a two-step diffusion process. In order the investigate the effect of o-xylene absorption and desorption, the nebulizer setup was used to run multiple runs for flow rates between 2 μL/min to 10 μL/min with a minimum of 3 sorption runs captured for each flow rate. Figure 3.17 shows one of the detection curves for each of the different analyte flow rates, with vertical offsets

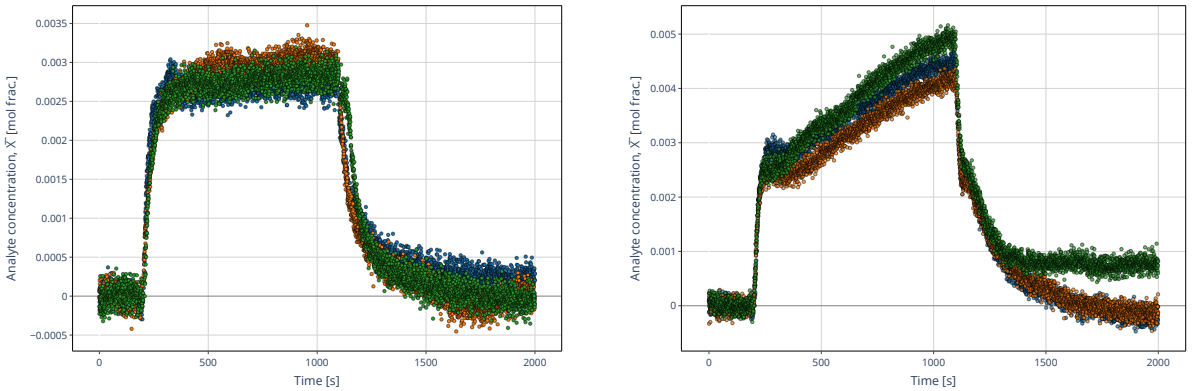

(a) 3 μL (b) 8 μL

Figure 3.16: Sorption curves for o-xylene with a flow rate of 3 μL/min and 8 μL/min through the nebulizer setup

applied for visualization.

By inspection, it is apparent that with increasing gas concentrations the rate of uptake of o-xylene into the film increases, and that the desorption rate also increases. In addition, the equilibrium value that is reached for each of the o-xylene partial pressures increases with increasing concentration, consistent with SPME principles [57]. It is also apparent that gas concentrations above 1770 ppm (179 Pa; 6 μL/min) show evidence for a second uptake process that occurs at a slower rate and leads to a much higher loading of the film. Especially the desorption curves show that the second slower process is time-delayed, as there is a clear step in the desorption curves.

The kinetics of this process will be quantitatively analyzed in the next section by fitting the experimental data to Crank's analytical solution of Fick's diffusion equation.

3.4.5 Determination of diffusion constants

In order to quantify the diffusion constants of the diffusion of o-xylene into PDMS, the absorption and desorption curves were fitted separately by a least-squares fit using the LMfit python package [76]. Briefly, the least squares fitting algorithm works by finding the set of parameters in a model that minimizes the sum of the squared differences (residuals) between the observed data and the model's predictions using the Levenburg-Marquardt gradient method. In other words, it adjusts the model parameters so that the curve fits the data as closely as possible, penalizing large deviations more strongly than small ones.

The absorption and desorption curves were fit with both a single diffusion coefficient and with two diffusion coefficients, i.e. using a weighted sum of the respective curves Equa-

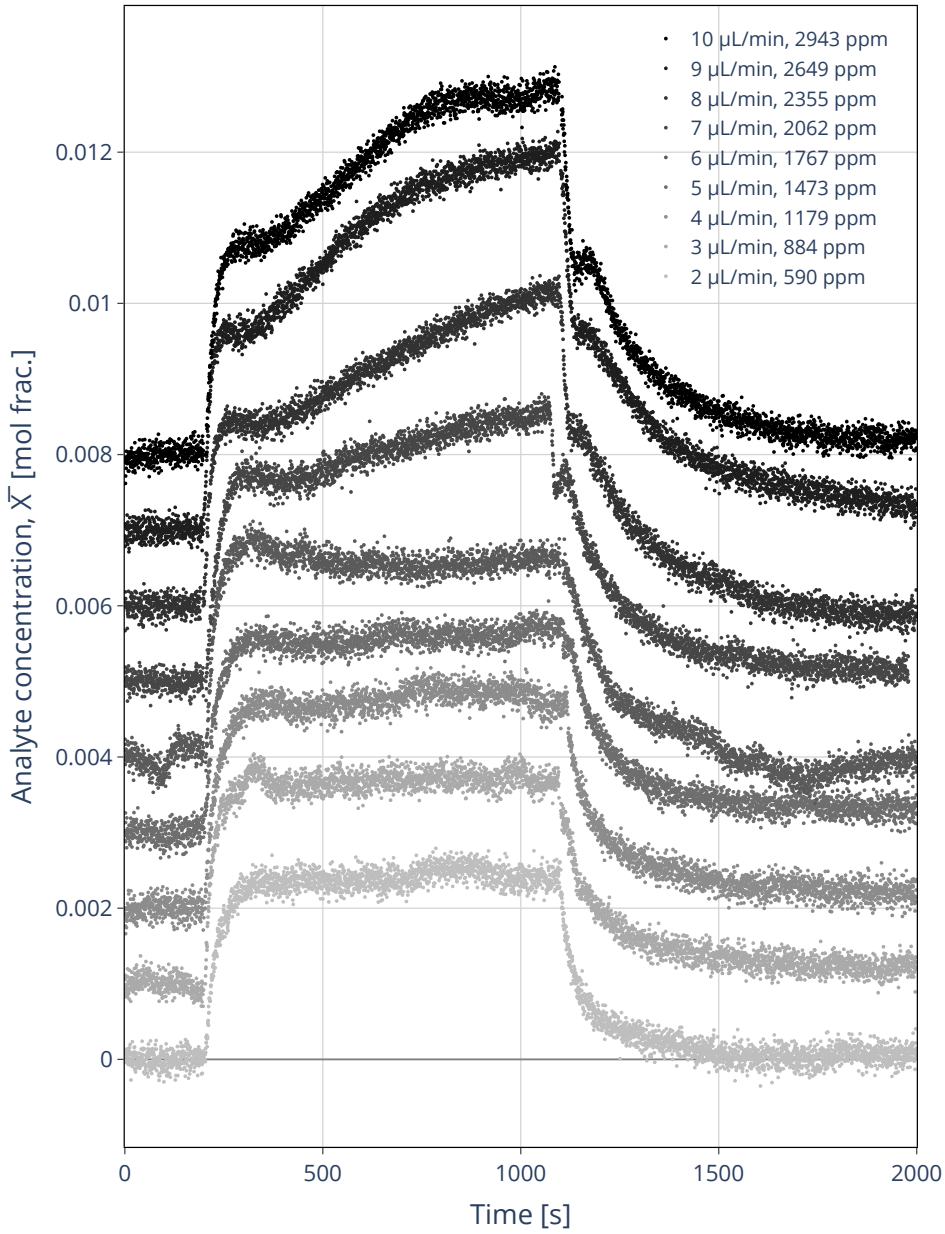

Figure 3.17: Sorption curves with nebulizer setup for different concentration of o-xylene. The absorption and desorption curves were obtained for a nitrogen gas flow of 750 mL/min. An additional offset is added for visualization. For the first 200 s, pure N_2 is flown over the chamber to establish a baseline, followed by 900 s of o-xylene saturated flow and pure N_2 flow again for absorption and desorption respectively.

tions (3.9) to (3.12) as expressed in Eq. 3.13 and Eq. 3.14, respectively. Table 3.2 summaries the initial guesses and bounds used for fitting parameters. The bounds ensured that the diffusion constants are physically meaningful and that the analyte concentration was

non-negative.

Table 3.2: Initial guess and bounds for double sorption constant fit parameters

Parameter	Initial guess	Lower bound	Upper bound
a_1/b_1	3.0×10^{-3}	0	N/a
a_2/b_2	1.0×10^{-3}	0	N/a
D_1	$1.0 \times 10^{-8}\text{cm}^2/\text{s}$	$1.0 \times 10^{-14}\text{cm}^2/\text{s}$	$1.0 \times 10^{-2}\text{cm}^2/\text{s}$
D_2	$2.0 \times 10^{-9}\text{cm}^2/\text{s}$	$1.0 \times 10^{-14}\text{cm}^2/\text{s}$	$1.0 \times 10^{-2}\text{cm}^2/\text{s}$

An additional baseline offset parameter was added to the equation to account for variation between sorption curves but was set to a constant through the fitting process. For absorption, the offset parameter was set to the value of first data point, and for desorption, the value was set to the average of the last 200 data points, i.e. when the desorption process has reached its asymptotic value.

In order to investigate if the diffusion processes are simultaneous or sequential, an additional delay time parameter, t_0, was introduced to allow for one of the sorption processes to start a certain time after the first process.

Figure 3.18 shows an example of the least-squares fit of the absorption and desorption using 2360 ppm o-xylene (238 Pa, 8 μL/min flow rate) to Eq. 3.14 having two different rates. Here, the fast and slow sorption processes were assumed to start at the same time and to occur concurrently. We note that the step in Figure 3.18, and, indeed, in all sorption curves with concentrations higher than 1770 ppm indicates that concurrent absorption may not be a good model. Introducing the time delay of the slower process as an additional fitting constant gave diffusion rates that were similar but had a larger variability, since the additional fitting parameter made the model less constrained (see Appendix B.1). For these practical reasons we retained the assumption that the slow and fast processes start at the same time in our analysis.

An analysis similar to that shown in Figure 3.18 was conducted for all concentrations of o-xylene and the two average diffusion coefficients for each flow rate were obtained by fitting. Each datum in Figure 3.19 represents the average fitted diffusion coefficients, D_1, D_2, of at least three runs, with the uncertainty derived from standard error. The size of the circular data markers is proportional to the asymptotic concentration, a_1, a_2, b_1, b_2, of the respective equation in Eq. 3.14.

The data tables below shows the absorption (Table 3.3) and desorption (Table 3.4) diffusion constants and asymptotic concentrations obtained by fitting the experimental data to Eq. 3.14.

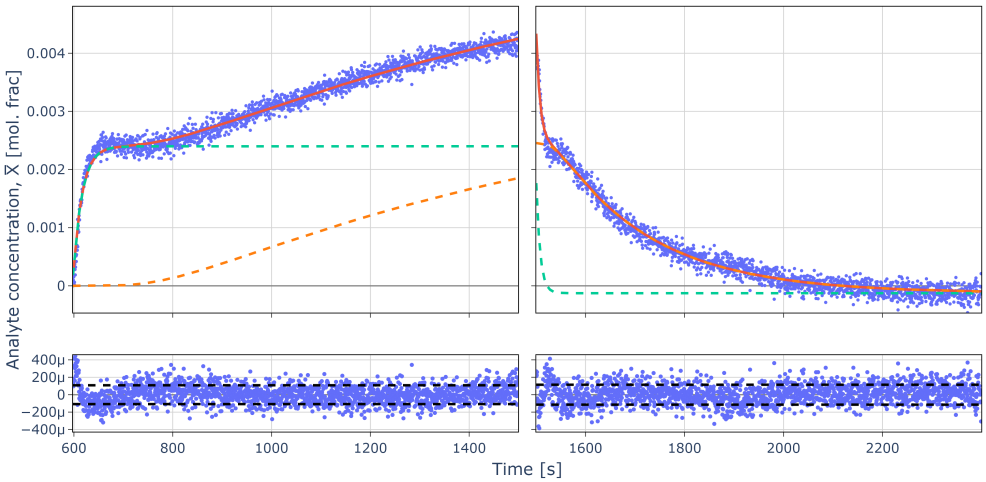

Figure 3.18: Fitting of sorption curve with Eq. 3.14. The fit (solid red line) is a linear combination of the bi-exponential fit (dashed green and orange line) for the absorption ($D_1 = 3.0\times10-8$ cm^2/s, $D_2 = 9.0\times10-10$ cm^2/s) and desorption ($D_1 = 3.5\times10-8$ cm^2/s, $D_2 = 1.9 \times 10 - 10$ cm^2/s). The residuals of each fit are displayed below each graph.

Table 3.3: Absorption diffusion constants and limiting asymptotic concentrations for each diffusion process

Flow rate [μL/min]	Conc. [ppm]	Diffusion constant, D_1 [cm^{2}s^{-1}]	Asymptotic concen., X_1 [mol. frac]	Diffusion constant, D_2 [cm^{2}s^{-1}]	Asymptotic concen., X_2 [mol. frac]
2	590	$(17 \pm 3) \times 10^{-9}$	1.5×10^{-3}	$(5 \pm 2) \times 10^{-9}$	1.4×10^{-3}
3	885	$(20 \pm 1) \times 10^{-9}$	3.1×10^{-3}	$(3 \pm 2) \times 10^{-9}$	0.5×10^{-3}
4	1180	$(18 \pm 2) \times 10^{-9}$	2.6×10^{-3}	$(6 \pm 3) \times 10^{-9}$	0.6×10^{-3}
5	1470	$(20 \pm 2) \times 10^{-9}$	3.1×10^{-3}	$(3 \pm 1) \times 10^{-9}$	0.9×10^{-3}
6	1770	$(20 \pm 2) \times 10^{-9}$	3.1×10^{-3}	$(0.4 \pm 0.2) \times 10^{-9}$	3.4×10^{-3}
7	2060	$(21 \pm 2) \times 10^{-9}$	3.2×10^{-3}	$(0.6 \pm 0.3) \times 10^{-9}$	3.4×10^{-3}
8	2360	$(24 \pm 0.4) \times 10^{-9}$	3.2×10^{-3}	$(0.5 \pm 0.1) \times 10^{-9}$	4.4×10^{-3}
9	2650	$(27 \pm 3) \times 10^{-9}$	3.7×10^{-3}	$(0.8 \pm 2) \times 10^{-9}$	4.6×10^{-3}
10	2940	$(24 \pm 4) \times 10^{-9}$	3.3×10^{-3}	$(0.9 \pm 0.2) \times 10^{-9}$	4.5×10^{-3}

The diffusion constants for the absorption processes are averaged to $D_1 = (22 \pm 6) \times 10^{-9}$ and $D_2 = (0.9 \pm 1.5) \times 10^{-9}$, whereas averaging the diffusion constants for the desorption processes yields $D_1 = (29 \pm 21) \times 10^{-9}$ and $D_2 = (2.5 \pm 0.7) \times 10^{-9}$. Here, the average was determined from the average of the diffusion constants weighted by their relative contribution to the process:

Table 3.4: Desorption diffusion constants and limiting asymptotic concentrations for each diffusion process

Flow rate [μL/min]	Conc. [ppm]	Diffusion constant, D_1 [cm^{2}s^{-1}]	Asymptotic concen., X_1 [mol. frac]	Diffusion constant, D_2 [cm^{2}s^{-1}]	Asymptotic concen., X_2 [mol. frac]
2	590	$(17 \pm 4) \times 10^{-9}$	1.8×10^{-3}	$(2.9 \pm 0.3) \times 10^{-9}$	0.8×10^{-3}
3	885	$(12 \pm 2) \times 10^{-9}$	2.2×10^{-3}	$(2.1 \pm 0.4) \times 10^{-9}$	0.9×10^{-3}
4	1180	$(9 \pm 1) \times 10^{-9}$	2.1×10^{-3}	$(1.7 \pm 0.2) \times 10^{-9}$	0.9×10^{-3}
5	1470	$(6 \pm 2) \times 10^{-9}$	1.6×10^{-3}	$(2.9 \pm 0.6) \times 10^{-9}$	1.2×10^{-3}
6	1770	$(7 \pm 2) \times 10^{-9}$	1.7×10^{-3}	$(2.3 \pm 0.5) \times 10^{-9}$	1.6×10^{-3}
7	2060	$(20 \pm 10) \times 10^{-9}$	2.2×10^{-3}	$(2.1 \pm 0.6) \times 10^{-9}$	1.6×10^{-3}
8	2360	$(58 \pm 3) \times 10^{-9}$	3.4×10^{-3}	$(2.9 \pm 0.7) \times 10^{-9}$	3.2×10^{-3}
9	2650	$(47 \pm 4) \times 10^{-9}$	3.7×10^{-3}	$(2.4 \pm 0.1) \times 10^{-9}$	3.3×10^{-3}
10	2940	$(41 \pm 4) \times 10^{-9}$	3.5×10^{-3}	$(2.3 \pm 0.1) \times 10^{-9}$	3.3×10^{-3}

$$\overline{D}_i = \frac{\sum_n X_{i,n} D_{i,n}}{\sum_n X_{i,n}} \tag{3.15}$$

The associated uncertainty

$$\sigma\left(\overline{D}_i\right) = \sqrt{S(\overline{D}_i)^2 + \Delta\overline{D}_i^2} \tag{3.16}$$

was determined from the respective weighted fit uncertainties of each of the measurement $\Delta D_{1,2}$, and from the standard deviation of the measured diffusion constants $S(D_{1,2})$

$$\Delta\overline{D}_i = \frac{\sum_n X_{i,n} \Delta D_{i,n}}{\sum_n X_{i,n}}; \quad S\left(\overline{D}_i\right) = \sqrt{\frac{\sum_n X_{i,n}\left(D_{i,n} - \overline{D}_i\right)^2}{\sum_n X_{i,n}}} \tag{3.17}$$

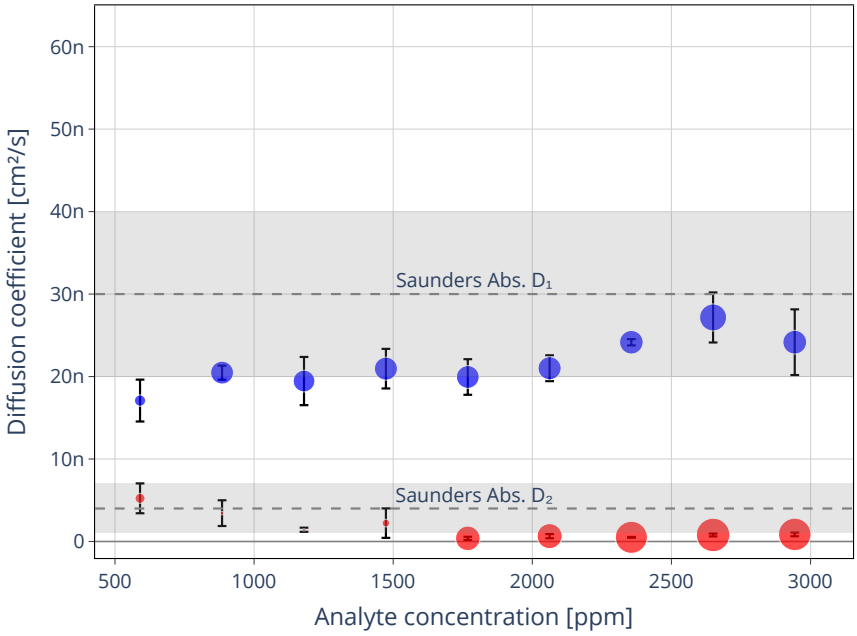

(a) Absorption

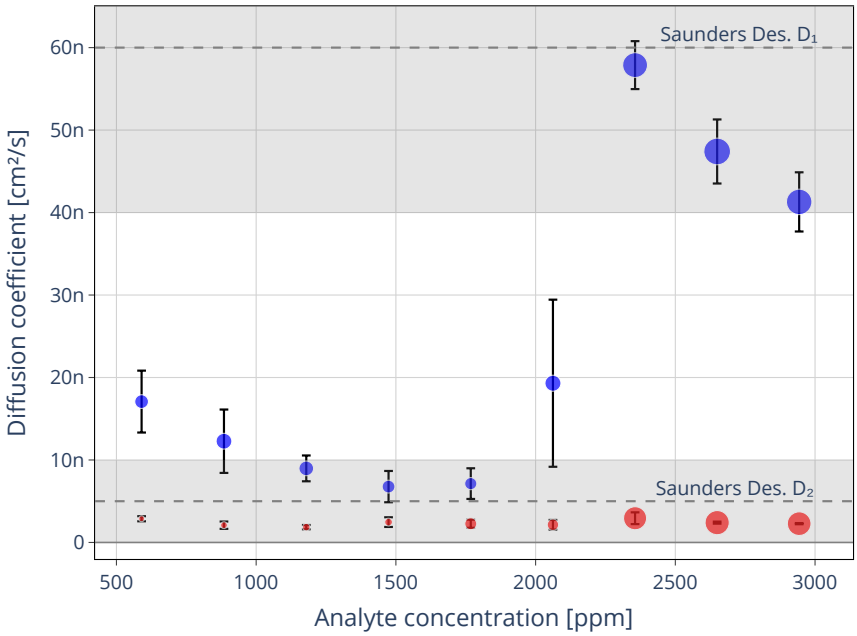

(b) Desorption

Figure 3.19: Average absorption (top) and desorption (bottom) diffusion constants (D_1 and D_2 given in cm^2/s) with the dashed grey line and shaded region representing previously obtained diffusion coefficients [34] for m-xylene with their uncertainties. The desorption D_1 diffusion coefficient for 2062 ppm (7 μL/min) shows a large uncertainty as not all fits were successful in capturing the second desorption process.

3.4.6 Estimation of swelling using thin-film interferometry

The EOT spectra obtained prior to analyte uptake and after the initial rapid shift of the EOT centroid were subtracted to obtain a differential spectrum. The difference spectrum contains the expected derivative line-shape near the EOT maximum but also amplifies the effect of thin film interference arising from Fresnel reflections at the PDMS interface (Figure 3.20). These small oscillations suggest that a low finesse cavity is formed due to the thin film of PDMS. Specifically, the oscillations in the difference spectrum arise from the swelling of this layer, thus altering the thickness of the cavity.

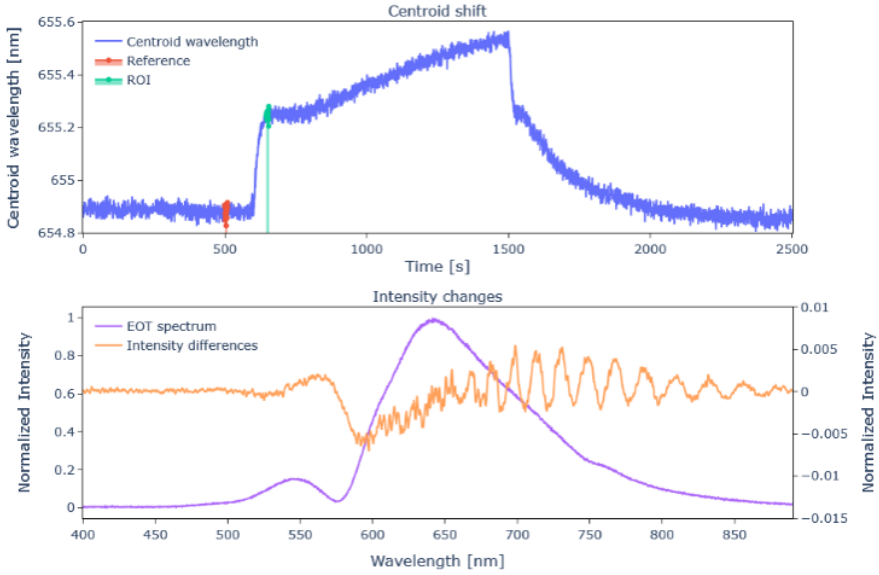

Figure 3.20: (top) Plot of the centroid shift for a full absorption and desorption run of o-xylene. (bottom) The normalized difference in intensity between the average intensity of the spectra in the ROI (highlighted in green) and a reference region (highlighted in red). The differential spectrum was obtained by taking the difference between the two regions of 10 s windows and smoothed using a Savitz-Golay filter with a window size of 11 and polynomial order of 3.

These oscillations can be modeled using a transfer-matrix approach [28] where we consider a three-layer system consisting of a PDMS film suspended in air. In this situation, we have the top layer and bottom with a refractive index of n_1, with a second layer of thickness d with refractive index of n_2. For light with incident angle of θ, we can derive the phase accumulated through the second layer using Snell's law:

$$\varphi = \frac{2\pi n_2 d}{\lambda} \cos\theta \tag{3.18}$$

If we consider normal incidence ($\theta = 0$), the total transmission through the film is obtained by summing the infinite series of multiple reflected beams and is given by:

$$t = \frac{4n_1 n_2 \exp(-j\varphi)}{(n_1 + n_2)^2 - (n_1 - n_2)^2 \exp(-j2\varphi)} \tag{3.19}$$

To simulate the effects of swelling with the Fabry-Perot cavity in the differential spectrum, we can adjust the thickness d in Eq. 3.18 and obtain the differential spectrum with respect to the initial spectrum at the start of the sorption runs when no swelling had occurred.

Figure 3.21 shows the comparison of the experiment differential spectrum with that predicted by Eq. 3.18 and 3.19. This figure qualitatively shows very good agreement assuming swelling of 3 % upon uptake of o-xylene. The model does not show the experimental variation below 660 nm as 3.19 ignores the plasmonic interaction due to the nanohole array and the resulting EOT peak shift. The small difference between the location of the calculated and experimental minima may be explained by our assumption of an ideal and perfectly flat PDMS surface (Figure 3.5).

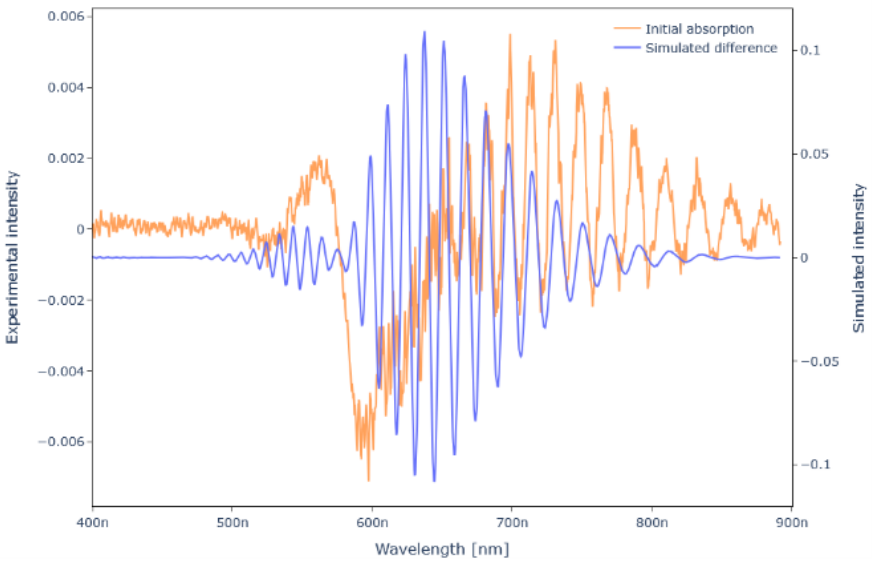

Figure 3.21: Differential spectrum after the first absorption stage (orange) and the modelled spectrum from Eq. 3.19 with a swelling of 3 %. The shape of the experimental curve below 650 nm is due to the peak shift of the EOT resonance.

3.5 Discussion

The residuals in Figure 3.18 may be used to estimate the uncertainty of the measurement. We can express this uncertainty either as the mole fraction of o-xylene in the film, $\delta X = \pm 0.0001$, or as the precision of the refractive index measurement $\delta n_{mix} = \pm 0.0001$ (see Eq. (3.8)). The precision of the refractive index measurement is much better than the accuracy obtained through the calibration curve in Figure 3.13, which also depends on the accuracy of the RI values determined for the calibration solutions (see Section 3.4.1.

Figure 3.19 shows that even at low concentrations of o-xylene the absorption and desorption curves can be well-fit using a process having two distinct diffusion constants. Both diffusion constants are consistent with earlier measurements of diffusion of m-xylene (not o-xylene) into a 20 μm-thick PDMS film interrogated by glancing angle thin-film interferometry [34]. The 1σ uncertainty of these previously obtained diffusion constants is given as grey bands in Figure 3.19.

The more robust measurements at concentrations $>$ 1770 ppm (6 μL/min) give diffusion constants that fall into the lower range of previously obtained values, which may be due to the difference between m-xylene used previously and o-xylene used here, the slightly different composition inherent with commercial PDMS formulations, or due to different boundary layer chemistry – our PDMS film is chemically bonded to a gold film, whereas in the previous measurement PDMS was spin-cast onto glass [34], a plexiglass plate [77] or a rubber membrane [67].

Importantly, the observed diffusion kinetics provide further evidence for a two-stage diffusion process as first reported by Saunders *et al.* [34] In their model, the VOC fills the pores within the PDMS resulting in a rapid change in refractive index. This process is followed by a slower absorption that changes the internal structure of the PDMS and causes it to swell. Both processes become faster with increasing VOC concentration of the surrounding gas, i.e. they are consistent with a first-order process.

The diffusion coefficients we obtained are consistent with measurements by Saunders *et al.* but they were 10-fold lower than those reported by other methods [67, 77, 40, 78] for o-xylene and its isomers. This discrepancy has been rationalized by Saunders *et al.* as being due to 1) the difference in PDMS manufacturers which has been shown to result in different degrees of crosslinking, thereby altering the diffusion kinetics through the polymer, and 2) the inconsistency of the mathematical modeling of the diffusion process through the PDMS, which can change the diffusion constant by a factor of 2 for different models as reported by Lue *et al.* [40, 64].

3.6 Summary

The results presented in this chapter demonstrate that plasmonic nanohole arrays (NHAs) coated with polydimethylsiloxane (PDMS) provide a sensitive and versatile system for detecting volatile organic compounds (VOCs), specifically o-xylene, and for investigating the diffusion kinetics of VOCs within polymer films.

The PDMS-coated NHAs exhibited clear and reproducible shifts in the extraordinary optical transmission (EOT) resonance upon exposure to o-xylene, confirming their capacity to detect refractive index changes associated with analyte uptake. The sensitivity of approximately 170–175 nm/RIU aligns well with reported values for other similar plasmonic sensing systems [17, 19], while offering advantages in terms of simplicity of fabrication and miniaturization compared to surface plasmon resonance or cavity-based optical methods. The use of centroid-based signal processing, combined with data smoothing, significantly improved measurement precision and reliability.

The experiments also revealed the critical role of adhesion between the PDMS layer and the underlying gold surface. Sensors without functionalization exhibited discontinuities in the response, likely due to detachment at the PDMS–gold interface. By contrast, functionalization with (3-mercaptopropyl)trimethoxysilane (MPTMS) substantially improved interfacial stability, yielding reproducible and reliable performance across multiple experimental runs.

The comparison of analyte delivery methods further emphasizes the importance of controlled experimental design. The bubbler system provided initial proof of concept but was limited by inconsistent and poorly controlled analyte concentrations, leading to variability in saturation levels and reduced comparability between experiments. Transitioning to a nebulizer system enabled fine-tuned control of analyte flow and concentration, resulting in greater reproducibility.

Together, these results establish PDMS-coated nanohole arrays as a promising platform for fundamental studies of polymer-VOC interactions. Beyond o-xylene, the method could be extended to other VOCs of environmental, industrial, and biomedical relevance, providing a versatile tool for monitoring air quality, assessing exposure risks, or probing polymer transport processes.

Despite these strengths, several limitations must be acknowledged. The assumption of negligible PDMS swelling, while justified for the timescales and concentrations used here, may not hold under longer exposure or higher VOC loading, and future work should explicitly quantify swelling effects. While the centroid method improved signal precision, it limits the

sensitivity of the device as we are implicitly averaging over both shifting and constant parts of the transmission spectrum. The complexity of overlapping EOT modes remains a challenge for rigorous modeling and may require more advanced spectral fitting techniques in future work.

In summary, the work presented in this chapter underscores the potential of plasmonic nanostructures integrated with functional polymer coatings to advance VOC sensing technologies and to open new avenues for studying molecular transport phenomena at the nanoscale.

Chapter 4

Long-range strain sensing system using a frequency-locked π-shifted grating

This chapter presents a passive, all-fiber strain sensing system capable of measuring localized strain with a 75 km fiber tether using a diode laser locked to a π-shifted grating. The bulk of the work described here has been published in a peer-reviewed article, for which I am the first author [1]. Section 4.4 detailing the coherent Pound–Drever–Hall detection setup is based on a second manuscript that has been submitted for publication, on which I am listed as the second author. The chapter is organized to first provide the theoretical background and experimental implementation of the sensing system, then present the characterization of the sensor using erbium-doped fiber amplification, followed by the description and initial results of the coherent detection system. It concludes with a discussion of overall performance metrics and the implications of this sensing approach for long-range applications in harsh environments.

4.1 Introduction

For the past six decades, the most common method to detect strain uses strain gauges consisting of metallic foil patterned on an insulated layer. The strain is obtained by measuring the change in electrical resistance of the gauge using a Wheatstone bridge as it is compressed and/or stretched. These sensors are prone to degradation due to corrosion, electromagnetic interference, and hysteresis.

The demand for sensing technologies that remain reliable and accurate under extreme environmental conditions has grown significantly across modern engineering and environmental monitoring fields. Among the most challenging of these applications is underwater sensing, where sensors must contend with high hydrostatic pressures, corrosive media, limited accessibility, and extended deployment distances [79]. Fiber optic sensors have emerged as a

promising solution for these applications, offering several advantages including immunity to electromagnetic interference, high sensitivity, and the ability to function over long distances with low maintenance requirements [2].

Long-range strain sensing using fiber optic components can be classified into two categories: highly localized or point-sensing, and distributed sensing. Point-sensing techniques use a single sensor head, most commonly a fiber Bragg grating (FBG) or its derivatives, that act as a transducer to measure the strain [80, 81]. These sensors offer high sensitivity [82, 83, 30] and are best suited for acoustic (microphone/hydrophone) [84, 85, 86] and acceleration measurements [87].

Distributed sensing methods utilize Rayleigh [88] or Brillouin backscattering [89] to detect and localize strain along the length of the fiber [90, 91, 92]. With Rayleigh backscattering (RBS) methods, the magnitude of the strain can be obtained either from the fluctuations in the intensity or the phase of the backscattered light due to changes in the interference state caused by the strain [91]. The localization of strain can be obtained from the time delay of the backscattered light, which can be determined either by sending a short pulse through the fiber using optical time domain reflectometry (OTDR) methods [93] or by mapping the delay to the frequency domain [94]. Brillouin scattering distributed sensors use similar measurement techniques to localize strain, but the magnitude of the strain is obtained by the Brillouin frequency shift or by the spectral linewidth [95]. Distributed fiber optic sensors have gathered significant interest in recent years for applications in submarine seismic sensing [96] due to their capacity to utilize existing telecom infrastructure and deliver high (meters) spatial resolution. However, the strain resolution of distributed sensors is limited to tens of microstrain in most systems [97, 98], with complex configurations [99] and phase demodulation schemes [100] required to achieve resolution at the nano-strain ($n\varepsilon$) level. In addition, optical signals need to be amplified in regular intervals so that the small scattering amplitudes can be discerned over distances of light travel [101].

In contrast, point-based sensors, particularly those based on fiber Bragg gratings (FBGs), offer passive, compact, and highly sensitive solutions for localized strain detection. These devices can achieve sub-microstrain resolution with simple architectures, and their inherently passive nature - requiring no on-site electronics - makes them ideal for long-range deployment in remote or harsh environments, such as subsea sensing, geophysical monitoring, or infrastructure assessment over distances exceeding tens of kilometers [80, 81, 102].

In this chapter, the long-range sensing refers to measuring sensing at a discrete highly localized point (less than 6 mm) with long fiber tethers to allow for remote deployment. This differs from long-gauge-length sensing which measures strain averaged over large distances

such as bridge.

The sensing principle of a fiber Bragg grating (FBG) relies on the modulation of the refractive index along the core of an optical fiber, which reflects a specific wavelength of light - known as the Bragg wavelength - while transmitting others. This reflection occurs due to constructive interference from the periodic index variation, and the Bragg wavelength is directly determined by the effective refractive index of the fiber core and the grating period. For a conventional FBG, this reflection envelope is typically between 0.2 nm to 0.5 nm. When the fiber is subjected to external perturbations such as strain, temperature, or pressure, these parameters change the grating period and/or the refractive index, leading to a measurable shift in the reflected wavelength. By precisely tracking this shift, FBGs can measure mechanical or thermal changes into optical signals with high accuracy and sensitivity [7].

Sensitive interrogation methods are required to resolve the narrow resonance shifts of π-shifted gratings. In the next section, I will be briefly summarize the most common interrogation methods for FBG-based strain sensors, and provide a description of the Pound-Drever-Hall locking technique used for our experimental setup.

4.1.1 Interrogation methods of FBG-based strain sensors

There are several different configurations that can be used to measure the strain on a FBG by either directly or indirectly measuring the shift in the Bragg wavelength. Although an optical spectrum analyzer can be used to measure the shift, these instruments are costly, slow and do not have the necessary resolution to measure shifts on the order of 10^{-12} m. Below I will briefly describe the most common methods.

FBG-based ring resonators utilize the change in reflectivity to indirectly measure the shift in the Bragg wavelength due to strain [103]. This is done by placing an FBG within a ring resonator and observing the transmitted intensities (Fig. 4.1). Outside the narrow-band reflection regime of the FBG, the system acts as a conventional ring resonator. The (ring) cavity resonance results in a forward-propagating mode of the input light only if the resonator is on resonance. If the wavelength of the incoming light also coincides with the Bragg wavelength the FBG reflectance produces a counter-propagating mode. The coupling between the two modes results in the splitting of the transmitted resonance into two spectral lines [104]. The strain can be obtained from the difference in wavelength between the split resonance lines, i.e., the coupling strength between the two coupled modes due to changes in the reflectivity of the FBG.

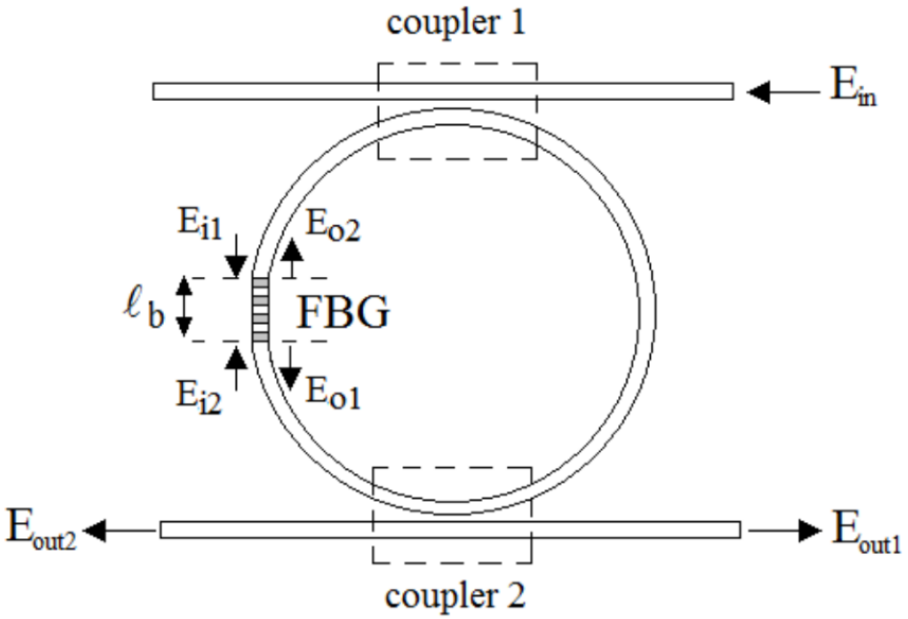

Figure 4.1: Schematic of FBG-based ring resonator strain sensing system. Figure from Reference [103]

Filtering techniques can be used to map the shift in wavelength due to strain to a change in intensity. In the simplest setup, a passive filter with linear attenuation near the Bragg wavelength will produce a change in intensity as the wavelength of the reflected light shifts due to strain on the FBG. This method is prone to fluctuations in the source intensity and requires the use of a reference measurement [29]. In recent years, additional improvements use a matched tunable filter, another FBG or FP cavity, thereby creating an "active filtering" system, which has shown increased sensitivity [26] (Fig. 4.2).

Since accurate intensity measurements are difficult, especially when light losses are difficult to quantify and/or to control, wavelength (or phase) measurements are usually preferred. The most straightforward phase measurements use a Mach Zehnder (MZ) interferometer, in which the phase difference between light in two co-propagating modes is used to measure the Bragg wavelength shift. In these configurations, the reflected envelope from the FBG could act as a source for an MZ interferometer (Fig. 4.2). Any shifts in the Bragg wavelength, λ_B, result in a phase difference, and subsequently a change in the output of the interferometer [26]. The interferometric phase can be demodulated through various methods using passive processing [105], homodyne processing [106], and in the Fourier domain [107].

Alternatively, the Pound-Drever-Hall (PDH) technique can be used to lock the laser to the resonance of an FBG. The PDH method is a frequency modulation technique that generates

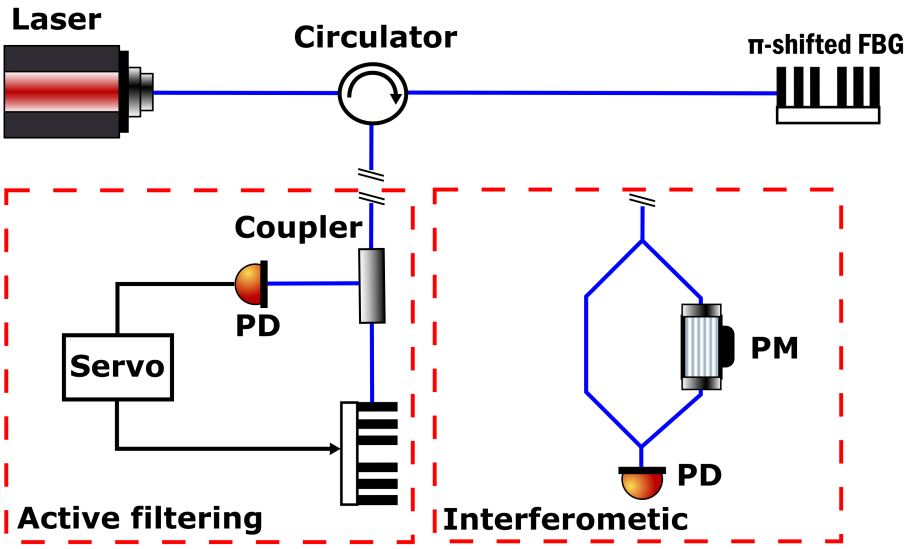

Figure 4.2: Schematic of active filtering and interferometric interrogation techniques

an error signal proportional to the degree of de-tuning from the cavity resonance. The strain is obtained from the feedback signal that is sent to the source to maintain the lock. This method thereby creates a signal that is directly correlated to the Bragg wavelength; it is used in the present work and will be discussed in detail in the following section.

4.1.2 Pound-Drever-Hall (PDH) frequency stabilization

The Pound-Drever-Hall technique was first devised in 1983 by R.V. Pound, R. Drever and J. L. Hall for laser frequency stabilization using a reference cavity [108]. It has since been integral in interferometric gravitational wave detectors [109], laser spectroscopy [110] and for many applications in atomic physics.

Previous attempts at laser stabilization with a cavity were performed by observing the changes in the reflected intensity near resonance. However, as the intensity profile is symmetric, it is not possible to lock at the center of the resonance of the cavity, and the system is susceptible to changes in the laser intensity itself [111]. To overcome this, the PDH method uses the derivative of the reflected intensity, which is antisymmetric, as the error signal to lock the laser. This is typically achieved by dithering the frequency of the incident light, either by phase or current modulation, to generate sidebands. The error signal is obtained by mixing the detected photodiode signal with the RF modulation and applying a low-pass filter (Fig. 4.3).

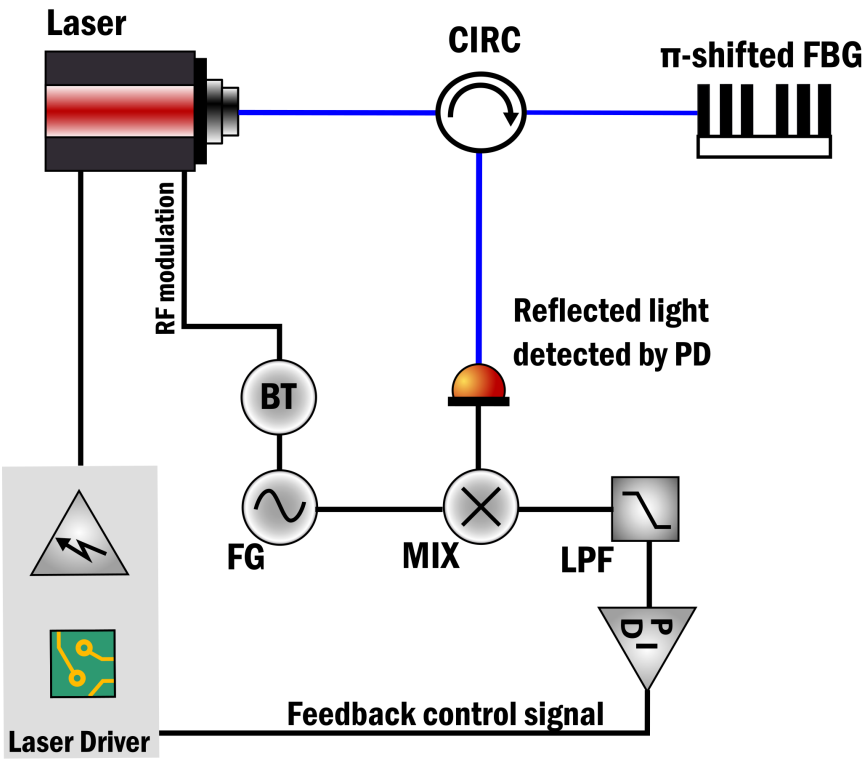

Figure 4.3: Basic PDH schematic with current modulation. CIRC: fiber circulator; BT: bias tee; PD: photodetector; FG: function generator; MIX: mixer; LPF: low-pass filter.

In the following, I describe the PDH technique following the arguments made by Black *et al.* [111], adapted by the author and Arthur Santos for the case for current modulation, in place of phase modulation. When using current modulation, we have both phase and amplitude modulation of the incident electric field (Fig. 4.4a):

$$\begin{aligned} E_{inc} &= E_0\,(1+\alpha\cos\Omega t)\,e^{i(\omega t+\beta\sin\Omega t)} \\ &\approx E_0\,(1+\alpha\cos\Omega t)\left[J_0 + J_1 e^{i(\omega+\Omega t)} - J_1 e^{i(\omega-\Omega t)}\right] \end{aligned} \tag{4.1}$$

where α is amplitude modulation depth, Ω is the RF modulation frequency, ω is the carrier frequency, β is phase modulation depth, J_0 and J_1 are the Bessel functions of the first kind.

The reflected electric field from the cavity is given by:

$$E_{\text{ref}} = E_0\left[F_\omega e^{i\omega t} + \frac{\alpha+\beta}{2}F_- e^{i(\omega+\Omega)t} + \frac{\alpha-\beta}{2}F_+ e^{i(\omega-\Omega)t}\right] \tag{4.2}$$

where $F(\omega)$ is the reflection coefficient function of the cavity. Here, I use a simplified

notation for the reflection coefficients where $F_\omega \equiv F(\omega)$ and $F_\pm \equiv F(\omega \pm \Omega)$.

The detected intensity by the photodetector is given by:

$$\begin{aligned} P_c = \left|E_0^2\right| \Bigg\{ & J_0^2 |F_\omega|^2 + J_1^2 \left(\frac{\alpha+\beta}{2}\right)^2 |F_+|^2 + J_1^2 \left(\frac{\alpha-\beta}{2}\right)^2 |F_-|^2 \\ & + J_0 J_1 \Re\left[F_\omega F_+^*(\beta+\alpha) - (\beta-\alpha)F_\omega^* F_-\right] \cos\Omega t \\ & + J_0 J_1 \Im\left[F_\omega F_+^*(\beta+\alpha) - (\beta-\alpha)F_\omega^* F_-\right] \sin\Omega t \Bigg\} \\ & + (2\Omega \text{ and higher order terms}) \end{aligned} \tag{4.3}$$

The terms oscillating at the modulation frequency, Ω, sample the phase of the reflected carrier and contain information on the derivative of the reflected intensity (highlighted in red in Fig. 4.4b). They can be extracted by mixing the photodiode output with the RF modulation and retrieving the DC component through a low pass filter.

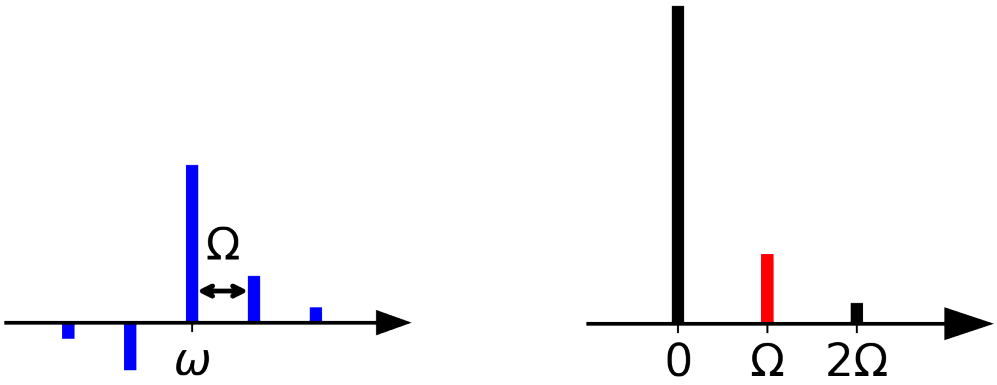

(a) From current-modulated laser (b) After photodiode detection

Figure 4.4: Frequency components of PDH technique. The blue line represent the light frequency component from the current-modulated laser, while the black lines represent the radio frequency components after detection by the photodiode. The red line shows the frequency component that is used to obtain the error signal

The error signal will be extracted from either the cosine term or sine term, depending on the modulation frequency and the cavity linewidth. For modulation frequencies much lower than the cavity linewidth (referred to as the "slow modulation regime"), the standing wave within the cavity has enough time to respond and will be in equilibrium with the incident beam. In this case, the term at the modulation frequency is purely real, and can just can be extracted from the cosine term. If you assume that $\frac{\Omega}{2\pi} \ll$ FWHM, the error signal is given by

$$g(\omega) \approx 2R_{PD}\beta P_0 J_0 J_1 \frac{d|F(\omega)|^2}{d\omega}\Omega \tag{4.4}$$

where R_{PD} is the responsivity of the photodetector.

For modulation frequency much larger than the cavity linewidth, the sidebands are totally reflected, and only the purely imaginary sine term remains. Conceptually, in this regime, the error signal is generated by the relative phase difference between the incident beam and the time-averaged phase over the storage time of the cavity [42]. For our setup, we operate at the slow modulation regime, thus the error signal is given by Eq. 4.4.

Recent advances in the Pound–Drever–Hall (PDH) interrogation technique have addressed key limitations in measurement range and probe power for high-resolution fiber grating sensors. To expand the dynamic range, the sideband interrogation method shifts the PDH response to frequency-shifted sidebands [112], eliminating the need for laser frequency tuning, while the high-order PDH technique exploits higher-order sidebands to generate multiple error signals [113], effectively broadening the usable range without sacrificing sensitivity. Liu *et al.* [114, 115] further proposed to use a heterodyne configuration with a Pound-Drever-Hall technique to greatly improve the SNR of the error signal when the probe power is low. This configuration divides the laser output into the probe beam and a local oscillator that is coherently detected with the reflected light to generate a beat signal. The PDH error signal can be retrieved by passing the beat signal through a band pass filter and frequency doubler. This signal will be similar to that obtained with the conventional PDH technique but the error signal is linearly proportional to the power in the LO arm, enabling the maintenance of high power and high signal-to-noise ratio (SNR) in the error signal, even at very low probe powers.

The Pound-Drever-Hall frequency stabilization method has been used previously with, both, fiber Fabry-Perot cavities consisting of two identical FBGs [82, 116, 117] and with π-shifted FBGs as strain sensors [31, 118, 119]. Gatti *et al.* demonstrated dynamic strain sensitivity down to $p\varepsilon$ level for frequencies above 100 kHz [31]. We previously attempted to add a tethered fiber (10 km) with such a system by locking a 1550 nm laser to a narrow (5-10 MHz) cavity resonance and found that the cavity resonances were susceptible to birefringent peak-splitting – an effect that cannot be avoided given the birefringent nature of a bent or strained fiber cavity [116]. It can also not easily be corrected when using longer tethers due to polarization wander [120], although a feedback-controlled polarization stabilization scheme has recently been demonstrated [121].

Previous attempts to utilize fiber Bragg gratings (FBGs) in localized long-range configu-

rations have been limited to distances of 25 km due to the transmission losses, necessitating the use of repeaters and optical amplification to extend their range [122, 123, 124, 125]. Additionally, the operating range of these systems is in the micro-strain regime (up to 1000 $\mu\varepsilon$) [124] and is, thus, ill-suited in applications demanding the detection of minute strains, such as hydrophones (50 $n\varepsilon$ to 1 $\mu\varepsilon$). In recent years, fiber laser strain sensors have been used to detect strain close to the thermodynamic resolution limit by detecting wavelength shifts in an optical pumped fiber laser using an unbalanced interferometer [126]. These sensors offer much higher resolution than passive FBG-based strain sensors. They may not be suited for long-range sensing, however, as they are based on phase-sensitive measurement of strain and require a very long coherence length [127].

4.1.3 Motivation and scope

In this chapter, we present a system for localized long-range (up to 75 km) strain measurements with a high bandwidth (up to 100 kHz), high sensitivity and large dynamic range ($<$ 30 $n\varepsilon$ to about 20 $\mu\varepsilon$). The system employs a π-shifted fiber Bragg grating (π-FBG) as the sensor head, coupled with an erbium-doped fiber amplifier (EDFA) placed in front of the photodetector to enhance the reflected signal. The π-FBG offers a broader resonance, reducing susceptibility to peak splitting, and the use of an EDFA to boost the low return light signal is more advantageous than amplifying the low electrical signal of a photodetector. The strain is measured using the Pound-Drever-Hall (PDH) method to lock the laser to the resonance and is encoded in the feedback signal required to maintain the lock.

Furthermore, we demonstrate an improved coherent PDH setup to improve the signal-to-noise ratio of the error signal to allow the system to lock to a laser with a very weak return signal (-58 dBm; $<$ 2 nW). This eliminates the need for an EDFA and is expected to allow the system to measure strain with a fiber tether up to 155 km.

Our findings demonstrate the potential of this advanced strain sensing system to address the challenges of long-range, high-sensitivity measurements in harsh environments, paving the way for more robust and reliable underwater sensing applications.

4.2 Experimental methods

The PDH method uses the derivative of the reflected intensity as the error signal to lock the laser wavelength to a resonance of an optical cavity. This is typically achieved by dithering the frequency of the incident light, either by phase or current modulation, to generate sidebands. The error signal is obtained by mixing the detected photodiode signal

with the RF modulation and applying a low-pass filter. It is antisymmetric around the cavity resonance and can therefore be used to provide negative feedback to the laser.

The demodulation of the photodiode signal to obtain the error signal was initially performed with an all-analogue setup with a custom-built circuit with an on-board mixer, and adjustable PI servo loop to send feedback to the laser (Fig. 4.3). The acquiring of the feedback signal and locking of the laser were performed through a custom Python script through a Raspberry PI [120]. This system was able to lock the laser to the resonance of the π-shifted and obtain strain measurements over a fiber tether of 50 km, but the system had a limited frequency bandwidth, < 100 Hz with 50 km of fiber, thus was not suited for acoustic measurements required for applications such as building a fiber optic hydrophone. In order to improve the frequency response and increase the range of fiber optic strain sensor, the demodulation of the photodiode signal and locking was done with an FPGA-device (Moku:Lab, Liquid Instruments, USA), and improvements were made to the photodiode amplifier to reduce the detector noise in the system. In order to further improve the measurement range of the strain sensor, a coherent PDH setup was employed whereby the weak return signal is heterodyned with a frequency-shifted local oscillator arm to improve the signal-to-noise ratio of the error signal.

I will first provide a description of the experimental setup with the use of EDFA to amplify the reflected light and provide the full sensor characterization of the setup. Next, I provide the description of the coherent Pound-Drever-Hall system, and initial results from these strain measurements having an improved signal-to-noise ratio.

4.2.1 Experimental setup

In this work, a tunable DFB laser (Avanex A1905LMI) is radio frequency (RF)-modulated at 11 MHz through a bias tee to produce the necessary side bands for locking (Fig. 4.5). The modulated light is directed towards a π-shifted FBG mounted on a piezoelectric ceramic cylinder (APC International Ltd, No. 42-1052) through a fiber circulator and single-mode fiber tethers having lengths of approximately 3 m, 25 km, 50 km and 75 km. The reflected light from the grating is amplified using an EDFA (Keopsys/Optocom Innovation) and detected with a fast photodetector (Lucent 131N) through a low-noise photodiode circuit (see Appendix C.1.1 for circuit design). The detected signal is processed by an FPGA hardware device (Liquid Instruments, Moku:Lab) to obtain an error signal and to lock the laser to the cavity resonance. This is achieved by mixing the photodiode signal with the RF-modulation and applying a low-pass filter (4th-order Butterworth filter $f_{co} = 70$ kHz). The error signal

is sent through a proportional-integral (PI) controller towards the laser driver to maintain the lock. The feedback control signal is also sent to a lock-in amplifier (Stanford Research Systems, SRS 830) to accurately measure the amplitude of the feedback signal.

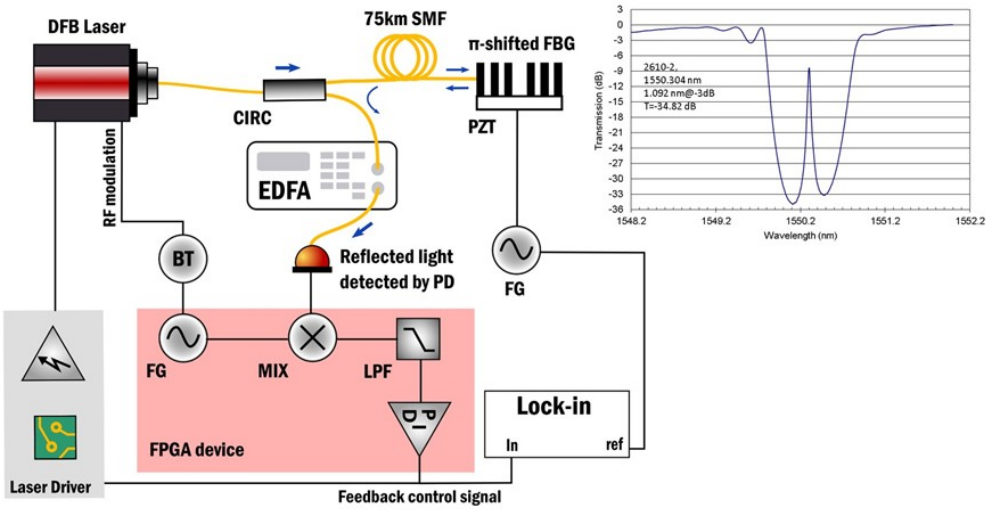

Figure 4.5: Strain sensing setup. CIRC: fiber circulator; BT: bias tee; PD: photodetector; FG: function generator; MIX: mixer; LPF: low-pass filter; FPGA: field programmable gate array PZT: 38.1 mm diameter piezoelectric ceramic cylinder. Inset: Transmission spectrum of π-shifted FBG obtained with an Optical Spectrum Analyzer having a bandwidth of about 15 pm.

The π-shifted grating is a 6 mm FBG produced at Toronto Metropolitan University with a missing "tooth" that results in a sharp cavity resonance with bandwidth of 6 pm (750 MHz) at 1550.304 nm (Fig. 4.5 inset). This grating is attached to a piezoelectric transducer. Strain is applied on the sensor through radial expansion of the PZT cylinder using a function generator and a piezo driver (PiezoDrive, MX200). Both the frequency and amplitude of the expansion are controlled independently. The static strain applied on the sensor, ε, was approximated using the expression of the radial displacement given by the piezoelectric constant, d_{31}:

$$\varepsilon = d_{31}\left(\frac{t+ID}{2t}\right)\frac{V}{r} \tag{4.5}$$

where t, r, ID and are the thickness, radius, inner diameter of the cylinder, and V is the voltage supplied. The above equation can be used to estimate the dynamic strain amplitude on the sensor for frequencies far from any mechanical resonances.

4.2.2 Error signal and PDH locking

Fig. 4.6 shows the obtained PDH error signal and their respective signal-to-noise ratio (SNR) for the system with different tether lengths. The signal-to-noise ratio (SNR) of the error signal was measured to determine the maximum tether length possible with the setup. The error signal was obtained by scanning the laser frequency through the laser current at 10 Hz. The SNR was measured as the ratio of the peak-to-peak amplitude of the error signal divided by the standard deviation of the dataset. Here, the peak-to-peak amplitude was determined by applying a 10 kHz low-pass filter to eliminate the high frequency contributions to the signal. The maximum tether length was limited to 75 km due to the low SNR of the error signal (< 5) with longer tethers.

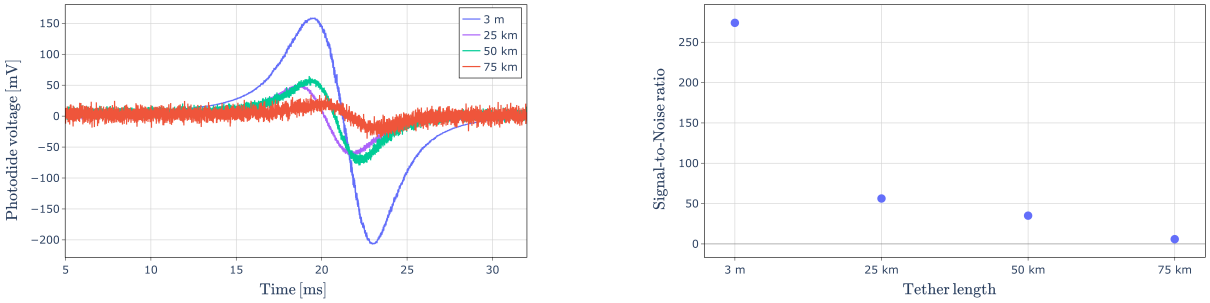

(a) PDH error signal for each tether length

(b) Signal-to-noise ratio for each tether length

Figure 4.6: PDH error signal and signal-to-noise ratio

To perform the PDH locking, a variation of the Ziegler-Nichols tuning was used to determine the optimal proportional and integral gain for the PI controller. Aside from the inevitable roll-off introduced by the bandwidth of the feedback loop, an additional phase delay is introduced for the longer tether lengths due to the light round-trip travel time (253 μs, 507 μs, and 761 μs, for 25 km, 50 km, and 75 km respectively). To satisfy the Nyquist criterion for stability in closed-loop systems, the gain for higher frequencies was therefore reduced as the length of the fiber was increased. Due to the lower gain at higher frequencies, we have a less "tight" lock which results in a marked amplitude response of the photodiode signal in response to the applied strain. Note, that the photodiode registers a minimal amount of light intensity when the laser is tightly locked to the resonance, i.e. at the peak of the π-FBG resonance. As long as the laser remains locked at these high acoustic modulation frequencies, the photodiode signal can then be used to recover the high-frequency information.

The robustness of the FPGA-based locking algorithm allows for the system to remain locked near the π-shifted FBG resonance even when strain is applied at frequencies above the servo bandwidth (500 Hz – 20 kHz depending on the tether length). This allows us to detect strain directly from the photodiode signal at acoustic frequencies higher than the cut-off frequency. A similar technique was utilized previously to develop a fiber optic vibration sensor with an ultrawide frequency range (from subsonic frequencies up to 10 MHz) [116]. It should be noted that it is difficult to recover the *absolute* magnitude of the strain from changes in the photodiode signal intensity. Since the reflected intensity is proportional to the FBGs reflectivity in the non-linear region of the FBG reflection spectrum, the photodiode signal always contains higher harmonic frequencies.

Furthermore, the use of current modulation to control the laser wavelength results in amplitude modulation of the light output at the RF modulation frequency, in addition to the desired frequency modulation. This provides unequal powers in the sidebands and leads to a lock that is centered slightly off-resonance.

4.3 Sensor characterization

The performance of a strain sensing system is characterized by four main metrics: resolution (or limit of detection), sensitivity, dynamic range, and its frequency bandwidth. These metrics are quantified for the current system through amplitude and frequency modulation of the PZT cylinder. Our measurements are also supported by a sound (music) recording with both the feedback and photodiode signals. Of the two sound recordings, the recording using the photodiode output has a lower signal-to-noise ratio compared to the recording using the feedback signal.

4.3.1 Strain response

The theoretical strain dependence of the π-FBG's resonant wavelength λ_B can be modeled by differentiating Eq. 1.1 with respect to the length of the grating, L:

$$\frac{\partial \lambda_B}{\partial L} = 2\left(\frac{\partial n_{\text{eff}}}{\partial L}\Lambda + n\frac{\Lambda}{L}\right) \tag{4.6}$$

Multiplying by L and substituting $\varepsilon = \partial L/L$ yields Eq. 4.7, i.e., the strain sensitivity of the wavelength measurement, where $\partial n_{\text{eff}}/\partial \varepsilon$ is the strain dependence of the refractive index.

$$\frac{\partial \lambda_B}{\partial \varepsilon} = 2n_{\text{eff}}\Lambda \left(\frac{1}{n_{\text{eff}}} \frac{\partial n_{\text{eff}}}{\partial \varepsilon} + 1 \right) \tag{4.7}$$

This equation can be expressed in terms of the properties of fiber:

$$\frac{\partial \lambda_B}{\partial \varepsilon} = 2n_{eff}\Lambda \left(1 - \frac{n_{eff}^2}{2} \left[p_{12} - v \left(p_{11} + p_{12} \right) \right] \right) \tag{4.8}$$

where p_{ij} are Pockel's coefficient of the stress-optic tensor and v is Poisson's ratio of the fiber-optic material. This strain dependence is valid for a FBG and a π-shifted FBG as both their resonances are centered at the Bragg wavelengths. Using the strain-optic coefficients for SMF-28 fiber ($p_{11} = 0.116$ and $p_{12} = 0.255$ at 1531 nm [128]), Poisson's ratio, $v = 0.17$ [129], and the tuning characteristics of our laser (2.924 pm/mV), we can calculate the expected system sensitivity to be 4.22 mV/$\mu\varepsilon$.

Although the Bragg wavelength of an FBG is also temperature-dependent, this effect can be neglected in our setup as we monitor dynamic strain signals occurring at much higher frequencies than typical thermal fluctuations. Temperature changes in the fiber occur over much longer timescales (seconds to minutes) and therefore remain effectively constant within the dynamic measurement window, contributing negligibly to the strain-induced wavelength shifts.

Fig. 4.7 shows the feedback signal output of the system in a frequency-locked state under different amplitudes of applied strain at 10 Hz with the 75 km fiber tether. The power spectral density of the unstrained output and strained output indicates the presence of line noise with peaks at 60 Hz, 180 Hz, 240 Hz and 300 Hz. The strained output has further peaks at the harmonics of the applied strain frequency.

Fig. 4.8 shows the strain response of the system for different tether lengths at a PZT modulation frequency of 10 Hz. The voltage amplitude of the feedback control signal was measured with a 1-second time constant on the lock-in amplifier (Stanford Research Systems, SR830) to suppress frequency noise. The system sensitivity was measured to be 5.27 mV/$\mu\varepsilon$ for a tether length of 75 km, with nearly identical values for 50 km, and 25 km and 3 m tethers in fair agreement with the calculated value of 4.22 mV/$\mu\varepsilon$.

The minimal detectable strain derived from the 3σ confidence intervals of this linear fit was determined to be 22-24 $n\varepsilon$ for all tether lengths [130].

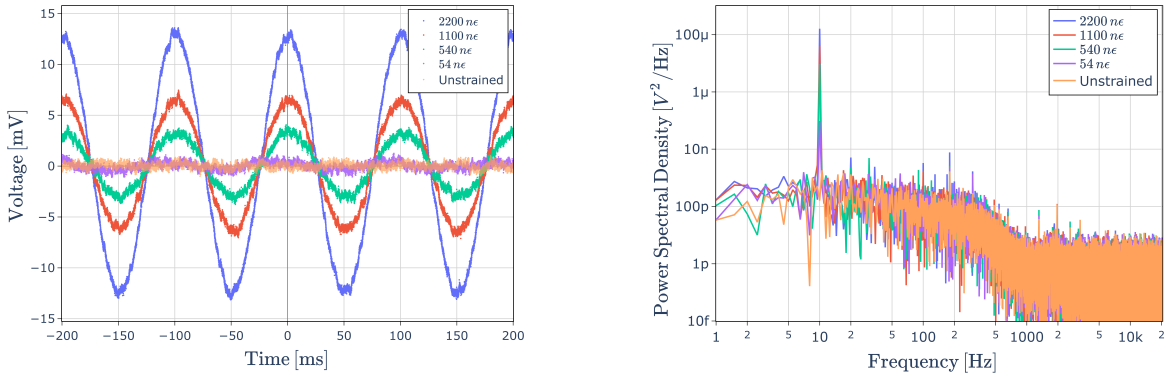

(a) Feedback signal output

(b) Power spectral density

Figure 4.7: Feedback signal output and its power spectral density for applied strains of 2200 $n\varepsilon$ (blue), 1100 $n\varepsilon$ (red), 540 $n\varepsilon$ (green), 54 $n\varepsilon$ (purple) at 10 Hz, and the frequency-locked output of the unstrained fiber (orange). The raw data was captured with a sampling rate of 50 kHz.

4.3.2 Frequency response

The frequency response of the system was investigated by applying a constant amplitude sinusoid over the acoustic frequency range to the PZT cylinder. The amplitudes of feedback voltage and photodiode voltage were recorded using a frequency response analyzer (Liquid instruments, Moku:Go) and are shown in Fig. 4.9.

The frequency response can be split into three regimes: (1) At low frequencies, we observe maximum gain from the servo-amplifier which provides the highest sensitivity for measuring strain through the feedback signal. The cut-off frequency for this regime (indicated by vertical dashed lines) is dependent on the tether length and the time-of-flight of the photons. We lowered the gain above the cut-off frequency to ensure the closed-loop stability of the system. (2) Above the time-of-flight cut-off frequency, the feedback signal exhibits a lower sensitivity, but the strain on the fiber can nevertheless be determined. In this regime, there is a phase delay in the feedback signal that can be modeled based on the length of the tether (not shown). Furthermore, in this regime, the less tight lock (due to lower gain) allows for the measurement of the applied strain from the photodiode signal. (3) For frequencies higher than the low-pass filter cut-off, and with high strain amplitudes, (at 25 kHz in Fig. 4.9), the feedback signal is no longer proportional to the applied strain, but the laser remains locked to the resonance of the cavity.

Fig. 4.10 shows the correlation between the feedback and photodiode signal for frequen-

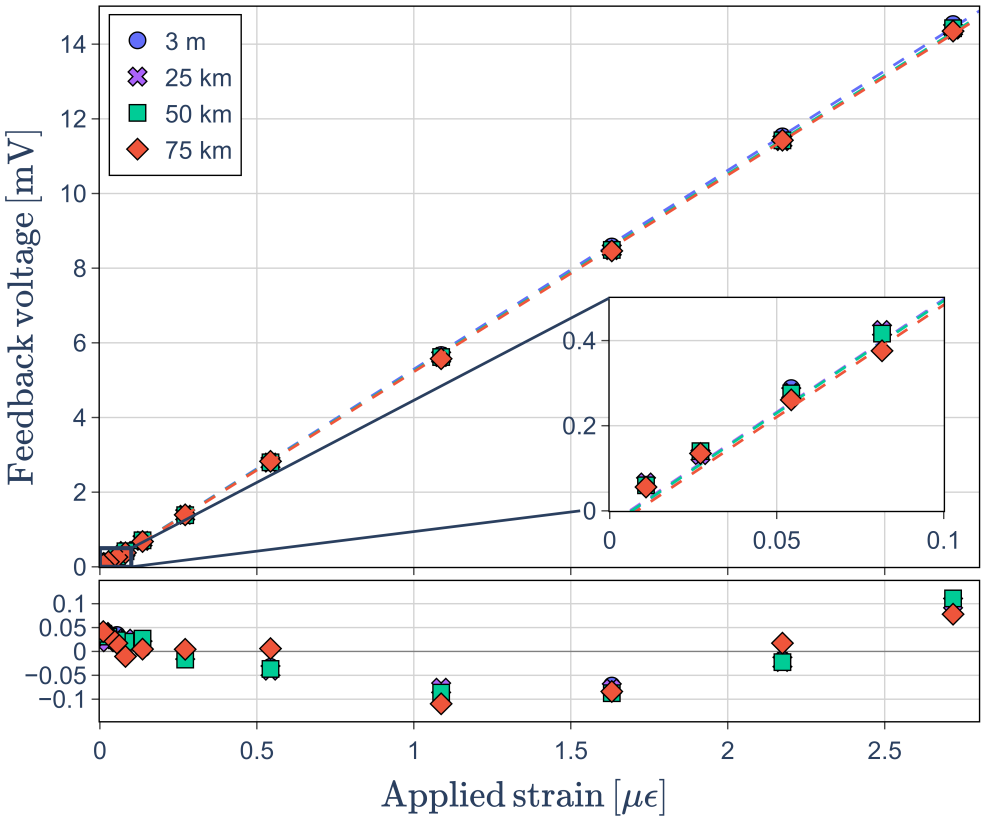

Figure 4.8: Strain response of the system with different tethers. The sensitivities for the tether length of 3 m, 25 km, 50 km, 75 km were measured to be 5.33 mV/$\mu\varepsilon$, 5.27 mV/$\mu\varepsilon$, 5.28 mV/$\mu\varepsilon$, and 5.27 mV/$\mu\varepsilon$, with a limit of detection of 22 $n\varepsilon$, 22 $n\varepsilon$, 24 $n\varepsilon$, 23 $n\varepsilon$ respectively. The inset shows a magnification of the measurements up to 100 $n\varepsilon$. The residual from a linear fit is shown below the figure.

cies up to 100 kHz. The 3 regimes can be clearly identified in this plot and the dynamic range of the system can be obtained. At the lowest frequencies, we observe a constant response from the feedback signal, with the photodiode signal being minimal. With increasing frequency the lower gain leads to a less tight lock, resulting in a response in the photodiode intensity. At even higher frequencies, the photodiode amplitude and the feedback voltage remain linearly correlated with the amplitude of the photodiode signal increasing relative to the amplitude of the feedback signal, which is apparent through the distinct displaced lines. Interestingly, saturation of the highest amplitude signals leads to a curvature and even a negative correlation at the highest photodiode amplitudes. Fig. 4.10 shows that the linear dynamic range of the feedback and photodiode signals is around 30 dB and 50 dB, respectively, at any of the frequencies. This corresponds to the strain measurement range from about 25 nε to 20 $\mu\varepsilon$ using the feedback signal and up to 2 mε using the photodiode/intensity

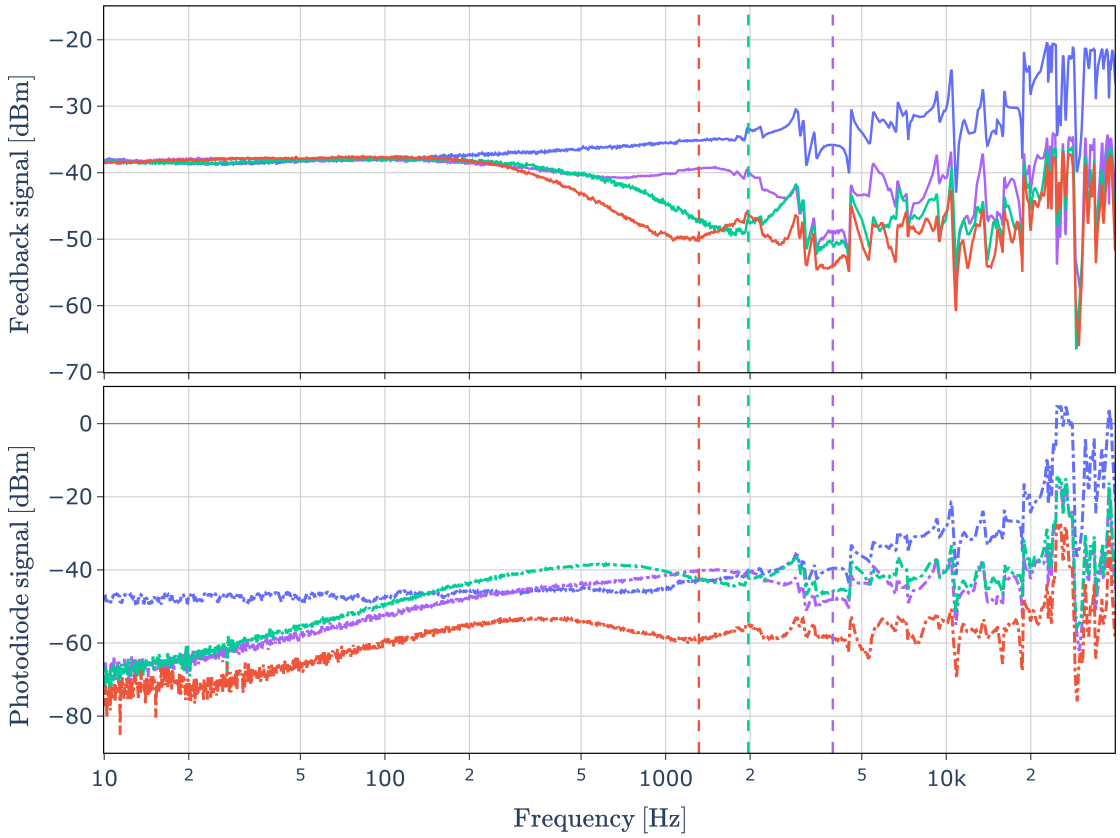

Figure 4.9: Frequency response with (a) feedback signal (solid) and (b) photodiode signal (dotted). 3m (blue), 25 km (purple), 50 km (green), 75 km (red). The dashed lines of the respective colors represent the cut-off frequency due to the round-trip time delay.

signal.

The investigation of the phase information from the frequency response from Fig. 4.9 for a fiber tether of 50 km is shown in Fig. 4.11. This information on the acoustic phase difference was obtained by comparing the difference in phase between the strain applied to the mandrel and the feedback signal by the frequency response analyzer (Liquid instruments, Moku:Go). Due to the time-of-flight delay, we expect an accumulation of phase that is linearly proportional to length of the fiber used. From the slope of the phase plot, we found the time-of-flight for fiber of 25 km, 50 km, 75 km to be 132 μs, 254 μs and 377 μs respectively.

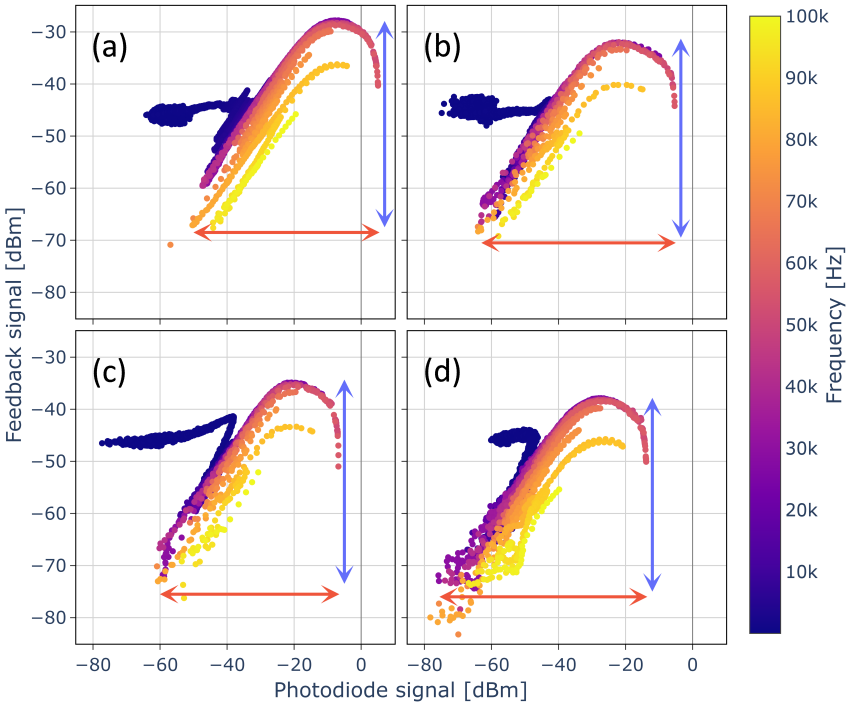

Figure 4.10: Correlation between feedback signal and photodiode signal for (a) 3 m, (b) 25 km, (c) 50 km, and (d) 75 km. The red and blue arrows represent the dynamic range for the feedback and photodiode signals, respectively.

4.3.3 Impulse response

The impulse response of the system was measured to further characterize the acoustic frequency response of the system. It was determined by observing the frequency output of the system when an impulse, modeled as a Dirac delta function, is sent as the input to the piezo mandrel. Assuming that our strain sensor is a linear time-invariant system, the impulse response can be determined from the derivative of the step response. For low applied strain this is a valid assumption as the error signal is then linearly correlated to the degree of detuning from resonance. Here, the impulse response was calculated through a finite-difference derivative of the feedback and photodiode signal response when the voltage applied to the PZT cylinder was changed from 0 to 20 V within less than 1 μs. The power spectral density of the impulse response was calculated using Python combined with the SciPy signal processing package.

The measured acoustic impulse response with each fiber tether (3 m, 25 km, 50 km,

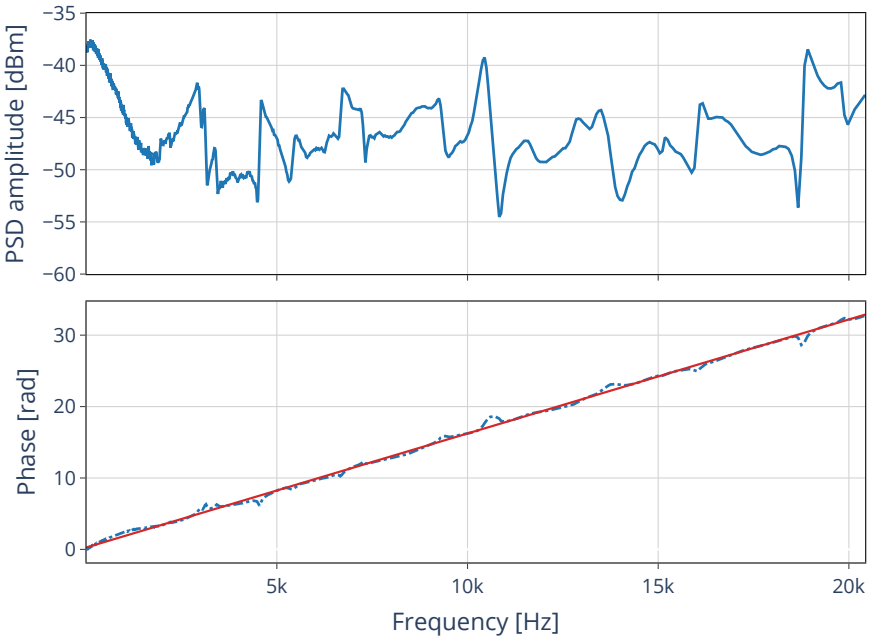

Figure 4.11: Relative phase of feedback signal with respect to applied strain at different frequencies with a 50 km tether. A linear fit of the phase gives the time-of-flight delay, which was found to be 254 μs.

75 km) is shown in Fig. 4.12. In the time domain, the photon time-of-flight delay can be readily determined from the left panels as 130 μs, 252 μs, and 376 μs for the four different tether lengths. These values are consistent with an effective refractive index of approximately $n_{\text{eff}} = 1.48$. The respective corresponding frequency responses may be compared with the analysis provided in Fig. 4.9. As was observed in Fig. 4.9, the feedback signal response is largely flat from subsonic frequencies to a cut-off frequency that depends on the tether length. At frequencies above the cutoff frequency the feedback and photodiode signals are correlated and exhibit the many of the same resonance frequencies associated with the PZT cylinder. Compared to the frequency sweep experiment shown above, the impulse response better captures the strongest resonances at 25 kHz without saturation.

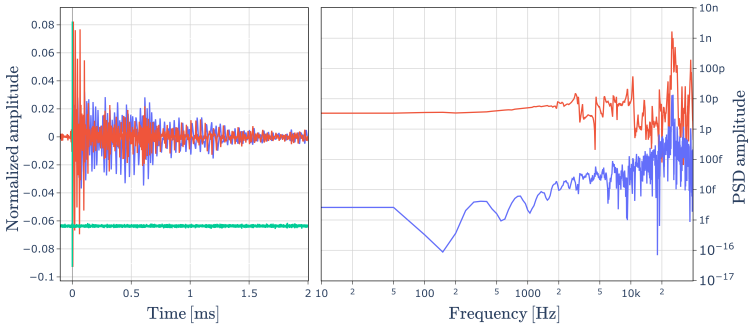

(a) 0 km

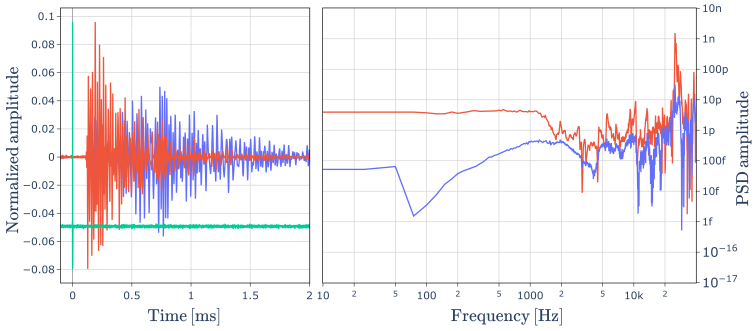

(b) 25 km

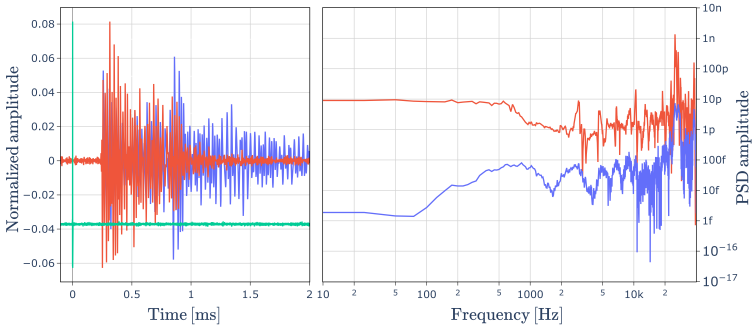

(c) 50 km

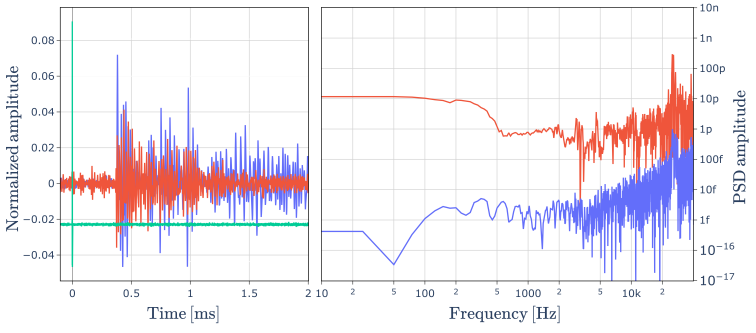

(d) 75 km

Figure 4.12: Impulse response of the feedback (red) and photodiode (blue) signals in the time and frequency domain for tether lengths of (a) 3 m, (b) 25 km, (c) 50 km, and (d) 75 km.

4.3.4 Sound recording

To demonstrate the fidelity with which sound can be recorded using the 75 km tether, we amplitude-modulated the PZT cylinder with a hydrophone recording of a humpback whale song with dolphin calls by Ocean Networks Canada [131]. The feedback and photodiode signals were captured using a USB audio interface (Solid State Logic, SSL 2+).

The corresponding spectrograms are shown in Fig. 4.13. From these figures it is evident that the feedback signal shows a clearer response to low frequencies, evident from the whale calls below 200 Hz, while also reproducing high frequency harmonics of humpback whale song. The photodiode signal exhibits higher sensitivity for higher frequencies but has a lower overall signal-to-noise ratio due to much higher background noise, apparent as "graininess" of the spectrogram. The horizontal lines in the spectrograms are due to line noise from the photodiode amplifier.

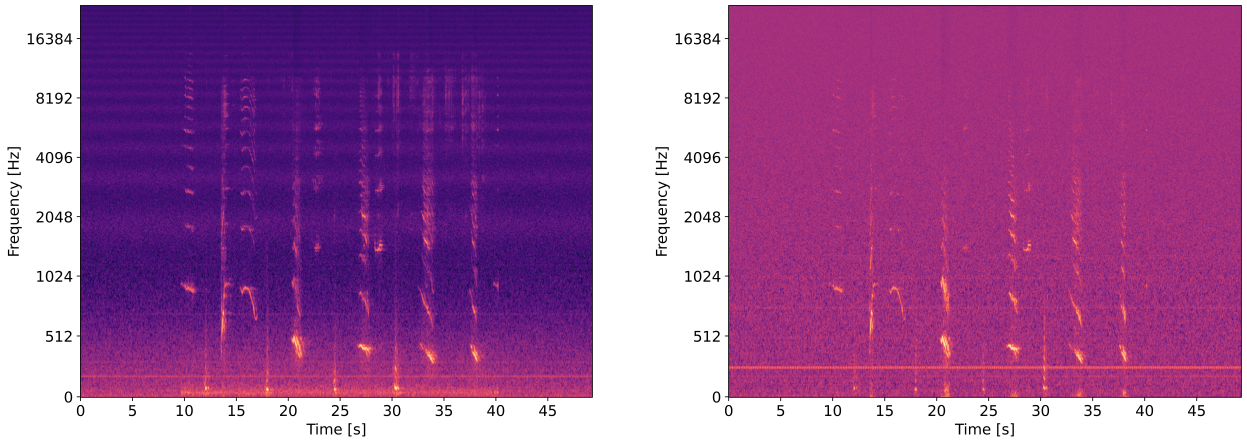

(a) Feedback signal

(b) Photodiode signal

Figure 4.13: Spectrograms of the audio recording with a 75 km tether with feedback signal (left) and photodiode signal (right). The spectrograms were generated with a Hanning window size of 8192 and plotted on a Mel scale.

4.3.5 Noise characterization

An Allan-Werle variance analysis was performed to analyze the noise characteristics of the system. Werle *et al.* first introduced this technique to identify the sampling interval that provides the best detection limit in absorption spectroscopy [132], and the method has since then been used for frequency stability analysis in inertial sensors [133]. Aside from yielding the optimized sampling interval, the Allan-Werle analysis also provides information on the type of noise present in the system.

Here, the feedback signal and photodiode signal were sampled at 100 kS/s for 120 s with the laser locked to the resonance, and the overlapping Allan deviation was calculated with different sampling intervals (Fig. 4.14). The slope of the curve provides information on the properties of noise present.

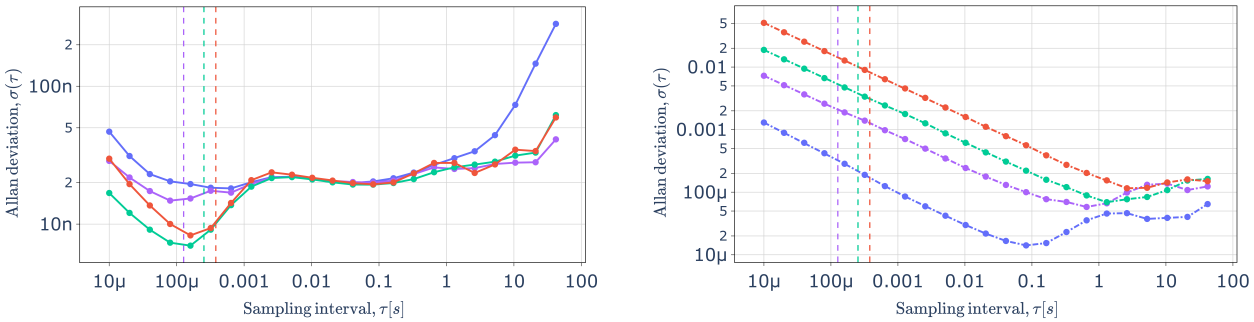

(a) Feedback signal

(b) Photodiode signal

Figure 4.14: Allan deviation of the feedback signal and photodiode for 3 m (blue), 25 km (purple), 50 km (green), 75 km (red) tethers. The dashed lines correspond to the photon flight times along the fiber tethers.

For the feedback signal, we identified three different noise sources: (1) For short sampling intervals, the slope of the curves, for each tether is between $d\sigma(\tau)/d\tau$ = -0.4 and -0.6, indicating white noise as the dominant noise type; (2) for sampling intervals between 0.01 s and 0.1 s, the slope of approximately zero can be attributed to flicker noise, which likely originates in the FPGA electronics; (3) for larger sampling intervals with a slope of +1, a drift caused by changes in the temperature was determined.

For the photodiode signal, the slope $d\sigma(\tau)/d\tau = -0.5$ for each of the tethers, implying that white noise is the dominant noise type. The magnitude of the Allan variance, $\sigma(\tau)$ strongly depends on the length of the fiber and is largest for the longest tether as one might expect given the large loss of light intensity along the fiber tethers. The observed shift of the optimal sampling interval from 0.1 s to 2 s with increasing fiber length is consistent with the expected lower signal to noise ratio for the long tethers (see also Fig 4.6b). By contrast, the feedback signal is largely immune to the length of the fiber tether.

4.4 Coherent PDH system

With the configuration presented above, we are amplifying the light in the return beam. Light intensity noise is unfortunately also amplified, resulting in a low signal-to-noise ratio of the photodiode signal for very long tethers. To improve the signal-to-noise of the error signal and to extend the measurement range of the strain sensing system, we implemented the coherent Pound-Drever-Hall technique, first reported by Liu *et al.* with our current setup using a current-modulated laser. The improved setup (shown in Fig. 4.15) replaces the photodetector with a balanced photodetector which coherently detects the light from the π-shifted grating by interfering it with light from a local oscillator (LO) arm which introduces a frequency shift from the laser.

With the conventional PDH technique, information on the phase of the reflected beam (error signal) is obtained by interfering sidebands at $\pm\Omega$ with the carrier wave at ω to generate a beat pattern using a photodetector. The error signal is extracted from the terms that are oscillating at the modulation frequency Ω (Eq. 4.3). The heterodyne method follows the same principle but in a different frequency regime. The following derivation was developed by Arthur Santos with the author's assistance and review. Figure 4.16 show the frequency components in the light before and after being detected by the balanced photodetector. The probe and LO arm both contain the sidebands generated from the current modulation of the laser and their respective electric fields are given by:

$$\begin{aligned} E_p &= E_0\left(1+\alpha\cos\Omega t\right) \\ &\quad\times\left[J_0F_\omega e^{i\omega t}+J_1F_+e^{i(\omega+\Omega)t}-J_1F_-e^{i(\omega-\Omega)t}\right], \\ E_{LO} &= E_l\left(1+\alpha\cos\Omega t\right) \\ &\quad\times\left[J_0e^{i\omega t}+J_1e^{i(\omega+\Omega)t}-J_1e^{i(\omega-\Omega)t}\right]e^{-i\Omega t+i\Phi(t)}, \end{aligned} \tag{4.9}$$

where E_0 and E_l are the field amplitudes, α is the amplitude modulation depth, ω is the carrier frequency, Ω is the current modulation frequency, Ω_0 is the acousto-optic modulation frequency, F is the reflection coefficient of the cavity, J_0 and J_1 are Bessel functions of the first kind. Following the coherent detection by the balanced photodetector, the beat frequency components are isolated by a band pass filter (Fig. 4.16). These components are similar to what one would expect in the conventional PDH but centered around the acoustic-optic modulator (AOM) modulation shift frequency Ω_0 in place of the carrier wave frequency ω. An frequency doubler is used to simulate the effect of a photodetector and interfere the sidebands with the center frequency to retrieve a similar amplified error signal

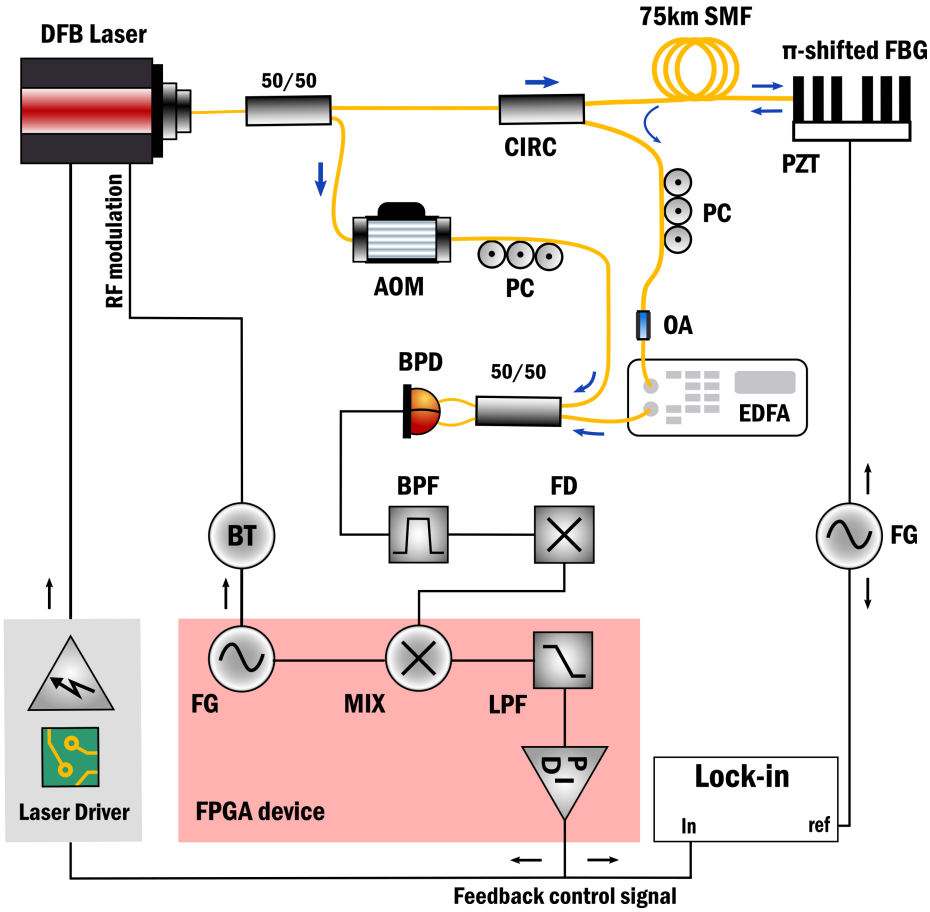

Figure 4.15: Coherent strain sensing setup. DFB: distributed feedback; RF: radio frequency; BT: bias-tee; AOM: acousto-optic modulator; PC: polarization controller; CIRC: circulator; SMF: single mode fiber; OA: optical attenuator; EDFA: erbium-doped fiber amplifier; BPD: balanced photodetector; BPF: band-pass filter; FD: frequency doubler; FPGA: field-programmable gate array; MIX: mixer; FG: function generator; LPF: low-pass filter.

at the modulation frequency Ω (highlighted in red in Figure 4.16) that is given by:

$$g(\omega) \approx 4kG^2R^2P_0P_lJ_0^3\left(J_1\frac{d|F(\omega)|^2}{d\omega}\Omega + 2\alpha J_0|F|^2\right), \tag{4.10}$$

where k is the frequency doubling coefficient, R and G are the responsivity and the trans-impedance gain of the balanced photodetector, respectively. Compared to the previously derived heterodyne PDH error signal [114], an additional term, $4kG^2r^2P_0P_l(2\alpha J_0^4|F|^2)$ appears in Eq. 4.10. That term adds a DC offset in the off-resonance region of the error signal, resulting in a slight distortion of the error signal line shape. These effects were also observed in a strain sensor that employs the conventional PDH method with a current-modulated

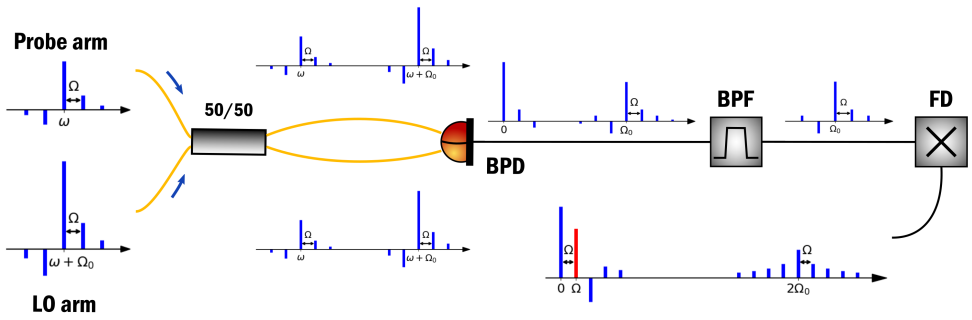

Figure 4.16: Diagram showing the evolution of the frequency components. BPD: balanced photodetector; BPF: band-pass filter; FD: frequency doubler; ω is the carrier frequency; Ω_0 is the modulation frequency; Ω is the acousto-optic modulation frequency. The frequency component shown in red correspond to $g(\omega)$ in Eq. 4.10. The diagram explicitly includes the low frequency components resulting from a non-ideal setup. Figure made by Arthur Giron-Santos.

laser [134].

This amplified error signal can provide a tight lock, and the acoustic signal is obtained from the feedback voltage as before. The circuit design for the band-pass filter and frequency doubler can be found in Appendix C.1.2. Details on the mathematical description of the error signal and on the experimental results are given in a forthcoming publication.

4.4.1 Improvement of error signal SNR

Fig. 4.17a shows measurements of the error signal curve for 3 m, 25 km, 50 km, and 75 km of fiber. The power in the LO arm and the relative polarization between the arms were adjusted to optimize the SNR of the error signal. The second row in Fig. 4.17 shows the error signals obtained for 75 km of fiber with optical attenuators of 10, 20, 27, and 32 dB in the probe arm. An EDFA was used to boost the return signal for the 27 dB and 32 dB attenuators.

Fig. 4.17b shows the SNR improvement of the PDH error signal as the power of the LO arm was increased from -8 to 2 dBm for the 75 km fiber tether, with a constant probe power of -26.0 dBm. The SNR was determined using the ratio between the peak-to-peak voltage and the standard deviation of the baseline.

At a power of more than -3 dBm in the LO arm, the SNR is no longer improved and remains constant at 26 dB. Increasing the power in the LO arm above -3 dBm produces thermal noise [135, 30], shot noise [136], and noise induced by stimulated Brillouin scattering [137, 138] which then offsets the advantage of heterodyning the weak probe signal.

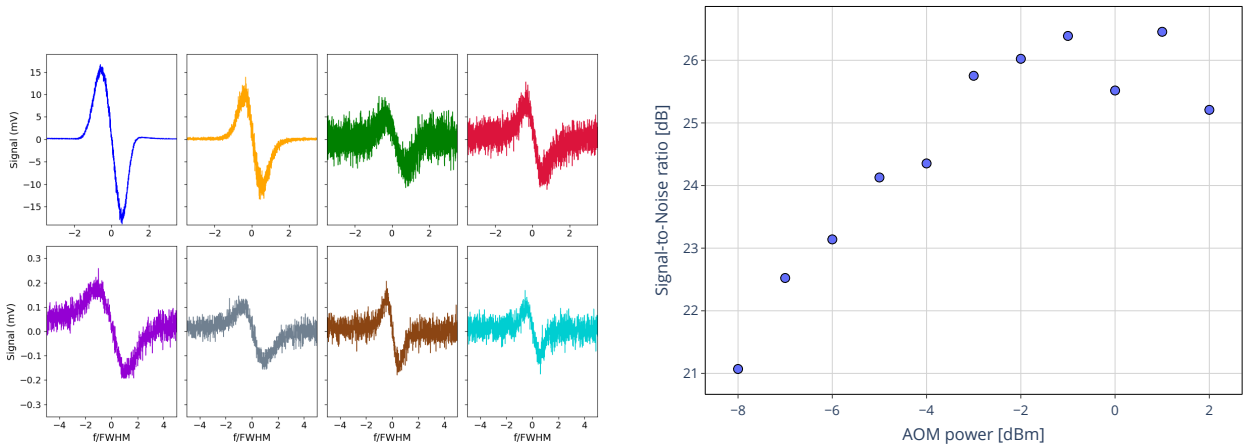

(a) Error signal curves

(b) SNR improvement

Figure 4.17: (a) Error signal curves for fiber lengths of 3 m (blue), 25 km (yellow), 50 km (green), and 75 km (red), and in the second row for 75 km of fiber with additional attenuations of 10 dB (purple), 20 dB (gray), 27 dB (brown), and 32 dB (cyan). (b) SNR improvement as the AOM power increases for 75 km of fiber.

The full sensor characterization was performed by another PhD candidate, Arthur-Giron Santos, and can be found in the submitted publication.

4.5 Summary

In this chapter, we demonstrated the design, implementation, and performance evaluation of a long-range fiber-optic strain sensing system employing a diode laser frequency-locked to the resonance of a π-shifted fiber Bragg grating. Through detailed characterization of both the feedback control signal and the photodiode response, the system was shown to deliver a sensitivity of approximately 5.3 mV/$\mu\varepsilon$, with a minimum detectable strain below 30 $n\varepsilon$. Its operational bandwidth extended from DC to 100 kHz, and the linear dynamic range reached about 30 dB, corresponding to strains from tens of nano-strain up to tens of micro-strain. Importantly, these metrics remained unchanged even when the sensing head was deployed with fiber tethers up to 75 km in length.

While the strain sensor head, i.e. the π-shifted FBG, is not fundamentally different from those described in previous reports [118, 31, 119] and has a similar sensitivity to strain, we demonstrate that the weak reflected intensity is sufficient to provide a robust laser lock over a surprisingly large range of acoustic frequencies. Interestingly, the propagation delay of several hundred microseconds does not prevent us from recording acoustic signals at frequencies in the kilohertz range.

The chapter further introduced a coherent Pound–Drever–Hall (PDH) detection scheme designed to address limitations imposed by low probe power and noise amplification in conventional configurations. By heterodyning the weak reflected signal with a frequency-shifted local oscillator and coherently detecting it with a balanced photodiode, the coherent PDH method enhanced the signal-to-noise ratio of the error signal by more than an order of magnitude. This improvement enabled reliable laser locking with return powers as low as –58 dBm (< 2 nW), effectively eliminating the need for EDFAs and extending the theoretical maximum tether length to beyond 150 km.

The advantages of the system lie in its passive nature – it can be deployed with all active and serviceable components at one end. The fiber optic cable and fiber sensor can also be made rugged for use in hostile environments such as on the ocean floor or in remote locations, with minimal maintenance and without concern for power delivery.

Chapter 5

Conclusion and Future Work

5.1 Thesis Summary

This thesis presents two different optical sensing systems that use optical resonances to enhance light-matter interactions for applications in environmental and human health monitoring. The first approach uses plasmonic field confinement in metallic nanohole arrays to investigate the diffusion kinetics of volatile organic compounds in polymer films, while the second utilizes π-shifted fiber Bragg gratings to achieve sensitive, long-range strain sensing capable of operating in harsh environments. Although these sensing systems target distinct physical phenomena, they are unified by a common objective: to develop passive, high-sensitivity optical sensors that can measure chemical and mechanical changes beyond the capabilities of conventional techniques.

Chapter 2 provides the theoretical foundation for the VOC sensing system by deriving exact integrated solutions to Fick's second law of diffusion for analyte diffusion in thin polymer films with either permeable or impermeable substrates. These models enable more accurate determination of diffusion constants from experimental data than traditional first-order approximations and can be broadly applied to various polymer-analyte systems.

Chapter 3 demonstrates a novel real-time, on-line, cost-effective VOC sensing platform based on extraordinary optical transmission (EOT) through polymer-coated metallic nanohole arrays. The sensor measures plasmonic resonance shifts using the centroid method to allow for the detection of refractive index changes on the order of 10^{-4} RIU, enabling the investigation of the absorption and desorption dynamics of o-xylene in PDMS. Experimental data was fitted to the diffusion models derived in Chapter 2, yielding diffusion constants consistent with past work by Saunders *et al.* [34] and provided further evidence for a two-stage diffusion process of VOCs into PDMS.

While the first part of this thesis focuses on chemical sensing through plasmonic res-

onances, the second part applies the same resonance-based principles to mechanical sensing. Chapter 4 presents the design, development, and characterization of a π-FBG–based strain sensor interrogated via Pound–Drever–Hall locking method. The system achieves nanostrain-level resolution over fiber tethers up to 75 km without requiring in-line amplification, demonstrating its suitability for challenging environments. A thorough characterization of the system was performed by investigating the strain and frequency response, impulse response, and noise characteristics. By observing both the feedback control signal and reflected photodiode signal, the system is capable of measuring strain below 30 $n\varepsilon$, with operational bandwidth up to 100 kHz, and a linear dynamic range of 30 dB. Despite the propagation delay from the long tethers, we have shown that the system is capable of recording acoustic signals. In addition, we demonstrated a coherent PDH system that improved the signal-to-noise ratio of the error signal to allow for stable locking with return powers as low as -58 dBm (< 2 nW).

5.2 Future work

5.2.1 Detection of volatile organic compounds using metallic flow-through nanohole arrays

The detection and investigation of o-xylene has been demonstrated in Chapter 3, but further work can be done with using the system to investigate the diffusion of other solvents, as well as improvements to the setup to increase the sensitivity of the instrument, and its ability to measure the thickness changes to the PDMS layer.

Investigation of the diffusion other solvents into PDMS or similar polymers

In the work presented here, we primarily focused on the diffusion kinetics of o-xylene as a model compound to fully characterize and validate the sensing system. The natural next step would be extend this approach to a wider range of VOCs, and assess the versatility of the nanohole array sensor for broader chemical detection using PDMS and possibly related polymers such as poly-diphenyl siloxane (PDPS) [139]. Preliminary experiments using acetone as a test analyte with the gas bubbler system at Queen's University (Fig. 5.1) highlight the potential of this direction.

Acetone has a lower refractive index than PDMS ($n_{\text{acetone}} = 1.3483$), and higher absorption and diffusion constants into PDMS than o-xylene [34]. This is evident from Fig. 5.1 as we observe a blue shift in the centroid wavelength and faster absorption and desorption of

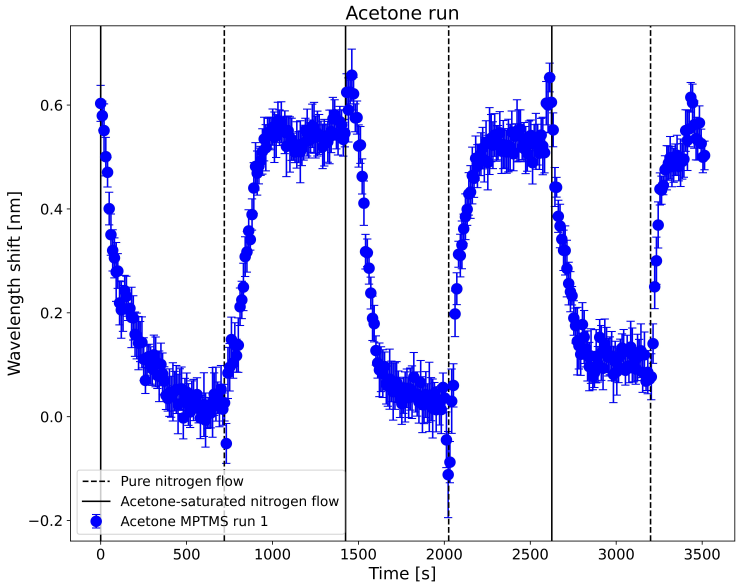

Figure 5.1: Repeated absorption and desorption run with acetone

the solvent. These preliminary results also demonstrate the feasibility of identifying different VOCs based on their kinetics and refractive indices.

Sensitivity improvements

In the nanohole array gas sensing experiments presented in this work, the plasmonic resonance shift was measured using the centroid wavelength of the transmission spectrum. This approach was chosen because of the complex extraordinary optical transmission (EOT) spectrum and the relatively small magnitude of refractive index–induced peak shifts. Although this has proven robust, it inherently reduces sensitivity by implicitly averaging over both shifting and non-shifting parts of the spectrum. Only a portion of the broad resonance around 660 nm exhibits a systematic shift with refractive index, suggesting that isolating this spectral feature could yield more sensitive and higher-resolution sensing system.

Future work will focus on improving the sensitivity of the system through both improved data processing and nanohole array design optimization. On the software side, we are currently exploring the fitting of EOT spectrum to extract peak positions directly. Specifically, fitting the broad resonance to a combination of Lorentzian or Fano lineshapes can separate the shifting resonance from overlapping background features, reducing noise and improving the precision of plasmonic shift. We can further look into designing alternative nanohole array geometries or compositions to that allows for the isolation of the EOT resonance that

corresponds to the gold-PDMS interface. By combining these software and hardware strategies, the sensing system could achieve significantly higher sensitivity and resolution, enabling more reliable detection of weak VOC diffusion signatures in polymer films.

Interferometric EOT-based sensor

One of the assumptions that we make when modeling the diffusion kinetics with our setup is that we neglect swelling of the PDMS as the VOCs goes through the absorption and desorption phase. Although, this assumption is valid for o-xylene as we observe below 5% swelling in the film, this would not necessarily be true for other VOCs such as toluene that can see swelling up to 80% over 72 hours [62].

A promising extension of this work is the development of a dual-mode optical sensing setup that simultaneously uses the extraordinary optical transmission (EOT) response of plasmonic nanohole arrays (NHAs) in transmission and the thin-film interference fringes generated in reflection from a PDMS layer. In such a configuration, a thin layer of polydimethylsiloxane (PDMS) would be deposited atop the gold NHA structure, forming an air–PDMS–NHA multilayer stack. The EOT resonance, governed by surface plasmon polariton excitation and cavity-like transmission modes through the subwavelength apertures, would remain accessible in transmission for refractive-index sensing, as demonstrated in Chapter 3. At the same time, the partially reflective gold-coated NHA interface beneath the PDMS film can act as a back reflector, enabling thin film interferometry to retrieve the thickness of the PDMS layer from the interference fringes in the reflected spectrum as evidenced by the results presented in Section 3.4.6. The ability to extract thickness through fringe periodicity has been demonstrated extensively in thin-film reflectometry [140, 141], while recent work has shown that plasmonic nano-structures themselves can serve as functional reflectors within interferometric sensing schemes [142, 143]. Balderas-Valadez *et al.* integrated NHAs with porous silicon to combine plasmonic and interferometric sensing modes [142], and Tu *et al.* uses a micro-machined Fabry-Perot cavity to enhance the refractive index sensitivity, validating the concept of using nano-structured metal films as reflective elements [143].

Future work will focus on optimizing the PDMS layer thickness and optical properties to balance transmission of EOT resonances with sufficient reflectivity to produce high-contrast interference fringes. This will involve controlled deposition or spin-coating of PDMS films in the 10–50 μm range, where fringe spacing is well matched to the spectral resolution of standard spectrometers. Additionally, incorporating transfer-matrix modeling or FDTD simulations that account for the complex, wavelength-dependent reflection coefficient of the NHA

interface will enable more accurate thickness retrieval from measured reflectance spectra.

5.2.2 Long-range strain sensing system using a frequency-locked π-shifted grating

Fiber optic hydrophone

Current hydrophone technology is almost exclusively based on piezo-electric transducers (PZTs), i.e., electromechanical devices that produce a small voltage upon deformation. All PZT devices require voltage or current amplification and transmission of this electric signal over distances as long as 100 km. As a result, issues such as calibration, maintenance requirements, electronic noise, and signal degradation limit their performance, particularly for remote or deep-sea monitoring, and generally limit their deployment to environments near power sources such as shore stations, marine vessels, or buoys [144].

Since their first demonstration in the late 1970s, fiber-optic hydrophones (FOHs) have been recognized for their high sensitivity, immunity to electromagnetic interference, light weight, and compatibility with multiplexed large-scale sensing arrays [145]. Considerable progress has been made in both interferometric and fiber laser-based hydrophone designs. Interferometric FOHs remain the most sensitive and are widely used for scalar pressure detection in applications ranging from underwater surveillance and seismic exploration to industrial monitoring [146, 147]. Fiber laser sensors (FLS) offer an alternative approach, achieving near-thermodynamic noise limits by interrogating environmentally sensitive distributed feedback fiber lasers. Their short sensing length and wavelength-division multiplexing capability enable compact, lightweight, and scalable array systems, such as the 8-element seabed array demonstrated by Foster et al. [127]. While conventional FBG hydrophones are generally limited in sensitivity, innovations such as slow-light–enhanced FBGs have demonstrated sub-millipascal pressure resolution, highlighting their potential for future acoustic sensing applications [148].

Building on these developments, we propose the use of the long-range strain sensing system presented in this thesis toward fiber-optic hydrophone applications. Since we require a mechanical conversion from sound/pressure waves to strain, we will focus on flex tensional transducers such as cymbal-shaped transducers developed by the US Navy [149]. These transducers have a limited axial motion that results in a high radial displacement upon impingement of a sound/pressure wave. The proposed design, developed in collaboration with Sea to Shore Ltd, aims to integrate a π-phase-shifted FBG directly into one of the end caps of a cymbal hydrophone (Fig. 5.2). Embedding the grating directly into the cap will

allow the acoustic pressure-induced flexural deformation of the cymbal to be transduced into radial strain on the grating, thereby modulating its resonance wavelength.

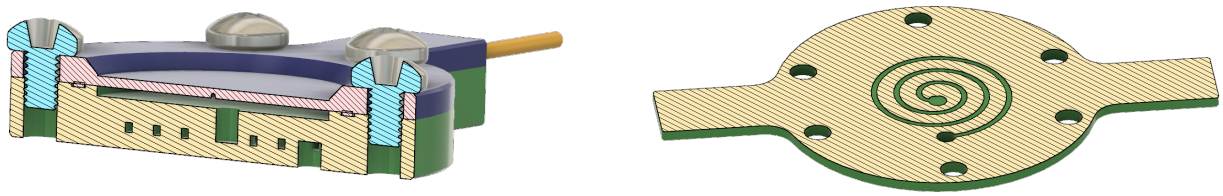

(a) Cross section of proposed design (b) Pressure compensation coil

Figure 5.2: Proposed cymbal-shaped fiber optic hydrophone design. Design developed in collaboration with Sea-to-Shore Ltd.

A critical aspect of the proposed system is pressure compensation to ensure stable operation across varying hydrostatic pressures, particularly for deep-sea deployment. the future design will incorporate an oil-filled cavity within the opposing cymbal end cap. This cavity will serve as a compliant volume, equalizing static pressure and isolating the sensing grating from quasi-static strain that could shift its operating point. A coil-shaped internal structure will be integrated into this chamber to enhance its compliance and pressure-relief characteristics, allowing the hydrophone to maintain consistent responsivity and dynamic range even at deep depths.

Free space interrogation

The coherent Pound–Drever–Hall (PDH) technique has demonstrated exceptional sensitivity under ultralow probe powers by exploiting coherent detection with a strong local oscillator, significantly improving the signal-to-noise ratio even when the reflected signal power is on the order of –58 dBm. Building on this capability, we are investigating the feasibility of extending coherent PDH interrogation beyond fiber-based sensor networks to free-space optical configurations. The primary motivation is to eliminate the dependence on long fiber tethers, which introduce propagation losses, and complexity in field-deployed sensing systems, especially in environments where fiber installation is impractical or undesirable.

Our preliminary approach replaces the conventional 75 km fiber link with a free-space propagation path, using fiber collimators to send and collect the probe light from a π-shifted fiber Bragg grating (FBG) sensor. This configuration preserves the high-resolution interrogation capability of PDH while testing the system's tolerance to alignment errors, beam divergence, and return power losses in free space.

The next stage of this work aims to replace the π-shifted FBG with alternative optical resonators that provide comparably narrow resonances suitable for PDH locking. One promising candidate is a π-shifted dielectric mirror, constructed as a multilayer Bragg stack with a localized phase shift to support a narrow transmission resonance (Fig. 5.3a). Such a structure would mimic the linewidth characteristics of a π-shifted FBG while being inherently compatible with free-space optical interrogation (Fig. 5.3b).

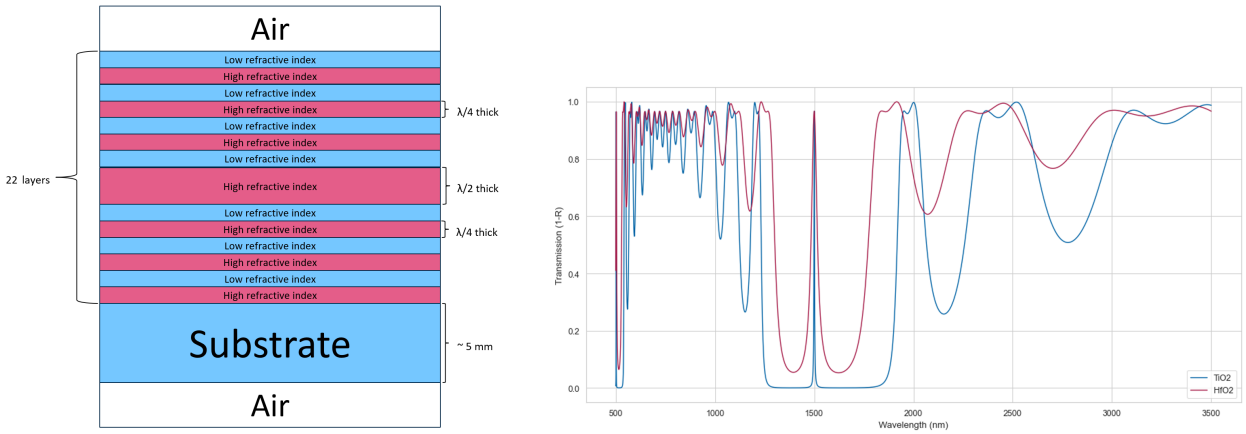

(a) Proposed design of π-shifted mirror (b) Transmission spectra for different substrates

Figure 5.3: Proposed design for π-shifted mirror with their associated transmission spectra with two different materials for the high refractive index (Titanium dioxide: blue, Hafnium dioxide: red). Figure obtained from collaborators at University of Vienna.

Transitioning fiber strain sensing into free space introduces both opportunities and challenges. On one hand, it opens new avenues for remote, passive strain sensing, where structures could be interrogated without the need for fiber coupling or embedded sensors, significantly broadening deployment scenarios — for instance, in structural health monitoring of large civil infrastructure or aerospace components, where fiber routing is impractical. On the other hand, free-space propagation introduces sensitivity to alignment drift, atmospheric turbulence [150], and mechanical vibrations, all of which could degrade the locking capabilities of the system. Furthermore, unlike fiber-integrated FBGs, dielectric stack resonators require precise angular and polarization alignment to achieve high-finesse coupling.

As our work Chapter 5 demonstrated, though, the strain sensitivity of the setup, and its associated minimal detectable strain is not affected by the degraded signal, i.e. as long as a laser can be locked to the resonator, the strain response is identical. This is in marked contrast to all sensor systems that are based on light intensity measurements. If successful, such a system would enable a new class of fully passive, remotely interrogated strain sensors,

leveraging narrow-linewidth resonators without requiring physical fiber connections between the sensor and the interrogation unit.

5.3 Overall conclusions

This thesis highlights the potential of optical resonance–based platforms to enable highly sensitive detection of chemical diffusion and mechanical strain. Continued advances in optics and photonics will be crucial for transforming these approaches into practical sensors that meet real-world demands in environmental, industrial, and structural applications.

Bibliography

[1] S. Daxini, D. Aydin, A. Giron, J. Barnes, X. Gu, and H.-P. Loock, "Long-range strain sensing system using a frequency-locked π-shifted grating," *Optics Express*, vol. 33, pp. 6039–6047, Feb 2025.

[2] E. Udd and W. B. Spillman, *Fiber optic sensors : an introduction for engineers and scientists*. Hoboken, New Jersey: John Wiley & Sons, 2nd ed., 2008.

[3] B. H. Lee, Y. H. Kim, K. S. Park, J. B. Eom, M. J. Kim, B. S. Rho, and H. Y. Choi, "Interferometric fiber optic sensors," *Sensors*, vol. 12, no. 3, pp. 2467–86, 2012.

[4] D. Aydin, J. A. Barnes, and H.-P. Loock, "In-fiber interferometry sensors for refractive index," *Applied Physics Reviews*, vol. 10, no. 1, p. 011307, 2023.

[5] F. Vollmer and S. Arnold, "Whispering-gallery-mode biosensing: label-free detection down to single molecules," *Nature Methods*, vol. 5, no. 7, pp. 591–596, 2008.

[6] G. Gagliardi and H.-P. Loock, *Cavity-Enhanced Spectroscopy and Sensing*, vol. 179 of *Springer Series in Optical Sciences*. Berlin, Heidelberg: Springer Nature, 2014 ed., 2013.

[7] A. Othonos, K. Kalli, and G. E. Kohnke, "Fiber Bragg gratings: Fundamentals and applications in telecommunications and sensing," *Physics Today*, vol. 53, no. 5, pp. 61–62, 2000.

[8] J. Divya, S. Selvendran, A. S. Raja, and A. Sivasubramanian, "Surface plasmon based plasmonic sensors: A review on their past, present and future," *Biosensors and Bioelectronics: X*, vol. 11, p. 100175, 2022.

[9] T. W. Ebbesen, H. J. Lezec, H. F. Ghaemi, T. Thio, and P. A. Wolff, "Extraordinary optical transmission through sub-wavelength hole arrays," *Nature*, vol. 391, no. 6668, pp. 667–669, 1998.

[10] J. Homola, "Surface plasmon resonance sensors for detection of chemical and biological species," *Chemical Reviews*, vol. 108, no. 2, pp. 462–493, 2008.

[11] H. A. Bethe, "Theory of diffraction by small holes," *Physical Review*, vol. 66, no. 7-8, pp. 163–182, 1944.

[12] R. Gordon, D. Sinton, K. L. Kavanagh, and A. G. Brolo, "A new generation of sensors based on extraordinary optical transmission," *Accounts of Chemical Research*, vol. 41, no. 8, pp. 1049–1057, 2008.

[13] X. Lan, B. Cheng, Q. Yang, J. Huang, H. Wang, Y. Ma, H. Shi, and H. Xiao, "Reflection based extraordinary optical transmission fiber optic probe for refractive index sensing," *Sensors and actuators. B, Chemical*, vol. 193, pp. 95–99, 2014.

[14] A. G. Brolo, S. C. Kwok, M. G. Moffitt, R. Gordon, J. Riordon, and K. L. Kavanagh, "Enhanced fluorescence from arrays of nanoholes in a gold film," *Journal of the American Chemical Society*, vol. 127, no. 42, pp. 14936–14941, 2005.

[15] C. Escobedo, "On-chip nanohole array based sensing: a review," *Lab on a Chip*, vol. 13, no. 13, pp. 2445–2463, 2013.

[16] J. Ferreira, M. J. L. Santos, M. M. Rahman, A. G. Brolo, R. Gordon, D. Sinton, and E. M. Girotto, "Attomolar protein detection using in-hole surface plasmon resonance," *Journal of the American Chemical Society*, vol. 131, no. 2, pp. 436–437, 2009.

[17] J. Gomez-Cruz, S. Nair, G. Ascanio, and C. Escobedo, "Flow-through nanohole array based sensor implemented on analogue smartphone components," in *Society of Photo-Optical Instrumentation Engineers (SPIE) Conference Series*, vol. 10346, p. 1034624, 2017.

[18] J.-C. Yang, J. Ji, J. M. Hogle, and D. N. Larson, "Multiplexed plasmonic sensing based on small-dimension nanohole arrays and intensity interrogation," *Biosensors & bioelectronics*, vol. 24, no. 8, pp. 2334–2338, 2009.

[19] J. Gomez-Cruz, S. Nair, A. Manjarrez-Hernandez, S. Gavilanes-Parra, G. Ascanio, and C. Escobedo, "Cost-effective flow-through nanohole array-based biosensing platform for the label-free detection of uropathogenic e. coli in real time," *Biosensors & bioelectronics*, vol. 106, pp. 105–110, 2018.

[20] J. Ji, J. G. O'Connell, D. J. Carter, and D. N. Larson, "High-throughput nanohole array based system to monitor multiple binding events in real time," *Analytical chemistry*, vol. 80, no. 7, pp. 2491–8, 2008.

[21] L. Kalvoda, J. Jakoubková, M. Burda, P. Kwiecien, I. Richter, and J. Kopeček, "Fiber optic sensor of ammonia gas using plasmonic extraordinary optical transmission," *Sensors*, vol. 23, no. 8, p. 4065, 2023.

[22] Y. Zhao, K. Mukherjee, K. D. Benkstein, L. Sun, K. L. Steffens, C. B. Montgomery, S. Guo, S. Semancik, and M. E. Zaghloul, "Miniaturized nanohole array based plasmonic sensor for the detection of acetone and ethanol with insights into the kinetics of adsorptive plasmonic sensing," *Nanoscale*, vol. 11, no. 24, pp. 11922–11932, 2019.

[23] J. A. Barnes, R. S. Brown, J. Cipot-Wechsler, C. M. Crudden, J. Du, H.-P. Loock, and K. Plett, "Long-period gratings in chemical sensing," vol. 7099, pp. 70992C–70992C–8, SPIE, 2008.

[24] S. A. Vasil'ev, O. I. Medvedkov, I. G. Korolev, A. S. Bozhkov, A. S. Kurkov, and E. M. Dianov, "Fibre gratings and their applications," *Quantum electronics*, vol. 35, no. 12, pp. 1085–1103, 2005.

[25] A. I. Freytag, A. G. MacLean, M. Abtahi, J. A. Barnes, and H. P. Loock, "All fiber-optic viscosity, density, and temperature measurements of liquids using a photothermally actuated cantilever," *Applied Physics B-Lasers and Optics*, vol. 124, no. 11, 2018.

[26] A. Cusano, A. Cutolo, and J. Albert, *Fiber Bragg grating sensors recent advancements, industrial applications and market exploitation*. Saif Zone, Sharjah, United Arab Emirates: Bentham Science Publishers Ltd., 2011.

[27] S. Deepa and B. Das, "Interrogation techniques for π-phase-shifted fiber Bragg grating sensor: A review," *Sensors and Actuators A: Physical*, vol. 315, p. 112215, 2020.

[28] B. E. A. Saleh and M. C. Teich, *Fundamentals of photonics*. Hoboken, N.J: Wiley-Interscience, 2nd ed., 2007.

[29] S. M. Melle, K. Liu, and R. M. Measures, "A passive wavelength demodulation system for guided-wave Bragg grating sensors," *IEEE Photonics Technology Letters*, vol. 4, no. 5, pp. 516–518, 1992.

[30] S. X. Zhao, Q. W. Liu, J. G. Chen, and Z. Y. He, "Resonant fiber-optic strain and temperature sensor achieving thermal-noise-limit resolution," *Optics Express*, vol. 29, no. 2, pp. 1870–1878, 2021.

[31] D. Gatti, G. Galzerano, D. Janner, S. Longhi, and P. Laporta, "Fiber strain sensor based on a π-phase-shifted Bragg grating and the Pound-Drever-Hall technique," *Optics express*, vol. 16, no. 3, p. 1945, 2008.

[32] J. Crank, *The mathematics of diffusion.* Oxford: Clarendon Press, 1956.

[33] C. M. Balik, "On the extraction of diffusion coefficients from gravimetric data for sorption of small molecules by polymer thin films," *Macromolecules*, vol. 29, no. 8, pp. 3025–3029, 1996.

[34] J. E. Saunders, H. Chen, C. Brauer, M. Clayton, and H.-P. Loock, "Two distinct mechanisms upon absorption of volatile organic compounds into siloxane polymers," *Soft matter*, vol. 14, no. 12, pp. 2206–2218, 2018.

[35] J. E. Saunders, H. Chen, C. Brauer, M. Clayton, W. Chen, J. A. Barnes, and H. P. Loock, "Quantitative diffusion and swelling kinetic measurements using large-angle interferometric refractometry," *Soft Matter*, vol. 11, no. 45, pp. 8746–57, 2015.

[36] H. Megahd, M. Carlotti, M. Martusciello, L. Magnasco, A. Pucci, D. Comoretto, and P. Lova, "Controlled molecular diffusion in fluorescent polymer films for label-free detection of volatile organic compounds," *Advanced Sensor Research*, vol. 3, no. 1, p. 2300114, 2024.

[37] M. Prabhugouda, M. T. Lagare, N. N. Mallikarjuna, B. V. K. Naidu, and T. M. Aminabhavi, "A novel spectrophotometric method to measure the diffusion coefficient of aniline in benzene at 298.15 K," *Journal of Molecular Liquids*, vol. 116, no. 1, pp. 51–54, 2005.

[38] H. Chen, J. E. Saunders, S. Borjian, X. Wu, C. M. Crudden, D.-X. Xu, and H.-P. Loock, "Tetrasulfide-functionalized mesoporous silica on nanowire ring resonators for detection of aqueous lead, Pb(II)," *Advanced Sustainable Systems*, vol. 3, no. 1, p. 1800084, 2019.

[39] R. Shang, Y. Deng, W. Bao, X. Cai, L. Cao, Y. Liu, F. Cong, H. Zhang, X. Wang, X. Yan, and J. Xie, "Diffusion behavior and kinetics for the vapor phase infiltration of

trimethylaluminum in poly(ethylene oxide): An in situ quartz crystal microgravimetry study," *ACS Applied Materials & Interfaces*, vol. 16, no. 47, pp. 64907–64915, 2024.

[40] S. J. Lue, S. F. Wang, L. D. Wang, W. W. Chen, K.-M. Du, and S. Y. Wu, "Diffusion of multicomponent vapors in a poly(dimethyl siloxane) membrane," *Desalination*, vol. 233, no. 1, pp. 277–285, 2008.

[41] D. Kouzoudis, T. Baimpos, and G. Samourgkanidis, "A new method for the measurement of the diffusion coefficient of adsorbed vapors in thin zeolite films, based on magnetoelastic sensors," *Sensors*, vol. 20, no. 11, p. 3251, 2020.

[42] J. E. Saunders, *Refractometry studies of the optical properties of polymer films and the development of polymer coated refractive index sensors*. Thesis, 2016.

[43] P. Ciccioli, C. Silibello, S. Finardi, N. Pepe, P. Ciccioli, F. Rapparini, L. Neri, S. Fares, F. Brilli, M. Mircea, E. Magliulo, and R. Baraldi, "The potential impact of biogenic volatile organic compounds (BVOCs) from terrestrial vegetation on a Mediterranean area using two different emission models," *Agricultural and Forest Meteorology*, vol. 328, p. 109255, 2023.

[44] R. Epping and M. Koch, "On-site detection of volatile organic compounds (VOCs)," *Molecules*, vol. 28, no. 4, p. 1598, 2023.

[45] C. Di Fiore, P. Pandolfi, F. Carriera, A. Iannone, G. Settimo, V. Mattei, and P. Avino, "The presence of aromatic substances in incense: Determining indoor air quality and its impact on human health," *Applied Sciences*, vol. 13, no. 12, p. 7344, 2023.

[46] X. Bai, W. Liu, B. Wu, S. Liu, X. Liu, Y. Hao, W. Liang, S. Lin, L. Luo, S. Zhao, C. Zhu, J. Hao, and H. Tian, "Emission characteristics and inventory of volatile organic compounds from the chinese cement industry based on field measurements," *Environmental Pollution*, vol. 316, p. 120600, 2023.

[47] M. Fan, T. F. Rakotondrabe, G. Chen, and M. Guo, "Advances in microbial analysis: Based on volatile organic compounds of microorganisms in food," *Food Chemistry*, vol. 418, p. 135950, 2023.

[48] A. Erler, D. Riebe, T. Beitz, H. G. Löhmannsröben, D. Grothusheitkamp, T. Kunz, and F. J. Methner, "Characterization of volatile metabolites formed by molds on barley by mass and ion mobility spectrometry," *Journal of Mass Spectrometry*, vol. 55, no. 5, p. e4501, 2020.

[49] Q. Pan, Q.-Y. Liu, J. Zheng, Y.-H. Li, S. Xiang, X.-J. Sun, and X.-S. He, "Volatile and semi-volatile organic compounds in landfill gas: Composition characteristics and health risks," *Environment International*, vol. 174, p. 107886, 2023.

[50] R. Montero-Montoya, R. López-Vargas, and O. Arellano-Aguilar, "Volatile organic compounds in air: Sources, distribution, exposure and associated illnesses in children," *Annals of Global Health*, vol. 84, no. 2, pp. 225–238, 2018.

[51] M. D. Masekameni, R. Moolla, M. Gulumian, and D. Brouwer, "Risk assessment of benzene, toluene, ethyl benzene, and xylene concentrations from the combustion of coal in a controlled laboratory environment," *International Journal of Environmental Research and Public Health*, vol. 16, no. 1, p. 95, 2019.

[52] J. L. González, A. Pell, M. López-Mesas, and M. Valiente, "Simultaneous determination of BTEX and their metabolites using solid-phase microextraction followed by HPLC or GC/MS: An application in teeth as environmental biomarkers," *Science of The Total Environment*, vol. 603-604, pp. 109–117, 2017.

[53] N. Baimatova, B. Kenessov, J. A. Koziel, L. Carlsen, M. Bektassov, and O. P. Demyanenko, "Simple and accurate quantification of BTEX in ambient air by SPME and GC-MS," *Talanta*, vol. 154, pp. 46–52, 2016.

[54] M. R. Lee, C. M. Chang, and J. Dou, "Determination of benzene, toluene, ethylbenzene, xylenes in water at sub-ng l-1 levels by solid-phase microextraction coupled to cryo-trap gas chromatography-mass spectrometry," *Chemosphere*, vol. 69, no. 9, pp. 1381–7, 2007.

[55] H. Shim, B. Hwang, and S. T. Yang, "Separation of benzene, toluene, ethylbenzene, and xylenes by micellar electrokinetic capillary chromatography," *Environmental Technology*, vol. 25, no. 1, pp. 51–6, 2004.

[56] C. L. Arthur and J. Pawliszyn, "Solid phase microextraction with thermal desorption using fused silica optical fibers," *Analytical Chemistry*, vol. 62, no. 19, pp. 2145–2148, 1990.

[57] J. Pawliszyn, *Applications of solid phase microextraction*. RSC chromatography monographs, Cambridge: Royal Society of Chemistry, 1st ed., 1999.

[58] P. A. Martos and J. Pawliszyn, "Calibration of solid phase microextraction for air analyses based on physical chemical properties of the coating," *Analytical Chemistry*, vol. 69, no. 2, pp. 206–215, 1997.

[59] J. B. Pawliszyn, *Solid phase microextraction : theory and practice*. John Wiley & Sons, 1997.

[60] A. Mata, A. J. Fleischman, and S. Roy, "Characterization of polydimethylsiloxane (PDMS) properties for biomedical micro/nanosystems," *Biomedical Microdevices*, vol. 7, no. 4, pp. 281–93, 2005.

[61] N. E. Stankova, P. A. Atanasov, R. G. Nikov, R. G. Nikov, N. N. Nedyalkov, T. R. Stoyanchov, N. Fukata, K. N. Kolev, E. I. Valova, J. S. Georgieva, and S. A. Armyanov, "Optical properties of polydimethylsiloxane (PDMS) during nanosecond laser processing," *Applied Surface Science*, vol. 374, pp. 96–103, 2016.

[62] C. V. Rumens, M. A. Ziai, K. E. Belsey, J. C. Batchelor, and S. J. Holder, "Swelling of PDMS networks in solvent vapours; applications for passive RFID wireless sensors," *Journal of Materials Chemistry C*, vol. 3, no. 39, pp. 10091–10098, 2015.

[63] R. Howley, B. D. MacCraith, K. O'Dwyer, H. Masterson, P. Kirwan, and P. McLoughlin, "Determination of hydrocarbons using sapphire fibers coated with poly(dimethylsiloxane)," *Applied Spectroscopy*, vol. 57, no. 4, pp. 400–6, 2003.

[64] G. Dakroub, T. Duguet, C. Lacaze-Dufaure, S. Roualdes, A. van der Lee, D. Rebiscoul, and V. Rouessac, "Plasma polymerized organosilicon thin films for volatile organic compound (VOC) detection," *Plasma*, vol. 6, no. 3, pp. 563–576, 2023.

[65] Y.-M. Sun and J. Chen, "Sorption/desorption properties of ethanol, toluene, and xylene in poly(dimethylsiloxane) membranes," *Journal of Applied Polymer Science*, vol. 51, no. 10, pp. 1797–1804, 1994.

[66] S. Sato, M. Suzuki, S. Kanehashi, and K. Nagai, "Permeability, diffusivity, and solubility of benzene vapor and water vapor in high free volume silicon- or fluorine-containing polymer membranes," *Journal of Membrane Science*, vol. 360, no. 1, pp. 352–362, 2010.

[67] K.-S. Oh, Y.-M. Koo, and K.-W. Jung, "Characterization of a sheet membrane interface for sample introduction into a time-of-flight mass spectrometer," *International Journal of Mass Spectrometry*, vol. 253, no. 1, pp. 65–70, 2006.

[68] S. A. Maier, *Plasmonics: Fundamentals and Applications: Fundamentals and Applications*. New York: Springer Science + Business Media, 1. aufl. ed., 2007.

[69] C. Genet and T. W. Ebbesen, "Light in tiny holes," *Nature*, vol. 445, no. 7123, pp. 39–46, 2007.

[70] A. González-López, J. Gomez-Cruz, G. Ascanio, and C. Escobedo, "Cost-effective piezoresistive-based sensor for evaluating thin polymeric membranes on au metallic surfaces," *IEEE Sensors Journal*, vol. 25, no. 13, pp. 23685–23691, 2025.

[71] P. V. Lambeck, "Integrated optical sensors for the chemical domain," *Measurement Science and Technology*, vol. 17, no. 8, pp. R93–R116, 2006.

[72] R. Niemeier and J. D. Rogers, "Low-cost reflective Hilger-Chance refractometer used to determine Sellmeier coefficients of bulk polydimethylsiloxane," *Applied Optics*, vol. 58, no. 22, pp. 6152–6156, 2019.

[73] K. Luke, Y. Okawachi, M. R. E. Lamont, A. L. Gaeta, and M. Lipson, "Broadband mid-infrared frequency comb generation in a si_3n_4 microresonator," *Optics Letters*, vol. 40, no. 21, pp. 4823–4826, 2015.

[74] M. N. Polyanskiy, "Refractiveindex.info database of optical constants," *Scientific Data*, vol. 11, no. 1, p. 94, 2024.

[75] A. D. Rakić, A. B. Djurišić, J. M. Elazar, and M. L. Majewski, "Optical properties of metallic films for vertical-cavity optoelectronic devices," *Applied Optics*, vol. 37, no. 22, pp. 5271–5283, 1998.

[76] M. Newville, R. Otten, A. Nelson, T. Stensitzki, A. Ingargiola, D. Allan, A. Fox, F. Carter, and M. Rawlik, *LMFIT: Non-Linear Least-Squares Minimization and Curve-Fitting for Python*. Zenodo, 2016.

[77] Y.-M. Sun and J. Chen, "Sorption/desorption properties of ethanol, toluene, and xylene in poly(dimethylsiloxane) membranes," *Journal of Applied Polymer Science*, vol. 51, no. 10, pp. 1797–1804, 1994.

[78] E. Boscaini, M. L. Alexander, P. Prazeller, and T. D. Märk, "Investigation of fundamental physical properties of a polydimethylsiloxane (PDMS) membrane using a proton transfer reaction mass spectrometer (PTRMS)," *International journal of mass spectrometry*, vol. 239, no. 2, pp. 179–186, 2004.

[79] S. Chen, J. Wang, C. Zhang, M. Li, N. Li, H. Wu, Y. Liu, W. Peng, and Y. Song, "Marine structural health monitoring with optical fiber sensors: A review," *Sensors*, vol. 23, no. 4, p. 1877, 2023.

[80] J. K. Sahota, N. Gupta, and D. Dhawan, "Fiber Bragg grating sensors for monitoring of physical parameters: a comprehensive review," *Optical engineering*, vol. 59, no. 6, p. 1, 2020.

[81] C. E. Campanella, A. Cuccovillo, C. Campanella, A. Yurt, and V. M. N. Passaro, "Fibre Bragg grating based strain sensors: Review of technology and applications," *Sensors*, vol. 18, no. 9, p. 3115, 2018.

[82] G. Gagliardi, M. Salza, S. Avino, P. Ferraro, and P. De Natale, "Probing the ultimate limit of fiber-optic strain sensing," *Science*, vol. 330, no. 6007, pp. 1081–1084, 2010.

[83] P. Liu, W. Huang, W. Zhang, and F. Li, "Ultrahigh resolution optic fiber strain sensor with a frequency-locked random distributed feedback fiber laser," *Optics letters*, vol. 43, no. 11, p. 2499, 2018.

[84] N. Ballard, D. Paz-Soldan, P. Kung, and H.-P. Loock, "Musical instrument recordings made with a fiber Fabry-Perot cavity: photonic guitar pickup," *Applied Optics*, vol. 49, no. 11, p. 2198, 2010.

[85] S. Avino, J. A. Barnes, G. Gagliardi, X. Gu, D. Gutstein, J. R. Mester, C. Nicholaou, and H.-P. Loock, "Musical instrument pickup based on a laser locked to an optical fiber resonator," *Optics express*, vol. 19, no. 25, p. 25057, 2011.

[86] G. Wild and S. Hinckley, "Acousto-ultrasonic optical fiber sensors: Overview and state-of-the-art," *IEEE sensors journal*, vol. 8, no. 7, pp. 1184–1193, 2008.

[87] K. Yüksel, D. Kinet, V. Moeyaert, G. Kouroussis, and C. Caucheteur, "Railway monitoring system using optical fiber grating accelerometers," *Smart materials and structures*, vol. 27, no. 10, p. 105033, 2018.

[88] N. J. Lindsey and E. R. Martin, "Fiber-optic seismology," *Annual review of earth and planetary sciences*, vol. 49, no. 1, pp. 309–336, 2021.

[89] Q. Bai, Q. Wang, D. Wang, Y. Wang, Y. Gao, H. Zhang, M. Zhang, and B. Jin, "Recent advances in Brillouin optical time domain reflectometry," *Sensors*, vol. 19, no. 8, p. 1862, 2019.

[90] L. Chamoin, S. Farahbakhsh, and M. Poncelet, "An educational review on distributed optic fiber sensing based on Rayleigh backscattering for damage tracking and structural health monitoring," *Measurement science & technology*, vol. 33, no. 12, p. 124008, 2022.

[91] Z. He and Q. Liu, "Optical fiber distributed acoustic sensors: A review," *Journal of Lightwave Technology*, vol. 39, no. 12, pp. 3671–3686, 2021.

[92] X. Bao and L. Chen, "Recent progress in distributed fiber optic sensors," *Sensors*, vol. 12, pp. 8601–8639, 2012.

[93] M. K. Barnoski and S. M. Jensen, "Fiber waveguides: a novel technique for investigating attenuation characteristics," *Applied Optics*, vol. 15, no. 9, pp. 2112–2115, 1976.

[94] W. Eickhoff and R. Ulrich, "Optical frequency domain reflectometry in single-mode fiber," *Applied Physics Letters*, vol. 39, no. 9, pp. 693–695, 1981.

[95] C. A. Galindez-Jamioy and J. M. López-Higuera, "Brillouin distributed fiber sensors: An overview and applications," *Journal of Sensors*, vol. 2012, p. 204121, 2012.

[96] W. Huang, W. Zhang, L. Li, H. Zhang, and F. Li, "Review on low-noise broadband fiber optic seismic sensor and its applications," *Journal of Lightwave Technology*, vol. 41, no. 13, pp. 4153–4163, 2023.

[97] P. Lu, N. Lalam, M. Badar, B. Liu, B. T. Chorpening, M. P. Buric, and P. R. Ohodnicki, "Distributed optical fiber sensing: Review and perspective," *Applied Physics Reviews*, vol. 6, no. 4, 2019.

[98] W. Blanc, L. Schenato, C. Molardi, L. Palmieri, A. Galtarossa, and D. Tosi, "Distributed fiber optics strain sensors: from long to short distance," *Comptes rendus. Geoscience*, vol. 354, no. S1, pp. 161–183, 2022.

[99] J. Pastor-Graells, H. F. Martins, A. Garcia-Ruiz, S. Martin-Lopez, and M. Gonzalez-Herraez, "Single-shot distributed temperature and strain tracking using direct detection phase-sensitive otdr with chirped pulses," *Optics express*, vol. 24, no. 12, p. 13121, 2016.

[100] Z. Wang, L. Zhang, S. Wang, N. Xue, F. Peng, M. Fan, W. Sun, X. Qian, J. Rao, and Y. Rao, "Coherent ϕ-OTDR based on I/Q demodulation and homodyne detection," *Optics express*, vol. 24, no. 2, pp. 853–858, 2016.

[101] C. Fan, H. Li, K. Zhang, H. Liu, Y. Sun, H. Liu, B. Yan, Z. Yan, D. Liu, P. P. Shum, and Q. Sun, "300 km ultralong fiber optic DAS system based on optimally designed bidirectional EDFA relays," *Photonics Research*, vol. 11, pp. 968–977, Jun 2023.

[102] J. Guo and C. Yang, "Highly stabilized phase-shifted fiber Bragg grating sensing system for ultrasonic detection," *IEEE Photonics Technology Letters*, vol. 27, no. 8, pp. 848–851, 2015.

[103] C. E. Campanella, A. Giorgini, S. Avino, P. Malara, R. Zullo, G. Gagliardi, and P. De Natale, "Localized strain sensing with fiber Bragg-grating ring cavities," *Optics Express*, vol. 21, no. 24, pp. 29435–41, 2013.

[104] P. Malara, L. Mastronardi, C. E. Campanella, A. Giorgini, S. Avino, V. M. Passaro, and G. Gagliardi, "Split-mode fiber Bragg grating sensor for high-resolution static strain measurements," *Optics Letters*, vol. 39, no. 24, pp. 6899–902, 2014.

[105] Z. Donghui, S. Xuewen, Z. Lin, and I. Bennion, "A novel sensor interrogation technique using chirped fiber grating based Sagnac loop," *Sensors*, vol. 2, pp. 1351–1353 vol.2, 2002.

[106] T. A. Berkoff and A. D. Kersey, "Fiber Bragg grating array sensor system using a bandpass wavelength division multiplexer and interferometric detection," *IEEE Photonics Technology Letters*, vol. 8, no. 11, pp. 1522–1524, 1996.

[107] M. A. Davis and A. D. Kersey, "Application of a fiber Fourier transform spectrometer to the detection of wavelength-encoded signals from Bragg grating sensors," *Journal of Lightwave Technology*, vol. 13, no. 7, pp. 1289–1295, 1995.

[108] R. W. P. Drever, J. L. Hall, F. V. Kowalski, J. Hough, G. M. Ford, A. J. Munley, and H. Ward, "Laser phase and frequency stabilization using an optical resonator," *Applied Physics B*, vol. 31, no. 2, pp. 97–105, 1983.

[109] A. Abramovici, W. E. Althouse, R. W. P. Drever, Y. Gürsel, S. Kawamura, F. J. Raab, D. Shoemaker, L. Sievers, R. E. Spero, K. S. Thorne, R. E. Vogt, R. Weiss, S. E. Whitcomb, and M. E. Zucker, "LIGO: The laser interferometer gravitational-wave observatory," *Science*, vol. 256, no. 5055, pp. 325–333, 1992.

[110] A. Schenzle, R. G. DeVoe, and R. G. Brewer, "Phase-modulation laser spectroscopy," *Physical Review A*, vol. 25, no. 5, pp. 2606–2621, 1982.

[111] E. D. Black, "An introduction to Pound–Drever–Hall laser frequency stabilization," *American Journal of Physics*, vol. 69, no. 1, pp. 79–87, 2001.

[112] Q. Liu, T. Tokunaga, and Z. He, "Sub-nano resolution fiber-optic static strain sensor using a sideband interrogation technique," *Optics Letters*, vol. 37, no. 3, pp. 434–6, 2012.

[113] S. Zhao, Q. Liu, J. Chen, and Z. He, "Pico-strain resolution multiplexed fiber grating sensor array interrogated with mode-locked laser," *Journal of Lightwave Technology*, vol. 37, no. 18, pp. 4838–4843, 2019.

[114] Q. Liu, M. Wu, J. Chen, and Z. He, "Coherent Pound–Drever–Hall technique for high resolution fiber-optic sensors at low probe power," *Journal of Lightwave Technology*, vol. 36, no. 4, pp. 1026–1031, 2018.

[115] M. Wu, Q. Liu, J. Chen, Z. He, Y. Chung, J. Canning, L. Yuan, W. Jin, B. Lee, and K. Nakamura, "Coherent Pound-Drever-Hall technique for high resolution fiber optic strain sensor at very low light power," vol. 10323, pp. 103230V–103230V–4, SPIE, 2017.

[116] J. Barnes, S. Li, A. Goyal, P. Abolmaesumi, P. Mousavi, and H.-P. Loock, "Broadband vibration detection in tissue phantoms using a fiber Fabry-Perot cavity," *IEEE Transactions on Biomedical Engineering*, vol. 65, no. 4, pp. 921–927, 2018.

[117] J. H. Chow, D. E. McClelland, M. B. Gray, and I. C. Littler, "Demonstration of a passive subpicostrain fiber strain sensor," *Optics Letters*, vol. 30, no. 15, pp. 1923–5, 2005.

[118] J. Chen, Q. Liu, X. Fan, and Z. He, "Ultrahigh resolution optical fiber strain sensor using dual Pound–Drever–Hall feedback loops," *Optics letters*, vol. 41, no. 5, pp. 1066–1069, 2016.

[119] W. Huang, W. Zhang, T. Zhen, F. Zhang, and F. Li, "π-phase-shifted FBG for high-resolution static-strain measurement based on wavelet threshold denoising algorithm," *Journal of Lightwave Technology*, vol. 32, no. 22, pp. 4294–4300, 2014.

[120] D. Aydin, *Sensing and Emission in Optical Cavities*. Thesis, 2021.

[121] S. P. Neumann, A. Buchner, L. Bulla, M. Bohmann, and R. Ursin, "Continuous entanglement distribution over a transnational 248 km fiber link," *Nature communications*, vol. 13, no. 1, pp. 6134–8, 2022.

[122] Y.-G. Han, T. V. A. Tran, S.-H. Kim, and S. B. Lee, "Multiwavelength Raman-fiber-laser-based long-distance remote sensor for simultaneous measurement of strain and temperature," *Optics Letters*, vol. 30, no. 11, pp. 1282–1284, 2005.

[123] H. Y. Fu, H. L. Liu, W. H. Chung, and H. Y. Tam, "A novel fiber Bragg grating sensor configuration for long-distance quasi-distributed measurement," *IEEE Sensors Journal*, vol. 8, no. 9, pp. 1598–1602, 2008.

[124] Y. C. Manie, R.-K. Shiu, P.-C. Peng, B.-Y. Guo, M. A. Bitew, W.-C. Tang, and H.-K. Lu, "Intensity and wavelength division multiplexing FBG sensor system using a Raman amplifier and extreme learning machine," *Journal of Sensors*, vol. 2018, no. 1, p. 7323149, 2018.

[125] J. Hu, Z. Chen, X. Yang, J. Ng, and C. Yu, "100-km long distance fiber Bragg grating sensor system based on Erbium-doped fiber and Raman amplification," *IEEE Photonics Technology Letters*, vol. 22, no. 19, pp. 1422–1424, 2010.

[126] S. B. Foster, G. A. Cranch, J. Harrison, A. E. Tikhomirov, and G. A. Miller, "Distributed feedback fiber laser strain sensor technology," *Journal of Lightwave Technology*, vol. 35, no. 16, pp. 3514–3530, 2017.

[127] S. Foster, A. Tikhomirov, J. Harrison, J. van Velzen, H. J. Kalinowski, J. L. Fabris, and W. J. Bock, "Demonstration of an advanced fibre laser hydrophone array in Gulf St Vincent," vol. 9634, pp. 96342F–96342F–4, SPIE, 2015.

[128] X. Roselló-Mechó, M. Delgado-Pinar, A. Díez, and M. V. Andrés, "Measurement of Pockels' coefficients and demonstration of the anisotropy of the elasto-optic effect in optical fibers under axial strain," *Optics Letters*, vol. 41, no. 13, pp. 2934–2937, 2016.

[129] F. El-Diasty, "Multiple-beam interferometric determination of Poisson's ratio and strain distribution profiles along the cross section of bent single-mode optical fibers," *Applied Optics*, vol. 39, no. 19, pp. 3197–3201, 2000.

[130] H.-P. Loock and P. D. Wentzell, "Detection limits of chemical sensors: Applications and misapplications," *Sensors and Actuators B: Chemical*, vol. 173, pp. 157–163, 2012.

[131] ONC, "Humpback song with dolphin calls," 2013.

[132] P. Werle, R. Mücke, and F. Slemr, "The limits of signal averaging in atmospheric trace-gas monitoring by tunable diode-laser absorption spectroscopy (TDLAS)," *Applied Physics B*, vol. 57, no. 2, pp. 131–139, 1993.

[133] N. El-Sheimy, H. Hou, and X. Niu, "Analysis and modeling of inertial sensors using Allan variance," *IEEE Transactions on Instrumentation and Measurement*, vol. 57, no. 1, pp. 140–149, 2008.

[134] J. Chow, J. Cumpston, I. Little, D. McClelland, and M. Gray, "Interrogation of a fiber Fabry-Perot sensor by current modulation of a diode laser," *ed: arXiv*, 2004.

[135] T. J. Hofler and S. L. Garrett, "Thermal noise in a fiber optic sensor," *The Journal of the Acoustical Society of America*, vol. 84, no. 2, pp. 471–475, 1988.

[136] J. H. Chow, T. T. Y. Lam, I. C. M. Littler, D. E. McClelland, and M. B. Gray, "Shot noise limited fiber laser source for sensing applications," vol. 7004, pp. 70041C–70041C–4, SPIE, 2008.

[137] J. E. Kadum, C. Feng, and T. Schneider, "Characterization of the noise induced by stimulated Brillouin scattering in distributed sensing," *Sensors*, vol. 20, no. 15, p. 4311, 2020.

[138] A. Kobyakov, M. Sauer, and D. Chowdhury, "Stimulated Brillouin scattering in optical fibers," *Advances in Optics and Photonics*, vol. 2, no. 1, pp. 1–59, 2010.

[139] J. Barnes, M. Dreher, K. Plett, R. S. Brown, C. M. Crudden, and H.-P. Loock, "Chemical sensor based on a long-period fibre grating modified by a functionalized polydimethylsiloxane coating," *Analyst*, vol. 133, pp. 1541–1549, 2008.

[140] R. Swanepoel, "Determination of the thickness and optical constants of amorphous silicon," *Journal of physics. E, Scientific instruments*, vol. 16, no. 12, pp. 1214–1222, 1983.

[141] N. E. Sánchez-Arriaga, D. Tiwari, W. Hutabarat, A. Leyland, and A. Tiwari, "A spectroscopic reflectance-based low-cost thickness measurement system for thin films: Development and testing," *Sensors*, vol. 23, no. 11, 2023.

[142] R. F. Balderas-Valadez and C. Pacholski, "Plasmonic nanohole arrays on top of porous silicon sensors: A win–win situation," *ACS Applied Materials & Interfaces*, vol. 13, no. 30, pp. 36436–36444, 2021.

[143] L. Tu, L. Huang, and W. Wang, "A novel micromachined Fabry-Perot interferometer integrating nano-holes and dielectrophoresis for enhanced biochemical sensing," *Biosensors & Bioelectronics*, vol. 127, pp. 19–24, 2019.

[144] R. F. W. Coates, *Underwater acoustic systems*. Macmillan new electronics series, London: Macmillan, 1990.

[145] Z. Meng, W. Chen, J. Wang, X. Hu, M. Chen, and Y. Zhang, "Recent progress in fiber-optic hydrophones," *Photonic Sensors*, vol. 11, no. 1, pp. 109–122, 2021.

[146] F. A. Bruno, M. Janneh, A. Gunda, R. Kyselica, P. Stajanca, S. Werzinger, G. Gruca, N. Rijnveld, G. V. Persiano, A. Cutolo, M. Pisco, and A. Cusano, "Fiber optic hydrophones for towed array applications," *Optics and Lasers in Engineering*, vol. 160, p. 107269, 2023.

[147] M. Janneh, F. A. Bruno, S. Guardato, G. P. Donnarumma, G. Iannaccone, G. Gruca, S. Werzinger, A. Gunda, N. Rijnveld, A. Cutolo, M. Pisco, and A. Cusano, "Fiber optic hydrophones for geophysical and volcanological monitoring," in *27th International Conference on Optical Fiber Sensors*, Technical Digest Series, p. W4.6, Optica Publishing Group, 2022.

[148] A. Arora, A. N. Zawada, M. Bernier, and M. J. F. Digonnet, "High-resolution slow-light fiber-Bragg-grating microphone and hydrophone," *IEEE Sensors Journal*, vol. 23, no. 8, pp. 8391–8399, 2023.

[149] K. E. Jenne, D. Huang, and T. R. Howarth, "Acoustic cymbal performance under hydrostatic pressure," *The Journal of the Acoustical Society of America*, vol. 115, no. 5, pp. 2621–2621, 2004.

[150] A. L. Buck, "Effects of the atmosphere on laser beam propagation," *Applied Optics*, vol. 6, no. 4, pp. 703–8, 1967.

Appendix A

Chapter 2 appendices

A.1 Matlab code for diffusion equations

Contents


```
% The matlab functions that describe the diffusion kinetics are separated
% into the cases for an impermeable and permeable film. In each of those
% cases, functions are provided for concentration gradients (as a function
% of y and t), integration concentrations (as a function of time) for a
% plasmonic interaction near the interface and over the entire film for the
% absorption and desorption processes.
```

PARAMETERS

```
% X1 (float): Analyte concentration
% D (float): Diffusion constant, in units of cm^2/s
% d (float): Thickness of membrane, in units of cm
% dy (float): Height of evanescent wave interaction, in units of cm
% t (array of float/int): Time, in units of s
% y (array of float/int): Height, in units of cm
% num_terms (int): Number of terms to sum over

num_terms = 50;
```

********** IMPERMEABLE FILM **********

Concentration gradients for absorption and desorption

Concentration gradient across impermeable membrane during absorption

```
function f=Imp_Abs_conc(X1,D,d,t,y)
    i=0;
    Terms(num_terms:length(y))=zeros;
        for j=0:num_terms
        i=i+1;
            Terms(i,:)=(-1)^j/(2*j+1)*cos((2*j+1)*pi*y/(2*d))*exp(-D.*(2*j+1)^2*pi^2*t/(4*d^2));
        end
    SumofTerms=sum(Terms);
    f=X1*(1-4/pi*SumofTerms);
end

% Concentration gradient across impermeable membrane during
% desorption
```

```
function f=Imp_Des_conc(X1,D,d,t,y)
    i=0;
    Terms(num_terms:length(y))=zeros;
        for j=0:num_terms
        i=i+1;
            Terms(i,:)=(-1)^j/(2*j+1)*cos((2*j+1)*pi*y/(2*d))*exp(-D.*(2*j+1)^2*pi^2*t/(4*d^2));
        end
    SumofTerms=sum(Terms);
    f=X1*(4/pi*SumofTerms);
end
```

Absorption and desorption processes through evanescent wave

```
% Integrated concentration through evanescent wave during
% absorption as a function of time
function f=Imp_Abs_ev(X1,D,d,t,dy)
    i=0;
    Terms(num_terms:length(t))=zeros;
        for j=0:num_terms
        i=i+1;
            Terms(i,:)= (-1)^j/(2*j+1)^2*sin((2*j+1)*pi*dy/(2*d))*exp(-D.*(2*j+1)^2*pi^2*t/(4*d.^2));
        end
    SumofTerms=sum(Terms);
    f=X1*(1-8*d/(pi^2*dy)*SumofTerms);
end

% Integrated concentration through evanescent wave during
% desorption as a function of time
function f=Imp_Des_ev(X1,D,d,t,dy)
    i=0;
    Terms(num_terms:length(t))=zeros;
        for j=0:num_terms
        i=i+1;
            Terms(i,:)= (-1)^j/(2*j+1)^2*sin((2*j+1)*pi*dy/(2*d))*exp(-D.*(2*j+1)^2*pi^2*t/(4*d.^2));
        end
    SumofTerms=sum(Terms);
    f=X1*(8*d/(pi^2*dy)*SumofTerms);
end
```

Absorption and desorption processes integrated over film

```
% Integrated concentration in film during absorption as a
% function of time
function f=Imp_Abs_film(X1,D,d,t)
    i=0;
    Terms(num_terms:length(t))=zeros;
        for j=0:num_terms
        i=i+1;
            Terms(i,:)= 1/(2*j+1)^2*exp(-D.*(2*j+1)^2*pi^2*t/(4*d.^2));
        end
    SumofTerms=sum(Terms);
    f=X1*(1-8/pi^2*SumofTerms);
end

% Integrated concentration in film during desorption as a
```

```
% function of time
function f=Imp_Des_film(X1,D,d,t)
    i=0;
    Terms(num_terms:length(t))=zeros;
        for j=0:num_terms
        i=i+1;
            Terms(i,:)= 1/(2*j+1)^2*exp(-D.*(2*j+1)^2*pi^2*t/(4*d.^2));
        end
    SumofTerms=sum(Terms);
    f=X1*(8/pi^2*SumofTerms);
end
```

********** PERMEABLE FILM **********

Concentration gradients for absorption and desorption

Concentration gradient across permeable membrane during absorption

```
function f=Per_Abs_conc(X1,D,d,t,y)
    i=0;
    Terms(num_terms:length(y))=zeros;
        for j=1:num_terms
        i=i+1;
            Terms(i,:)=(-1)^j/j*sin(j*pi*y/d)*exp(-D.*j^2*pi^2*t/(d^2));
        end
    SumofTerms=sum(Terms);
    f=X1*(y/100+2/pi*SumofTerms);
    %f=X1*(2/pi*SumofTerms);
end

% Concentration gradient across permeable membrane during
% desorption assuming linear concentration gradient
function f=Per_Des_conc_grad(X1,D,d,t,y)
    i=0;
    Terms(num_terms:length(y))=zeros;
        for j=1:num_terms
        i=i+1;
            Terms(i,:)=(-1)^j/(j)*sin(j*pi*y/d)*exp(-D.*j^2*pi^2*t/(d^2));
        end
    SumofTerms=sum(Terms);
    f=-X1*(2/pi*SumofTerms);
    %f=X1*(2/pi*SumofTerms);
end

% Concentration gradient across permeable membrane during
% desorption assuming constant initial concentration
function f=Per_Des_conc_const(X1,D,d,t,y)
    i=0;
    Terms(num_terms:length(y))=zeros;
        for j=0:num_terms
        i=i+1;
            Terms(i,:)=1/(2*j+1)*sin((2*j+1)*pi*y/d)*exp(-D.*(2*j+1)^2*pi^2*t/(d^2));
        end
    SumofTerms=sum(Terms);
    f=X1*(4/pi*SumofTerms);
    %f=X1*(2/pi*SumofTerms);
end
```

Absorption and desorption processes through evanescent wave

Integrated concentration through evanescent wave during absorption as a function of time

```
function f=Per_Abs_ev(X1,D,d,t,dy)
    i=0;
    Terms(num_terms:length(t))=zeros;
        for j=1:num_terms
        i=i+1;
            Terms(i,:)=(-1)^j/j^2*(cos(j*pi*dy/d)-1)*exp(-D.*j^2*pi^2*t/d^2);
        end
    SumofTerms=sum(Terms);
    f=X1*(dy/(d*2)-2*d/(dy*pi^2)*SumofTerms);
end

% Integrated concentration through evanescent wave during
% desorption assuming constant initial concentration as a function of time
function f=Per_Des_ev_const(X1,D,d,t,dy)
    i=0;
    Terms(num_terms:length(t))=zeros;
        for j=0:num_terms
        i=i+1;
            Terms(i,:)=1/(2*j+1)^2*(1-cos((2*j+1)*pi*dy/d))*exp(-D.*(2*j+1)^2*pi^2*t/d^2);
        end
    SumofTerms=sum(Terms);
    f=X1*(4*d/(dy*pi^2)*SumofTerms);
end

% Integrated concentration through evanescent wave during
% desorption assuming linear concentration gradient as a function of time
function f=Per_Des_ev_grad(X1,D,d,t,dy)
    i=0;
    Terms(num_terms:length(t))=zeros;
        for j=1:num_terms
        i=i+1;
            Terms(i,:)=(-1)^j/j^2*(cos(j*pi*dy/d)-1)*exp(-D.*j^2*pi^2*t/d^2);
        end
    SumofTerms=sum(Terms);
    f=X1*(2*d/(dy*pi^2)*SumofTerms);
end
```

Absorption and desorption processes integrated over film

```
% Integrated concentration over film during absorption as a
% function of time
function f=Per_Abs_film(X1,D,d,t)
    i=0;
    Terms(num_terms:length(t))=zeros;
        for j=0:num_terms
        i=i+1;
            Terms(i,:)=1/(2*j+1)^2*exp(-D.*(2*j+1)^2*pi^2*t/d^2);
        end
    SumofTerms=sum(Terms);
    f=X1*(1/2-4/pi^2*SumofTerms);
end
```

```
% Integrated concentration over film during desorption
% assuming constant initial concentration as a function of time
function f=Per_Des_film_const(X1,D,d,t)
    i=0;
    Terms(num_terms:length(t))=zeros;
        for j=0:num_terms
        i=i+1;
            Terms(i,:)=1/(2*j+1)^2*exp(-D.*(2*j+1)^2*pi^2*t/d^2);
        end
    SumofTerms=sum(Terms);
    f=X1*(8/(pi^2)*SumofTerms);
end

% Integrated concentration over film during desorption
% assuming linear concentration gradient as a function of time
function f=Per_des_film_grad(X1,D,d,t)
    i=0;
    Terms(num_terms:length(t))=zeros;
        for j=0:num_terms
        i=i+1;
            Terms(i,:)=1/(2*j+1)^2*exp(-D.*(2*j+1)^2*pi^2*t/d^2);
        end
    SumofTerms=sum(Terms);
    f=X1*(4/(pi^2)*SumofTerms);
end
```

Published with MATLAB® R2022b

Appendix B

Chapter 3 appendices

B.1 Sequential diffusion fitting

For the modeling of the diffusion constants of o-xylene into PDMS, we had assumed that two processes begin immediately upon exposure of the PDMS film to the VOC environment. Upon inspection of the sorption curves, we do observe a flat region between the curves, which may indicative of a sequential diffusion process. This delay could, in principle, correspond to a physical process where the swelling upon initial exposure of VOC changes the diffusion kinetics. However, the introduction of this parameter also increases the flexibility of the model, which carries the risk of overfitting experimental noise or system artifacts.

To test the performance of these two approaches, the sorption data was fit with an additional fitting parameter, t_0, to allow for one of the sorption processes to start a certain time after the first process. The two models were evaluated using the root mean square error (RMSE) and mean absolute error (MAE), which quantify the average deviation of the model from the experimental absorption–desorption curves. RMSE emphasizes larger deviations, while MAE provides a measure of the typical error magnitude. Table B.1 summarizes the RMSE and MAE calculated for the absorption and desorption process with both model, and the percentage improvement (implying a reduction in RMSE and MAE) we observe when using the sequential model. The sequential fits showed a 5 % improvement in error during the absorption of VOCs into PDMS and a 3 improvement during desorption. These modest reductions suggest that, although the sequential model can marginally improve numerical agreement, the physical significance of this improvement is limited.

Upon visual inspection of the respective fits, we can gain further insights into the difference of the two fit . For the higher concentration runs, the sequential model clearly produces a closer match to the experimental absorption profile as it better able to capture the inflection point of the second absorption process (Figures B.1a and B.1b). However, in

Parameter	Absorption	Desorption
RMSE (conc.)	1.35 x 10^{-4}	1.22 x 10^{-4}
RMSE (seq.)	1.28 x 10^{-4}	1.17 x 10^{-4}
Percentage Difference (RMSE)	4.5 %	2.5 %
MAE (conc.)	1.08 x 10^{-4}	0.96 x 10^{-4}
MAE (seq.)	1.01 x 10^{-4}	0.93 x 10^{-4}
Percentage Difference (MAE)	5.1 %	3.2 %

Table B.1: Comparison of concurrent and sequential diffusion models for absorption and desorption stages through RMSE and MAE metrics.

most practical datasets the sequential fits begin to track small fluctuations or experimental artifacts after the initial uptake or release stage (Figures B.1c and B.1e). This indicates that the time-delay parameter is compensating for noise rather than capturing a genuine transport mechanism. Consequently, while the sequential approach provides a better fit, the concurrent model remains the more physically consistent description of VOC diffusion into PDMS for the majority of cases examined in this study.

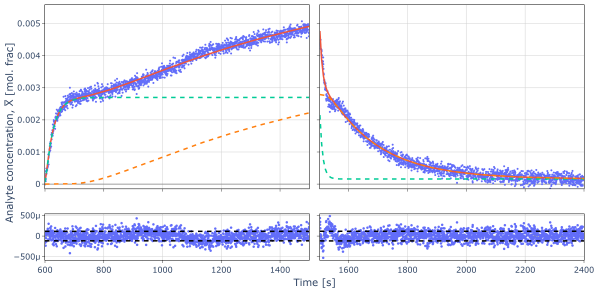

(a) 10 μL/min concurrent fit

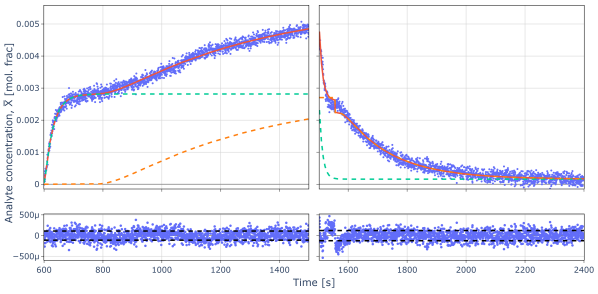

(b) 10 μL/min sequential fit

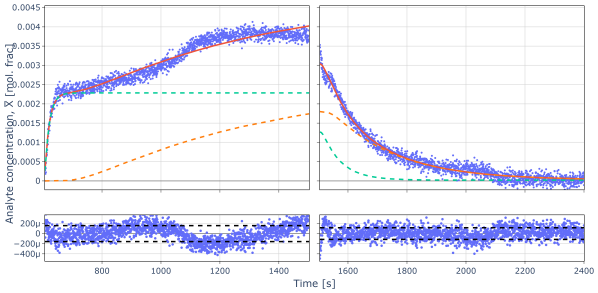

(c) 6 μL/min concurrent fit

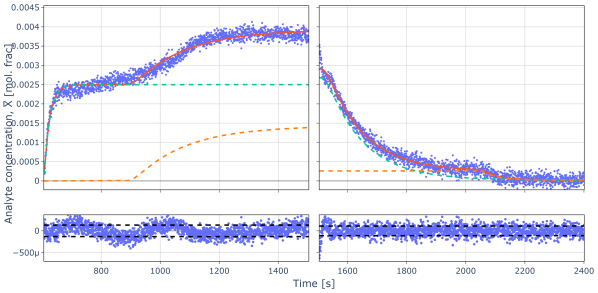

(d) 6 μL/min sequential fit

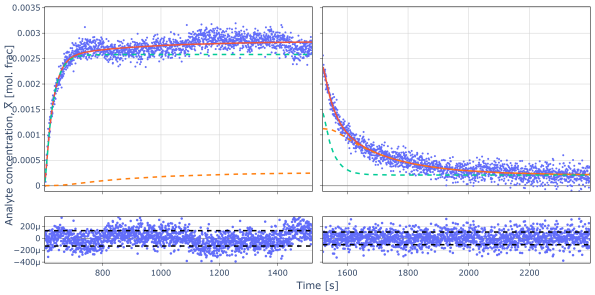

(e) 4 μL/min concurrent fit

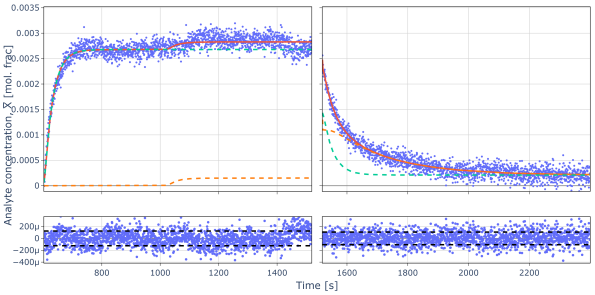

(f) 4 μL/min sequential fit

Figure B.1: Comparison of concurrent and sequential fits

B.2 Python code for analysis and fitting

```
## Import libraries
import numpy as np
import pandas as pd
import matplotlib.pyplot as plt
from mpl_toolkits.mplot3d import Axes3D
from scipy import signal, stats
from scipy.stats import sem
from scipy.optimize import curve_fit, least_squares, leastsq, differential_evolution
from lmfit import minimize, Parameters, fit_report, Model
import datetime

import plotly.express as px
import plotly.graph_objects as go
from plotly.subplots import make_subplots
import kaleido


### Diffusion models (Supported and Freestanding)

def fsm(t, X0, X1, X2, D, y1, y2, t0, phase, d = 8e-4):
    t1 = X1
    t2 = ((X2-X1)*(y2**2 - y1**2))/((y2-y1)*(2*d))
    t3 = 2*d/((y2-y1)*np.pi**2)
    t4 = (4*d*X0)/((y2-y1)*np.pi**2)
    num_terms = 200

    sum_fsm = 0
    sum_init = 0

    t_shift = np.array(t - t0) + 5
    # t_shift[t_shift < 0] = float('nan')
    t_shift[t_shift < 5] = 0

    for n in range(1, num_terms):
        m = n-1
        sum_fsm += ((X2*(-1)**n-X1)/n**2)*(np.cos(n*np.pi*y2/d) - np.cos(n*np.pi*y1/d))*(np.exp(-(D*n**2*np.pi**2*t_shift)/d**2))
        sum_init += (1/(2*m+1)**2)*(np.cos((2*m+1)*np.pi*y2/d) - np.cos((2*m+1)*np.pi*y1/d))*(np.exp(-(D*(2*m+1)**2*np.pi**2*t_shift)/(d**2)))

    if phase == 'abs':
        return t1 + t2 - t3*sum_fsm - t4*sum_init
    elif phase == 'des':
        return -t4*sum_init
    elif phase == 'des (old)':
        return -t3*sum_fsm

def sm(t, X, D, y1, y2, t0, phase, d = 8e-4):
    t1 = 1
    t2 = (8*d)/((y2-y1)*np.pi**2)
    num_terms = 200

    sum_sm = 0

    t_shift = np.array(t - t0) + 5
    # t_shift[t_shift < 0] = float('nan')
    t_shift[t_shift < 5] = 0

    for n in range(num_terms):
        sum_sm += ((-1)**n/(2*n+1)**2)*np.exp(-((D*np.pi**2*(2*n+1)**2*(t_shift))/(4*d**2)))*(np.sin(((2*n+1)*np.pi*y2)/(2*d)) - np.sin(((2*n+1)*np.pi*y1)/(2*d

    if phase == 'abs':
        return X*(t1-t2*sum_sm)
    elif phase == 'des':
        return X*t2*sum_sm

## Diffusion equation for special case of nanohole array

def fit_sing_abs(t, x_1, d_1, t0, o, d, dy = 1e-5):
    phase = 'abs'
    # Frational area calculation of support and free standing membrane
    A_tot = 450*450
    num_holes = 1125*1125
    A_holes = np.pi*0.1**2*num_holes

    # Area of free-standing membrane
    a_fsm = A_holes/A_tot
    # a_fsm = 0.5
    # Area of supported membrane
    a_sm = 1-a_fsm

    return a_fsm*fsm(t, 0, 0, x_1, d_1, 0, dy, t0, phase, d = d) + a_sm*sm(t, x_1, d_1, 0, dy, t0, phase, d = d) + o

def fit_dbl_abs(t, x_1, x_2, d_1, d_2, t0, t1, o, d, dy = 1e-5):
    phase = 'abs'
    # Frational area calculation of support and free standing membrane
    A_tot = 450*450
    num_holes = 1125*1125
    A_holes = np.pi*0.1**2*num_holes
    a_fsm = A_holes/A_tot
    # a_fsm = 0.5
    a_sm = 1-a_fsm

    return a_fsm*(fsm(t, 0, 0, x_1, d_1, 0, dy, t0, phase, d = d) + fsm(t, 0, 0, x_2, d_2, 0, dy, t1, phase, d = d)) + a_sm*(sm(t, x_1, d_1, 0, dy, t0, phase, 

def fit_sing_des(t, x_1, d_1, t0, o, d, dy = 1e-5):
    phase = 'des'
    # Frational area calculation of support and free standing membrane
    A_tot = 450*450
    num_holes = 1125*1125
    A_holes = np.pi*0.1**2*num_holes
    a_fsm = A_holes/A_tot
    # a_fsm = 0.5
    a_sm = 1-a_fsm

    return a_fsm*fsm(t, x_1, 0, 0, d_1, 0, dy, t0, phase, d = d) + a_sm*sm(t, x_1, d_1, 0, dy, t0, phase, d = d) + o

def fit_dbl_des(t, x_1, x_2, d_1, d_2, t0, t1, o, d, dy = 1e-5):
```

```
    phase = 'des'
    # Frational area calculation of support and free standing membrane
    A_tot = 450*450
    num_holes = 1125*1125
    A_holes = np.pi*0.1**2*num_holes
    a_fsm = A_holes/A_tot
    # a_fsm = 0.5
    a_sm = 1-a_fsm

    return a_fsm*(fsm(t, x_1, 0, 0, d_1, 0, dy, t0, phase, d = d) + fsm(t, x_2, 0, 0, d_2, 0, dy, t1, phase, d = d)) + a_sm*(sm(t, x_1, d_1, 0, dy, t0, phase, 


def fitting_model(df, fr, r, phase, exp, p0, dy, a_o = 0, fit_method = 'leastsq', data_type = 'data_diff_x', cen_per = 'X (50%)', x_inf = None, t0_vary = False

    # print(df.loc[fr, r][data_type][cen_per].loc['abs'][0])
    a_o = df.loc[fr, r][data_type][cen_per].loc['abs'].values[0]
    if(exp == 'single'):
        if(phase == 'abs'):
            mod = Model(fit_sing_abs)
            mod.set_param_hint('d', value = df['d'].loc[fr, r], vary = False)
            mod.set_param_hint('dy', value = dy, vary = False)
            mod.set_param_hint('t0', value = df['AS'].loc[fr, r], min = df['AS'].loc[fr, r], max = df['AS'].loc[fr, r] + t0_range, vary = t0_vary)
            mod.set_param_hint('o', value = a_o, vary = False)
            # mod.set_param_hint('x_1', value = np.mean(df.loc[fr, r]['data_diff_x'][cen_per].loc['abs'][-200:]), vary = False)
        elif(phase == 'des'):
            mod = Model(fit_sing_des)
            mod.set_param_hint('d', value = df['d'].loc[fr, r], vary = False)
            mod.set_param_hint('dy', value = dy, vary = False)
            mod.set_param_hint('t0', value = df['DS'].loc[fr, r], min = df['DS'].loc[fr, r], max = df['DS'].loc[fr, r] + t0_range,  vary = t0_vary)
            mod.set_param_hint('o', value = np.mean(df.loc[fr, r][data_type][cen_per].loc['des'][-200:]), vary = False)
            if x_inf is not None:
                mod.set_param_hint('x_1', value = x_inf, vary = False)
        if x_inf is None:
            params = mod.make_params(d_1 = dict(value = p0[0], min = 1e-14, max = 1e-2), #
                x_1 = dict(value = p0[1], min = 0)   #, min = 0
                )
        elif x_inf is not None:
            params = mod.make_params(d_1 = dict(value = p0[0], min = 1e-14, max = 1e-2)) #
    elif(exp == 'dbl'):
        if(phase == 'abs'):
            mod = Model(fit_dbl_abs)
            mod.set_param_hint('d', value = df['d'].loc[fr, r], vary = False)
            mod.set_param_hint('dy', value = dy, vary = False)
            mod.set_param_hint('t0', value = df['AS'].loc[fr, r], min = df['AS'].loc[fr, r], max = df['AS'].loc[fr, r] + t0_range, vary = t0_vary),
            mod.set_param_hint('t1', value = df['AS'].loc[fr, r], vary = t1_vary)
            mod.set_param_hint('o', value = a_o, vary = False)
        elif(phase == 'des'):
            mod = Model(fit_dbl_des)
            mod.set_param_hint('d', value = df['d'].loc[fr, r], vary = False)
            mod.set_param_hint('dy', value = dy, vary = False)
            mod.set_param_hint('t0', value = df['DS'].loc[fr, r], min = df['DS'].loc[fr, r], max = df['DS'].loc[fr, r] + t0_range, vary = t0_vary)
            mod.set_param_hint('t1', value = df['DS'].loc[fr, r], vary = t1_vary)
            mod.set_param_hint('o', value = np.mean(df.loc[fr, r][data_type][cen_per].loc['des'][-200:]), vary = False)
        params = mod.make_params(x_1 = dict(value = p0[0], min = 0), # , min = 0
                                 x_2 = dict(value = p0[1], min = 0), # , min = 0
                                 d_1 = dict(value = p0[2], min = 1e-14, max = 1e-2), #
                                 d_2 = dict(value = p0[3], min = 1e-14, max = 1e-2)) #

    tt = df.loc[fr, r][data_type]['Time'].loc[phase]
    data = df.loc[fr, r][data_type][cen_per].loc[phase]

    result = mod.fit(data, params, t = tt, nan_policy='omit', method = fit_method)
    # result = mod.fit(data, params, t = tt, weights = 1/uncer, nan_policy='omit', method = fit_method)

    # print(result.fit_report())

    return result

def fitting_run(df, fr, r, p_guess = [[2e-8, 3e-3], [2e-9, 3e-3], [3e-3, 1e-3, 10e-9, 2e-9], [3e-3, 1e-3, 10e-9, 2e-9]], data_type = 'data_diff_x', cen_per = '
    result_sing_abs = fitting_model(df, fr, r, 'abs', 'single', p0 = p_guess[0], dy = dy, data_type=data_type, cen_per=cen_per, fit_method=fit_method, t0_vary=
    if constantConc:
        result_sing_des = fitting_model(df, fr, r, 'des', 'single', p0 = p_guess[1][:2], x_inf = result_sing_abs.params['x_1'].value, dy = dy, data_type=data_t
    else:
        result_sing_des = fitting_model(df, fr, r, 'des', 'single', p0 = p_guess[1], dy = dy, data_type=data_type, cen_per=cen_per, fit_method=fit_method, t0_va

    result_dbl_abs = fitting_model(df, fr, r, 'abs', 'dbl', p0 = p_guess[2], dy = dy, data_type=data_type, cen_per=cen_per, fit_method=fit_method, t0_vary=t0_va
    result_dbl_des = fitting_model(df, fr, r, 'des', 'dbl', p0 = p_guess[3], dy = dy, data_type=data_type, cen_per=cen_per, fit_method=fit_method, t0_vary=t0_va

    if cen_per == 'X (50%)':
        df['model_s'].loc[fr, r] = [result_sing_abs, result_sing_des]
        df['model_d'].loc[fr, r] = [result_dbl_abs, result_dbl_des]
    elif cen_per == 'X (33%)':
        df['model_s_33'].loc[fr, r] = [result_sing_abs, result_sing_des]
        df['model_d_33'].loc[fr, r] = [result_dbl_abs, result_dbl_des]
    elif cen_per == 'X (25%)':
        df['model_s_25'].loc[fr, r] = [result_sing_abs, result_sing_des]
        df['model_d_25'].loc[fr, r] = [result_dbl_abs, result_dbl_des]


# Functions to convert centroid wavelength to refractive index and then to analyte concentration

def wavelength_to_refrac(df_ref, n_ref):
    slope_50 = 170      # in nm/RIU
    slope_33 = 180
    slope_25 = 179

    df = df_ref.copy()

    inter_50_calc = np.mean(df['Centroids (50%)'].loc['bas']) - slope_50*n_ref
    df['Centroids (50%)'][:] = (df['Centroids (50%)'] - inter_50_calc)/slope_50
    rel_se_50 = df_ref['Centroid (50%) SE']/df_ref['Centroids (50%)']
    df['Centroid (50%) SE'][:] = rel_se_50

    inter_33_calc = np.mean(df['Centroids (33%)'].loc['bas']) - slope_33*n_ref
    df['Centroids (33%)'][:] = (df['Centroids (33%)'] - inter_33_calc)/slope_33
    rel_se_33 = df_ref['Centroid (33%) SE']/df_ref['Centroids (33%)']
```

```
    df['Centroid (33%) SE'][:] = rel_se_33

    inter_25_calc = np.mean(df['Centroids (25%)'].loc['bas']) - slope_25*n_ref
    df['Centroids (25%)'][:] = (df['Centroids (25%)'] - inter_25_calc)/slope_25
    rel_se_25 = df_ref['Centroid (25%) SE']/df_ref['Centroids (25%)']
    df['Centroid (25%) SE'][:] = rel_se_25

    df.rename(columns = {'Centroids (50%)': 'RI (50%)', 'Centroid (50%) SE': 'Rel (50%) SE', 'Centroids (33%)': 'RI (33%)', 'Centroid (33%) SE': 'Rel (33%) SE'

    return df

# Function to convert the refractive index to a analyte concetration based on molar polarizability of the solvent. For more info on the equations used, refer t
# Saunders' PhD thesis Chapter 3.2

def refrac_to_conc(df_ref, mw_a, rho_a, n_a):
    mw_pdms = 74.15     # Molecular weight [g/mol]
    rho_pdms = 1.03     # Density [g/cm^3]
    n_pdms = 1.4225     # Refractive index

    P_pdms = (mw_pdms/rho_pdms)*((n_pdms**2 - 1)/(n_pdms**2 + 2))
    P_a = (mw_a/rho_a)*((n_a**2 - 1)/(n_a**2 + 2))

    term_np = (n_pdms**2 + 2)/(n_pdms**2 - 1)

    df = df_ref.copy()

    df['RI (50%)'][:] = (P_pdms - P_pdms*term_np*((df['RI (50%)']**2 - 1)/(df['RI (50%)']**2 + 2)))/(P_pdms - P_pdms*term_np*((df['RI (50%)']**2 - 1)/(df['RI (
    ri_se_50 = (6*P_pdms*term_np*P_a*df_ref['RI (50%)'])/((P_a+term_np*P_pdms-P_pdms)*df_ref['RI (50%)']**2 - 2*P_a - term_np*P_pdms - 2*P_pdms)**2
    df['Rel (50%) SE'][:] = ri_se_50*df['Rel (50%) SE'][:]*df['RI (50%)'][:]

    df['RI (33%)'][:] = (P_pdms - P_pdms*term_np*((df['RI (33%)']**2 - 1)/(df['RI (33%)']**2 + 2)))/(P_pdms - P_pdms*term_np*((df['RI (33%)']**2 - 1)/(df['RI (
    ri_se_33 = (6*P_pdms*term_np*P_a*df_ref['RI (33%)'])/((P_a+term_np*P_pdms-P_pdms)*df_ref['RI (33%)']**2 - 2*P_a - term_np*P_pdms - 2*P_pdms)**2
    df['Rel (33%) SE'][:] = ri_se_33*df['Rel (33%) SE'][:]*df['RI (33%)'][:]

    df['RI (25%)'][:] = (P_pdms - P_pdms*term_np*((df['RI (25%)']**2 - 1)/(df['RI (25%)']**2 + 2)))/(P_pdms - P_pdms*term_np*((df['RI (25%)']**2 - 1)/(df['RI (
    ri_se_25 = (6*P_pdms*term_np*P_a*df_ref['RI (25%)'])/((P_a+term_np*P_pdms-P_pdms)*df_ref['RI (25%)']**2 - 2*P_a - term_np*P_pdms - 2*P_pdms)**2
    df['Rel (25%) SE'][:] = ri_se_25*df['Rel (25%) SE'][:]*df['RI (25%)'][:]

    df.rename(columns = {'RI (50%)': 'X (50%)', 'Rel (50%) SE': 'X (50%) SE', 'RI (33%)': 'X (33%)', 'Rel (33%) SE': 'X (33%) SE', 'RI (25%)': 'X (25%)', 'Rel

    return df

# Function to determine the average centroid value between time interval [t_s, t_e] using the centroids percentage given by the string value of the column name

def get_avg_centroid(data, t_s, t_len, cen_per = 'Centroids (50%)'):

    avg_cen = np.zeros(len(t_s))
    se_cen = np.zeros(len(t_s))

    for i in range(len(t_s)):
        data_filt = data.copy()

        t_filt_s = data_filt['Time'] >= t_s[i]
        data_filt.where(t_filt_s, inplace = True)
        data_filt.dropna(inplace = True)

        t_filt_e = data_filt['Time'] <= t_s[i] + t_len
        data_filt.where(t_filt_e, inplace = True)
        data_filt.dropna(inplace = True)


        avg_cen[i] = np.mean(data_filt[cen_per])
        se_cen[i] = sem(data_filt[cen_per])

        return avg_cen, se_cen

# Function to get a subset of the Pandas Dataframe

def get_subset(data, t_s, t_e):
    data_filt = data.copy()

    t_filt_s = data_filt['Time'] >= t_s
    data_filt.where(t_filt_s, inplace = True)
    data_filt.dropna(inplace = True)

    t_filt_e = data_filt['Time'] <= t_e
    data_filt.where(t_filt_e, inplace = True)
    data_filt.dropna(inplace = True)

    return data_filt

# Function that splits and returns the baseline, absorption and desorption sections of a particular run

def get_diffusioncurves(fpath, t_bas_s, t_bas_e, t_abs_s, t_abs_e, t_des_s, t_des_e):
    data = pd.read_csv(fpath)
    base = get_subset(data, t_bas_s, t_bas_e)
    absorp = get_subset(data, t_abs_s, t_abs_e)
    desorp = get_subset(data, t_des_s, t_des_e)
    return data, base, absorp, desorp

# Function used to add a run to a PD Dataframe

def add_run(df, fpath, flowrate, run, flowside, d, date, t_bs, t_be, t_as, t_ae, t_ds, t_de):
    rawData, data_bas, data_abs, data_des = get_diffusioncurves(fpath, t_bs, t_be, t_as, t_ae, t_ds, t_de)

    data_diff = pd.concat([data_bas, data_abs, data_des], keys=['bas', 'abs', 'des'])

    for cen_per in ['Centroids (50%)', 'Centroids (33%)', 'Centroids (25%)', 'Centroids (10%)', 'Centroids (5%)']:
        abs_diff = data_diff[cen_per].loc['abs'].iloc[0] - np.mean(data_diff[cen_per].loc['bas'])
        data_diff[cen_per].loc['abs'][:] = data_diff[cen_per].loc['abs'] - abs_diff

    n_PDMS = 1.4225
    mw_oxyl = 106.16     # Molecular weight in g/mol
    rho_oxyl = 0.8801     # Density in g/cm^3
    n_oxyl = 1.5058      # Refractive index
    M_n2 = 28.05        # Molar flow rate in mol/min
```

```
    P_tot = 101325      # Total pressure in Pa
    M_oxyl = flowrate*1e-3*8.28    # Molar flow rate in mol/min
    X_oxyl = M_oxyl/(M_n2+M_oxyl)    # Molar fraction of o-xylene
    p_s = X_oxyl*P_tot    # Partial pressure of o-xylene in Pa

    data_diff_n = wavelength_to_refrac(data_diff, n_PDMS)
    data_diff_x = refrac_to_conc(data_diff_n, mw_oxyl, rho_oxyl, n_oxyl)

    dataEntry = {'fpath': [fpath],'FlowRate': [flowrate], 'P_s': [p_s], 'FlowSide': [flowside], 'd': [d], 'Run': [run], 'Date': [date], 'BS': [t_bs], 'BE': [t_
    df_entry = pd.DataFrame(dataEntry)
    df_entry.set_index(['FlowRate', 'Run'], inplace=True)

    return pd.concat([df, df_entry])


# Create a Dataframe with all variables

# Description of columns
# Fpath - Filepath for the data
# RawData - PD dataframe with raw data from the saved csv file
# FlowRate - Flow rate of the syringe pump in the run in uL/min
# Run - Run number for each flow rate.
# FlowSide - Whether the flow as from NHA or PDMS side
# d - Thickness of the membrane in centimeters
# Date - Date of run
# BS, BE - Start and end time (in secs) of the baseline dataset within the run
# AS, AE - Start and end time (in secs) of the absorption dataset
# DS, DE - Start and end time (in secs) of the desorption dataset
# data_diff - PD dataframe with baseline portion. Subset of RawData.
# data_diff_n - PD dataframe with absorption portion. Subset of RawData.
# data_diff_x - PD dataframe with desorption portion. Subset of RawData.
# model_s - List of ModelResult objects for single exponential fitting for absorption (index 0) and desorption (index 1)
# model_d - List of ModelResult objects for double exponential fitting for absorption (index 0) and desorption (index 1)

print(pd.__version__)
cols = ['fpath', 'FlowRate', 'P_s', 'Run', 'FlowSide', 'd', 'Date', 'BS', 'BE', 'AS', 'AE', 'DS', 'DE', 'RawData', 'data_diff', 'data_diff_n', 'data_diff_x', '

df = pd.DataFrame(columns=cols)
df.set_index(['FlowRate', 'Run'], inplace=True)

# Example of adding a run to the dataframe

fpath = 'raw_data_2uL_ Feb28.csv'

df = add_run(df, fpath, 2, 1, 'PDMS (new) (F)', 10.21e-4, datetime.datetime(2025, 3, 5), 400, 620, 621, 1500, 1501, 2400)

# Running the fitting for a particular run

fitting_run(df, 2, 1)

# To access the fitting results for double exponential absorption
print(df['model_d'].loc[2, 1][0].params.pretty_print())
```

Appendix C

Chapter 4 appendices

C.1 Custom circuits

C.1.1 Low-noise photodiode amplifier circuit

The photodiode amplifier circuit shown in Fig. C.1 was designed to minimize electronic noise contributions to photodiode signal in the strain sensing system. Each section of the circuit plays a specific role in suppressing noise sources and ensuring signal integrity. A brief description of the functional blocks is provided below.

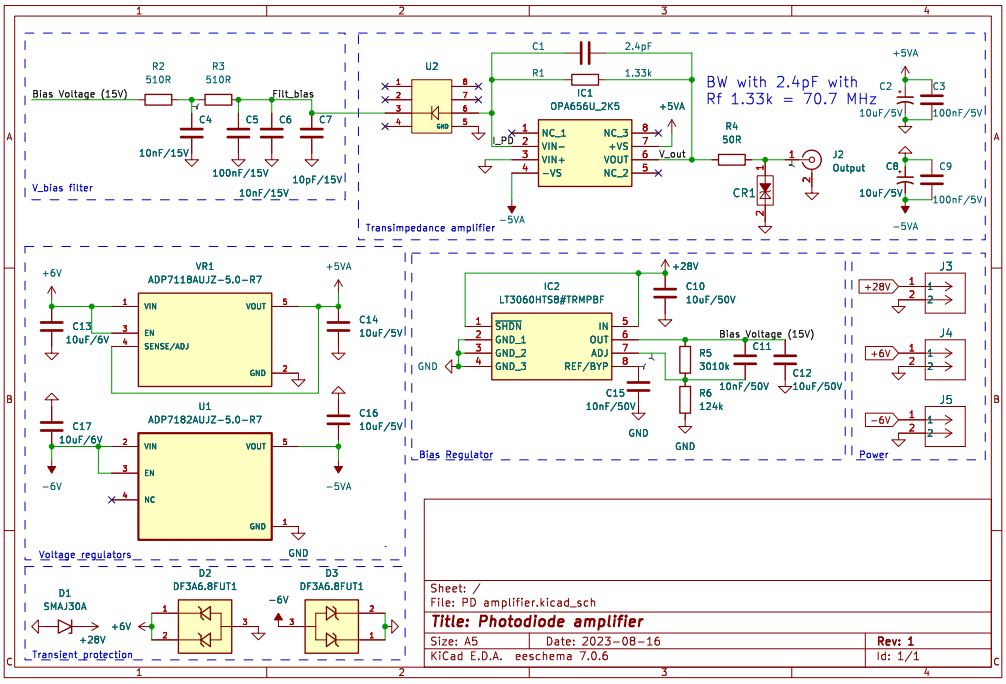

Figure C.1: Schematic of photodiode amplifier circuit

Transient Protection and voltage regulation

The input stage includes transient voltage suppressor diodes (D1, D2), which protect the circuit from high-voltage surges such as electrostatic discharge (ESD) or power line transients. Preventing these events avoids the injection of large noise spikes into the circuit and protects sensitive active components such as the operational amplifier and photodiode. Low-noise power rails are essential for achieving low-noise amplification. The design employs low-dropout regulators (U1: ADP7118 for +5 V, VR1: ADP7118 for –5 V) with extensive bypassing (C14–C17). These regulators provide stable ±5 V supplies with minimal output ripple. The capacitors are placed locally to suppress high-frequency disturbances. By reducing supply-induced noise, these regulators ensure that the operational amplifier operates under stable and quiet conditions. Distributed decoupling capacitors (e.g., C10, C11, and those surrounding the regulators) provide local charge storage and suppress noise from the power supply at high frequencies. This reduces the likelihood of oscillations in the high-gain transimpedance stage.

Photodiode Bias

The photodiode requires a stable reverse-bias voltage to operate in the photocurrent region. A dedicated RC filter network (R2–R4, C5–C7) attenuates noise on the 15 V bias line. Since bias voltage fluctuations translate directly into current noise at the photodiode, filtering this voltage is critical to prevent excess noise from being amplified in the transimpedance stage. The 15 V bias supply is generated from a +28 V input using an ultra-low-noise linear regulator (IC2: LT3060). This regulator, combined with decoupling capacitors (C12, C13, C15), minimizes broadband and low-frequency noise on the bias line. A low-noise bias ensures reduced dark current fluctuations and prevents additional noise from coupling into the photodiode current.

Transimpedance Amplifier (TIA)

The core of the circuit is the transimpedance amplifier, implemented with a high-speed, low-noise operational amplifier (U2: OPA656). A feedback resistor (R1 = 1.33 kΩ) converts the photodiode current into a voltage signal, while a feedback capacitor (C1 = 2.4 pF) stabilizes the amplifier and limits high-frequency noise, setting a bandwidth of approximately 70.7 MHz. The feedback network is carefully selected to balance bandwidth and noise performance. A protection diode (CR1) at the output prevents damage due to overvoltage conditions.

C.1.2 Coherent PDH: Bandpass filter and frequency doubler

The circuit shown in Figure C.2 implements a heterodyne detection stage comprising a bandpass filter and an analog multiplier configured as a frequency doubler. Its primary purpose is to generate a stable second harmonic signal for Pound–Drever–Hall (PDH) detection while minimizing noise contributions from the power supply. Each section of the design is described below.

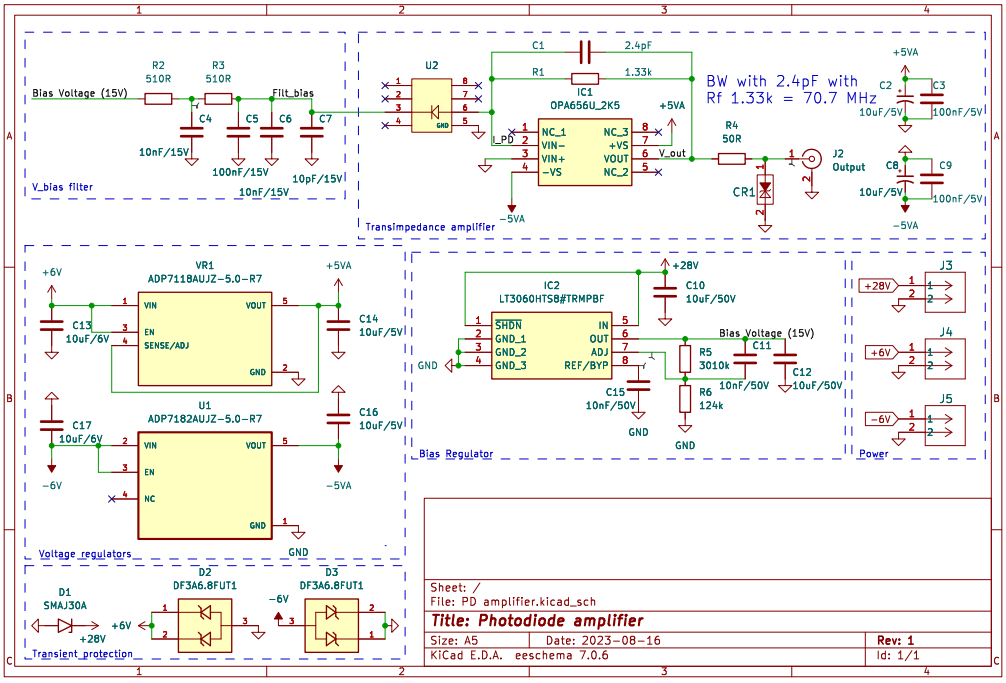

Figure C.2: Schematic of bandpass filter and frequency doubler for coherent PDH setup

Power Regulation and Protection

The input supply passes through diode protection and filtering components (F1, D1, D2), which provide reverse polarity protection and transient suppression. The regulated ±5 V rails are generated using low-noise linear regulators (U1, VR1: ADP7118). Decoupling capacitors (C7–C10) are placed locally to suppress high-frequency disturbances on the supply lines. As in the photodiode amplifier, clean power rails are essential to reduce coupling of supply ripple into the sensitive analog multiplier. Local capacitors (C11–C14) are distributed throughout the design to provide high-frequency stability and prevent oscillations in the analog multiplier and buffer. These components play a crucial role in suppressing noise and ensuring that the frequency doubler operates reliably over the required bandwidth.

Bandpass Filtering

The input RF signal is routed through a band-pass filter network (labelled "Bandpass filter"), which provides spectral selectivity. By attenuating out-of-band noise and harmonics, the filter ensures that only the desired carrier frequency enters the multiplier stage. This improves signal-to-noise ratio (SNR) and prevents unwanted mixing products. Careful grounding and bypassing in this block minimize noise leakage.

Analog Multiplier (Frequency Doubler)

The central stage employs an analog multiplier (U2: AD834) configured as a frequency doubler. When the input RF signal is applied to both multiplier inputs, the output includes both DC and a component at twice the input frequency. The bandpass filter preceding this stage ensures spectral purity, while the decoupling capacitors surrounding the AD834 suppress noise coupling. The doubling process is essential in PDH detection schemes, where frequency-doubled signals provide the error signals necessary for laser frequency stabilization. The use of a low-noise, broadband multiplier ensures accurate frequency conversion with minimal additive noise.

Output Buffering

The frequency-doubled signal is buffered by a wideband operational amplifier (U3: BUF634A). This stage isolates the multiplier from external loads, ensuring consistent output impedance and amplitude. By providing additional drive capability, the buffer prevents distortion or loading effects from subsequent electronics while maintaining low noise levels.